

EFFECTS OF HYDROGEN DILUTION ON
MORPHOLOGICAL, STRUCTURAL AND OPTICAL
PROPERTIES OF NiSi/SiC CORE-SHELL NANOWIRES BY
HOT WIRE CHEMICAL VAPOUR DEPOSITION

ABTISAM HASAN HAMOOD AL-MASOODI

FACULTY OF SCIENCE
UNIVERSITY OF MALAYA
KUALA LUMPUR

2015

EFFECTS OF HYDROGEN DILUTION ON
MORPHOLOGICAL, STRUCTURAL AND OPTICAL
PROPERTIES OF NiSi/SiC CORE-SHELL NANOWIRES BY
HOT WIRE CHEMICAL VAPOUR DEPOSITION

ABTISAM HASAN HAMOOD AL-MASOODI

RESEARCH REPORT SUBMITTED IN FULFILLMENT OF
THE REQUIREMENTS FOR THE DEGREE OF

MASTER OF SCIENCE

(APPLIED PHYSICS)

DEPARTMENT OF PHYSICS

FACULTY OF SCIENCE

UNIVERSITY OF MALAYA

KUALA LUMPUR

2015

UNIVERSITI MALAYA

ORIGINAL LITERARY WORK DECLARATION

Name of Candidate: **ABTISAM HASAN HAMOOD AL-MASOODI**
I/C/Passport No: **05305870**
Registration/Matric No.: **SGB120015**
Name of Degree: **MASTER OF SCIENCE (APPLIED PHYSICS)**

Title of Project Paper/Research Report/Dissertation/Thesis (“this Work”):

“Effects of hydrogen dilution on morphological, structural and optical properties of NiSi/SiC core-shell nanowires by hot wire chemical vapour deposition”

Field of Study: **NANOTECHNOLOGY AND NANOMATERIALS**

I do solemnly and sincerely declare that:

- (1) I am the sole author/writer of this Work,
- (2) This Work is original,
- (3) Any use of any work in which copyright exists was done by way of fair dealing and for permitted purposes and any excerpt or extract from, or reference to or reproduction of any copyright work has been disclosed expressly and sufficiently and the title of the Work and its authorship have been acknowledged in this Work,
- (4) I do not have any actual knowledge nor ought I reasonably to know that the making of this work constitutes an infringement of any copyright work,
- (5) I hereby assign all and every rights in the copyright to this Work to the University of Malaya (“UM”), who henceforth shall be owner of the copyright in this Work and that any reproduction or use in any form or by any means whatsoever is prohibited without the written consent of UM having been first had and obtained,
- (6) I am fully aware that if in the course of making this Work I have infringed any copyright whether intentionally or otherwise, I may be subject to legal action or any other action as may be determined by UM.

(Candidate Signature)

Date:

Subscribed and solemnly declared before,

Witness’s Signature

Date:

Name:

Designation:

ABSTRACT

NiSi/SiC core-shell nanowires grown on Ni-coated silicon substrates by hot-wire chemical vapour deposition were studied. Nickel was used as a catalyst to induce the growth of these core-shell nanowires at different hydrogen dilutions varying from 20 to 99 %. These nanowires consisted of single crystalline NiSi and amorphous SiC as core and shell of the nanowires, respectively. Moreover, an increase in hydrogen dilution enhances the decomposition rate and therefore improve the gas phase reactions of SiC formation. The shell of the nanowires showed the presence of 3C-SiC nano-crystallites embedded within an amorphous matrix. However, further increase in hydrogen dilution up to 99 % suppresses the growth of the nanowires attributed to film growth condition of SiC. The presence of Si and SiC nano-crystallites embedded within an amorphous matrix exhibited a room temperature PL emission in the range of 400-900 nm. These nanowires appeared a very low reflectance in visible range. The effects of the hydrogen dilution on the morphological, structural and optical properties of these core-shell nanowires are discussed.

Keywords: Core-shell nanowires; hydrogen dilution; Nickel silicides; phase transitions; SiC; HWCVD.

ABSTRAK

NiSi / SiC nanowayar teras-cangkerang tumbuh di atas substrat silikon dengan disaluti Ni menggunakan wayar panas wap kimia telah dikaji. Nikel digunakan sebagai pemangkin untuk mendorong pertumbuhan nanowayar teras-cangkerang dengan pencairan hidrogen yang berbeza diantara 20-99%. Nanowayar ini terdiri daripada hablur tunggal NiSi dan amorfus SiC sebagai teras dan tempurung, masing-masing daripada nanowayar. Selain itu, peningkatan dalam pencairan hidrogen meningkatkan kadar penguraian dan oleh itu meningkatkan tindak balas fasa gas pembentukan SiC. Cangkerang nanowayar menunjukkan kehadiran 3C-SiC nano hablur terbenam dalam matriks amorfus. Walau bagaimanapun, peningkatan dalam pencairan hidrogen sehingga 99% menyekat pertumbuhan nanowayar dikaitkan dengan keadaan pertumbuhan filem SiC. Kehadiran Si dan SiC nano-hablur terbenam dalam matriks amorfus dipamerkan pada suatu pancaran PL suhu bilik dalam lingkungan 400-900 nm. Nanowayar ini muncul pada pantulan lingkungan yang sangat rendah. Kesan pencairan hidrogen pada sifat-sifat morfologi, struktur dan optik nanowayar teras-cangkerang turut dibincangkan.

Kata kunci: Teras-cangkerang; nanowayar; pencairan hidrogen; Nikel silicides; peralihan fasa; SiC; HWCVD.

ACKNOWLEDGEMENT

In the name of Allah, invocation and greeting to adoration of Nabi Muhammad (S.A.W.), thanks to God because giving me strength and patience in finishing this Final Project. Alhamdulillah.

In particular, I wish to express my sincere gratitude to my family for their continuous support and help, specially my parents who always care for my study and tried to be patient for my absence, thanks to them for understanding and giving me this chance to complete my research. Also, I would like to express my sincere appreciation and thanks to my supervisor, Dr. Goh Boon Tong for his continuous guidance and patience towards my research development progress. He has guided me strictly to make sure that I have produced my best effort. He had spent his valuable time with me to discuss any problems and issues faced by me.

In addition, I would like to thank Hajjah University to sponsor my full scholarship, all Low Dimensional Materials Research Centre and Department of Physics in University of Malaya members for guiding me, gives suggestions and ideas. The experiences with them have been wonderful, interesting and rewarding one.

Last but not least, I want to take this opportunity and thank my brothers who gave me their words of encouragement and motivated me to finish my research.

Thank you!

The scholarship I have was sponsored by Hajjah University in Yemen and also this work was supported by the University of Malaya Research Grant (UMRG) of RG259-13AFR and University of Malaya Global Collaborative Programme of RU022D-2014.

TABLE OF CONTENTS

	Page
Abstract	iii
Abstrak	iv
Acknowledgement	v
Table of Contents	vi
List of Figures	ix
List of Tables	xiii
List of Appendices	xiv
Chapter 1: INTRODUCTION	
1.1 Background	1
1.2 Motivation of This Work	3
1.3 Objectives	4
1.4 Research Report Overview	5
Chapter 2: LITERATURE REVIEW	
2.1 Introduction	6
2.2 SiC Nanowires & SiC Based Core-Shell Nanowires	6
2.2.1 SiC Nanowires	7
2.2.2 SiC Based Core-Shell Nanowires	7
2.2.3 NiSi Nanowires	8
2.2.4 Advantages of Core-Shell Nanowires in Applications	9
2.3 Growth Techniques	10
2.3.1 PECVD, Laser Ablation, MOCVD, Thermal Evaporation	10
2.3.2 HWCVD	14
2.4 Growth Mechanism	15

2.4.1 VLS, VS, SLS	16
2.4.2 VSS	18
2.5 Morphological, structural and optical properties	19
Chapter 3: EXPERIMENTAL PROCEDURE	
AND CHARACTERIZATION TECHNIQUES	
3.1 Experimental Set Up	24
3.1.1 Reactor Geometry	26
3.1.2 Supply Units	27
3.1.2.1 RF Power Supply	27
3.1.2.2 Filament Heating Supply	28
3.1.2.3 Substrate Holder Heating Supply	29
3.1.2.4 Gas Supplies	30
3.1.2.5 Water Supply	30
3.2 Vacuum System	31
3.3 Materials Preparation	33
3.3.1 Substrates Cleaning	33
3.3.2 Filament Preheating	34
3.4 Growth Processes	35
3.4.1 System Evacuation	36
3.4.2 Substrates Heating	36
3.4.3 Metal Thin Film Deposition	36
3.4.4 Plasma Treatment	37
3.4.5 Growth Deposition	37
3.5 Post-deposition	38
3.6 Characterization Techniques	39

3.6.1 Field Emission Scanning Electron Microscopy (FESEM)	39
3.6.2 High Resolution Transmission Electron Microscopy (HRTEM)	40
3.6.3 Energy Dispersion X-Ray spectroscopy (EDS)	41
3.6.4 Micro-Raman Scattering Spectroscopy	42
3.6.5 Photoluminescence (PL)	43
3.6.6 X-Ray Diffraction (XRD)	44
3.6.7 UV/VIS/NIR Spectrophotometer	45
Chapter 4: RESULTS AND DISCUSSIONS	
4.1 FESEM Analysis	47
4.2 TEM and STEM/EDS Mapping Analysis	49
4.3 Raman Analysis	54
4.4 XRD Analysis	57
4.5 PL Analysis	59
4.6 UV/VIS/NIR Optical Reflectance Analysis	62
Chapter 5: CONCLUSIONS	
5.1 Conclusions	65
REFERENCES	66
APPENDICES	74

LIST OF FIGURES

	Page	
Figure 2.1	(a) Shows the custom-designed plasma-enhanced horizontal tube furnace (PEHTF, the inset shows a DC plasma discharge). (b) Shows a sketch of high-temperature (~ 700 °C) catalyst-assisted synthesis of semiconducting ZnO nanowires. (c) Illustrates low-temperature (~ 420 °C) catalyst-free synthesis of semiconducting ZnO nanowires (Ostrikov et al, 2012).	11
Figure 2.2	Schematic of a typical reactor for Laser Ablation.	12
Figure 2.3	Schematic of a typical reactor for MOCVD.	13
Figure 2.4	Schematic of a typical reactor for thermal evaporation.	14
Figure 2.5	Schematic diagram for home-built HW-PECVD system.	15
Figure 2.6	Schematic depiction of the SiNW growth via the SLS mechanism: (a) deposition of a thin layer of Ni on the Si (111) substrate;(b) formation of the Si-Ni eutectic liquid droplets; (c) the continuous diffusion of Si atoms through the substrate-liquid (S-L) interface;(d) final state of the SiNW growth. The smooth surface of the original substrate becomes rough at the end of the SiNW growth (Yu et al, 2001).	17
Figure 2.7	schematic diagram of the VSS growth mechanism for Si/SiC core shell NWs.	19
Figure 2.8	SiC nanowires without catalyst by using thermal evaporation	20
Figure 2.9	SiC nanowires a) with Al catalyst b) with Ni catalyst (Chang, 2008)	20

Figure 2.10	(a) FESEM (b) TEM images of NiSi/SiC core-shell nanowires prepared by HWCVD.	21
Figure 2.11	Room temperature photoluminescence spectra of SiC/SiO ₂ nanowires (a) as grown, (b)-(d) annealed in oxygen and Aragon mixed gas atmosphere at 1000°C for 3 min, 5min and 30min, respectively(Xia et al, 2014).	22
Figure 2.12	PL spectra of the Si/SiC core-shell nanowires prepared by HWCVD at different deposition pressures of 0.5 and 1 mbar.	23
Figure 3.1	Photograph of hot wire chemical vapor deposition system.	24
Figure 3.2	The schematic diagram of the hot wire chemical vapor deposition system.	25
Figure 3.3	schematic diagram of the reactor of the HWCVD	27
Figure 3.4	RF5S plasma production front panel.	28
Figure 3.5	Configuration of the vacuum pump system.	32
Figure 3.6	The cleaning steps of the substrates for (a) glass and (b) silicon.	34
Figure 3.7	The main stages of growth the nanowires.	35
Figure 3.8	(a) schematic diagram of the configuration of SEM, (b) photograph of Hitachi S4700 SEM	40
Figure 3.9	(a) schematic diagram of the configuration of HRTEM, (b) photograph of JEOL JEM-2100F HRTEM	41
Figure 3.10	(a) schematic diagram of the configuration of EDX, (b) photograph of HAAF/STEM and Oxford EDS.	42
Figure 3.11	(a) Schematic diagram of the configuration of micro-Raman spectroscopy, (b) photograph of Renishaw invia Raman Microscopy.	43

Figure 3.12	Basic scheme of a PL spectroscopy	44
Figure 3.13	(a) X-ray diffracted beam path in $\theta/2\theta$ mode (b) photograph of PANalytical EMpyrean X-ray diffraction.	45
Figure 3.14	(a) Schematic diagram of the configuration of UV/VIS/NIR Spectrophotometer, (b) photograph of UV/VIS/NIR spectrophotometer-V-570- JASCO SLM-468.	46
Figure 4.1	FESEM of NiSi/SiC core shell nanowires prepared by HWCVD at different hydrogen dilutions. Inset of each image a high magnification of FESEM images.	48
Figure 4.2	The variations of the lengths and diameters on the FESEM images against the hydrogen dilutions, an inset figure shows the variation of number densities with hydrogen dilutions.	49
Figure 4.3	(a) TEM image of the NiSi/SiC core-shell nanowires grown by HWCVD at hydrogen dilution of 43 %; (b), (c), (d), (e) and (f) show HRTEM images of the core-shell, near the edge of the core, shell and tip of the nanowires as labelled in the figure. Inset image (d) shows the FFT of the shell of the nanowire.	51
Figure 4.4	(a) Dark-field STEM image of the NiSi/SiC core-shell nanowires grown by HWCVD at hydrogen dilution of 43 %. The solid pink box in (a) shows the scanning area for the elemental maps on the single nanowire; (b)–(e) represent each EDS element map of the core-shell nanowire; (f) STEM/HAADF image of a typical single nanowire with an inset of EDS elemental profile overlay with the image; (g) EDS line scan of the elemental profile of a single nanowire at the stem.	53

Figure 4.5	(a) Raman scattering spectra of NiSi/SiC nanowires prepared by HWCVD at different hydrogen dilutions; (b) Si phonon modes at Raman scattering of the nanowires prepared at 20 % which the decomposed components are labelled as amorphous (amor), grain boundaries (g.b.) and crystalline (cryst).	56
Figure 4.6	XRD patterns of NiSi/SiC core shell nanowires prepared by HWCVD at different hydrogen dilutions.	59
Figure 4.7	(a) PL spectra of NiSi/SiC core-shell nanowires in different hydrogen dilutions. (b) a typical Gaussian de-convolution plot of the peak into different emission bands.	62
Figure 4.8	Optical reflectance spectra of NiSi/SiC core shell nanowires at different hydrogen dilutions.	64

LIST OF TABLES

		Page
Table 1.1	The properties of SiC semiconductor.	3
Table 3.1	The main conditions for plasma treatment.	37
Table 3.2	The gases flow rate, hydrogen dilution and the surface temperature at growth deposition.	38

LIST OF APPENDICES

	Page
Appendices A XRD patterns of materials.	74
Appendices B Gaussian plot of Raman scattering.	89
Appendices C Gaussian plot of PL spectrum.	90

CHAPTER 1

INTRODUCTION

1.1 Background

Recently, the rapid pace of research in the field of one dimensional semiconductor nanostructures such as nanowires and nanorods have been driven by the very exciting scientific challenges and technological potential of mesoscopic systems (Senozan et al, 2011; Lisowski & Zipper, 1998). The semiconductor nanowires and nanorods, mostly silicon based nanorods and nanowires, have achieved excellent structural, optical and electrical properties (Huong et al, 2011; Mezy et al, 2006; Minaee et al, 2013), such as their ideal of the light trapping (Zhu et al, 2008; Tsakalakos et al, 2007) and the conductive paths for collecting photo-generated carriers about $\sim 2 \mu\text{m}$ (Kelzenberg et al, 2008). These superior properties have made silicon based nanowires to emerge in many applications, such as nanolasers (Yang, 2012), optical waveguides (Vj et al, 2011), light emitting devices (Alvi et al, 2011), solar cells (Thambidurai et al, 2014) and sensors (Minaee et al, 2013). Heterostructure nanowires such as core-shell nanowires have significant technological potential in building blocks for the construction of nanoscale electronic and optoelectronic devices. The core-shell nanowire structure could increase the charges collection, suppress the recombination and show higher emission intensity and low thermal conductivity(Liu et al, 2011; Gao et al, 2014) that improve the efficiency with respect to single-nanowires (Yang, 2005). These nanowires appear as an active materials, enabling the cost-effective production of electricity, which is cost-competitive with the conventional energy sources. That makes core-shell nanowires more suitable in solar energy harvesting, such as photoelectrochemical cells, which would favor for the electrons injection and confines them in the core reducing the surface recombination

(Hwang et al, 2008), and photovoltaic cells (Yin et al, 2011), due to higher photon absorption and larger collection area.

Nanowires composed of nickel silicide (NiSi) core and silicon carbide (SiC) shell are predicted highly electrical conduction, visible emission light and highly mechanical properties. Single crystalline nickel silicide nanowires which have been achieved low resistance at low dimensional have highly metallic properties for enhancing the efficiency of electron transfer (Kim et al, 2007; Wu et al, 2004). The combination of low dimensional and physical properties silicon carbide nanowires have appeared high quality for field emission applications (Zekentes & Rogdakis, 2011; Chen et al, 2011).

The bottom-up approach of hot wire chemical vapor deposition (HWCVD) via catalytic growth is the most popular techniques for low temperature, high deposition rate and large area deposition of silicon and silicon-silicon carbide core-shell nanowires (Goh and Abdulrahman, 2014; Chong et al, 2012). HWCVD serves ion energy suppression and ion less deposition to achieve high quality of nanowires compared to plasma enhanced CVD (Rath, 2003). The decomposition of the molecules such as silane and methane with dilution of hydrogen gas by the hot wire surface is expected to make this technique the ability to fabricate high quality and single crystalline materials which have enabled breakthroughs in their incorporation into useful devices. Moreover, the decomposition of a high density of hydrogen radicals plays an important role in the low temperature growth of nano-crystallite SiC thin films.

The highly linear nanowires were grown by solid-state reaction such as Ni and Si at 575°C by sputtering method. The low-temperature process is desirable for applying nanowires as nanoscale interconnections with little or no damage on the fabricated structures (Kim and Anderson, 2005). Some of nanowires, such as Si NWs synthesized by using anodic aluminum oxide template (Kuo & Gau, 2011), and Si/SiC core-shell nanowires grown by catalyzing via nickel metal (Goh & Abdulrahman, 2014), can

synthesize well below the eutectic temperature inferring as a vapor-solid-solid (VSS) growth mechanism. This growth mechanism is a solid-phase diffusion mechanism, in which a solid catalyst acts as the energetically favored site for absorption of gas-phase reactants to direct the nanowires growth. In this work, we studied the growth of NiSi/SiC core-shell nanowires using nickel as a catalyst, and silane and methane as gas precursors with different hydrogen dilution via HWCVD system. The morphological, structural and optical properties of the grown nanowires were investigated by field emission scanning electron microscopy (FESEM), high resolution transmission electron microscopy (HRTEM), energy dispersion X-ray spectroscopy (EDS), X-ray diffraction (XRD), micro-Raman scattering spectroscopy, optical spectroscopy and photoluminescence (PL) spectroscopy.

1.2 Motivation of This Work

SiC is a semiconductor and has unique combination physical and chemical properties, as summarized in table 1.1, and high optical absorption at 792cm^{-1} wavenumber. That makes SiC a choice material for a wide range of applications, such as electric and optoelectric applications (Grinberg & Berliner, 2004; Khan, 2014).

Table 1.1: The properties of SiC semiconductor.

Density	Flexural Strength	Hardness	Young's Modulus	Band Gap	Thermal Conductivity	Thermal Stability	Oxidization Temperature
3.21 g/cm ³	490 GPa	32 GPa	440 GPa	3.4- 3.6eV	<10 W/mK	>800- 1000°C	800°C

The SiC nanowires are highly interesting since they have combined the physical properties of SiC with those induced by their low dimensionality (Zekentes & Rogdakis,

2011). For this reason, a large number of scientific studies have been dedicated to their fabrication and characterization as well as to their application in devices.

Nickel silicide is a promising material to substitute for those silicide materials providing several advantages, such as low resistivity about $14\mu\Omega\text{cm}$, low Si consumption that is only 0.82 nm of Si is consumed per 1nm of nickel, low formation temperature, density of 7.4g/cm^3 and high electric conductivity (Lee et al, 2010). Recently, Ni silicide has appeared as an ideal electrical contact materials to the source, drain and gate in complementary metal oxide silicon devices and also shows an excellent scaling down behavior (Lavoie et al, 2003).

Ni with heavy doping of Si with SiC structure is a metal-semiconductor low resistance ohmic contact (Sze & Ng, 2006) leading to the electrons in NiSi/SiC core-shell nanowires to be conducted away from the junction for improving the efficiency.

Due to the effect of quantum confinement, the band gap energy of nanomaterial would become larger, and a blue-shifted in photoluminescence (PL) is usually observed. The proper design of core-shell heterostructure is that the shell material has a larger band gap to confine carriers in the core region for the enhancing electrical transport properties. These nanowires have other advantages such as facilitating the charge collection, suppressing the recombination, light absorption, excellent electronic conduction and high mechanical strength. These properties make core-shell nanowires suitable in electric and optoelectronic applications.

1.3 Objectives

The objectives of this work are as follows:

1. To investigate the effects of hydrogen dilution on the growth of NiSi/SiC core-shell nanowires prepared by HWCVD.
2. To study the structural and optical properties of the nanowires by varying hydrogen dilution.

1.4 Research Report Overview

This research report is organized into five chapters, which aims to study the effects of hydrogen dilution of optical and structural properties for NiSi/SiC core-shell nanowires. These properties are useful for optoelectronic applications. Chapter 1 gives a background of core-shell nanowires and their applications. The motivation, main objective and the scope of this study are also highlighted in this chapter.

Chapter 2 furnishes a brief literature review on the nanowires, growth techniques and growth mechanism. Some background literature introduce silicon carbide and nickel silicide nanowires, silicon carbide based core-shell nanowires and their advantages in the application. A various growth techniques and growth mechanisms of the nanowires are discussed. Also some properties of core-shell nanowires, such as morphology and optical, are shown in this chapter.

Chapter 3 shows a chosen method for growth of the nanowires, which is a hot chemical vapor deposition system and their characterization techniques. It presents the set-up of this technique and the unit supplies. The condition for materials preparation and growth processes of five sets of NiSi/SiC core-shell nanowires are discussed in different hydrogen dilution. In the following section, the analytical techniques are explained to characterize the NiSi/SiC core-shell nanowires.

Chapter 4 presents and discusses the properties analysis, which is resulted from the characterization techniques. Finally, chapter 5 summarizes the findings from this work.

CHAPTER 2

LITERATURE REVIEW

2.1 Introduction

The nanowires, which are the potential building blocks for nanoscale devices, are used as a tiny link of components into extremely small circuits. Whereas the components could be created out from the synthesizing of the chemical compounds. The nanowires have been demonstrated the enhancing of the applications efficiency in solar cells, such as photoelectrochemical cells (Sankir & Dogan, 2011) and photovoltaic cells (Chehata et al, 2014), and energy storage (Shahid et al, 2013), due to high photon absorption and large collection area. Also they can appear in bundles (Ibupoto et al, 2013) which are been achieved as tribological additives to improve friction characteristics and reliability of electronic transducers (Noor & Krull, 2014), due to their high aspect ratio.

2.2 SiC Nanowires & SiC Based Core-Shell Nanowires

Carbide NWs were successfully synthesized in 1980 such as SiC and TiC by transformation of carbon nanotube (CNT). Whereas, a whisker growth have been known since 1960s.

Silicon carbide has unique combination physical and chemical properties and it is interesting material that can be nanotube, nanorods and nanowires. SiC nanotubes, which were successfully synthesized in 1995, have elastic modulus of 0.61TPa similarly to SiC nanorods, band gap is about 3.4-3.6 eV, thermal conductivity <10 W/mk and thermal stability >800-1000°C. SiC nanotubes is slowly oxidized at 800°C (Adhikari & Ray, 2011).

2.2.1 SiC Nanowires

There are some methods that are used to synthesis SiC nanowires. SiC nanowires were grown at 1500°C for 2h in an argon atmosphere without any catalyst via vapor solid (V-S) process by rapid heating carbothermal reduction (Li et al, 2011). SiC nanowires were successfully synthesized on Si substrate by the thermal evaporation method without the assistance of a metal catalyst (Chen et al, 2013). Also SiC nanowires can be synthesized with catalyst such as aluminum and nickel by using chemical vapor deposition (Chang, 2008). The branching of SiCNWs was grown with using iron as a catalyst (Cao et al, 2012). Also, Yuejian used simple method to directly fabricate one dimensional of SiC nanostructure from mixtures of Si and carbon nanotubes (CNTs) at relative low temperature without catalyst.

A various polytypes of SiC were produced as a nanowires such as 3C, 6H and 4H. The 3C-SiC nanowires were produced by several methods such as carbothermal reduction, from carbon monoxide and single crystal silicon (Attolini et al, 2008), and reaction of polyethylene terephthalate (PET) waste with SiO₂ microspheres in supercritical carbon dioxide system at 650°C for 3 h followed by vacuum annealing at 1500°C for 4 h (Gao et al, 2013). Also Attolini and his group demonstrated the growth of 3C-SiC using as nickel-catalyst on silicon by a chemical reaction involving carbon tetrachloride as a single precursor in 2009. Zhu et al reported the synthesis of 6H-SiC nanowires on bamboo leaves which were the carbon source and template for the growth of SiC by carbothermal method.

2.2.2 SiC Based Core-Shell Nanowires

Many of the producing of SiC-based on NW structures are covered by an oxide layer and some by C-rich phases i.e. they consist of a continuous crystalline nanowire

encapsulating in a sheath of different crystalline materials. These nanowires are rather one dimensional (1D) core-shell nanocables.

Zhenjiang et al achieved the growth of SiC nanowires with thickness-controlling SiO₂ shells which have been obtained by a simple and efficient method, namely treatment of SiC/SiO₂ core-shell nanowires in NaOH solution. The thickness of the SiO₂ shell can be effectively controlled by selecting the appropriate processing time (Li et al, 2014).

However, the sheath is a thin native oxide with minor influence on the physical properties and often have removed during device fabrication. Recently, nickel silicide NiSi core and SiC shell nanowires have been achieved by using hot wire chemical vapor deposition (HWCVD) (Nazarudin et al, 2014).

2.2.3 NiSi Nanowires

Nickel silicide is a contact material in Si technology and is a promising material to substitute for those silicide materials. Nickel silicide has several advantages; low resistivity, lower Si consumption and lower formation temperature (Kim et al, 2003). Nickel monosilicide is used in complementary-metal-oxide-semiconductor (CMOS) technology as ohmic contact and interconnect due to its several properties which the researchers found such as low temperature silicidation process (Iwai et al, 2002), low resistivity about 14 $\mu\Omega$ cm and low silicon consumption only 0.82 nm of Si is consumed per 1nm of nickel. However, NiSi has negative properties such as thermal instability (Lee et al, 2010). For the annealing at low temperature, the unstable and high resistivity phase Ni₂Si forms. Then, the preferred low resistivity phase NiSi begins to be formed. The NiSi phase is thermally stable up to 700°C and begins to transform to another high resistivity phase NiSi₂ at about 750°C (Zhao et al, 2004). Silicon with nickel silicide has been found with band gap energy about 1.92 and 1.96 eV before and after annealing, respectively, by no presence of hydrogen in Si-nickel silicide due to quantum confinement of a small crystallite size (Mohiddon, 2011).

The NiSi was formed as a thin film by vacuum annealing of nickel on silicon substrate (Bhaskarn et al, 2009). By different SiH₄ flow rate of Ni foam, NiSi can be formed in different phases such as e Ni₂Si nanowires, Ni₃Si₂nanowires and nanorods, and NiSi nanowires (Fan et al, 2012). NiSi nanowires were coated with a thin thickness carbon which is a good ohmic contact without insulating layer. Its resistivity decreases with lowing temperature (Lee et al, 2004). NiSi nanowires can also be prepared without using a gas type silicon source by metal induced growth methods (Kim & Anderson, 2005). That is used as probe to determine the polarity of lead zirconate titanate (PZT) ferroelectric thin film (Kim et al, 2008) and electrical contact in well-known standard technology. Ni is attractive metal at silicon compound because of its favorable impurity level in Si (Schmidt et al, 2010). By using metal induced CVD with only 50sccm of SiH₄ precursor for silicon substrate coated with Ni thin film that can be formed of NiSi NWs (Decker et al, 2004).

2.2.4 Advantages of Core-Shell Nanowires in Applications

Some core-shell nanowires, such as CdS/Cu₂S core-shell nanowires, can be used in solar cells, which has fill factor values superior to those reported for equivalent planar cells and an energy conversion efficiency of ~5.4% that is comparable to that of equivalent planar cells despite low light absorption levels (Tang et al, 2011). While, a strong photoresponse of ZnO/ZnSe core-shell nanowires, which have advantages for planar devices in light absorption, charge transport and collection, were demonstrated the feasibility and great potential for exploring all-inorganic versions type of heterojunction solar cells with wide band gap semiconductor (Cao et al, 2012).

The branches of SiC NWs can be achieved as a good green emission at peak of 535nm at room temperature that makes them having a good property for optoelectronic devices (Cao et al, 2012). Recently, the use of low dimensional nanostructure for optoelectronic applications is intensively studied. SiC/SiO₂ core-shell nanowires were

reported to exhibit a sharp ultraviolet peak at 380 nm and an intensive broad green band at maximum peak of 505 nm, which were observed in spectra of as-grown nanowires. In addition, SiC nanowires with SiO₂ shell exhibit a distinctly enhanced green emission while the bulk SiC light emission intensity is very low owing to its indirect band gap structure (Xia Liua et al, 2014).

2.3 Growth Techniques

Semiconductor NWs can be synthesized by using a variety of growth techniques such as organo-metallic vapor phase epitaxy (OMVPE), laser ablation and chemical vapor deposition.

2.3.1 PECVD, Laser Ablation, MOCVD, Thermal Evaporation.

A radio frequency (RF) generator is used to induce plasma for the deposition gas in a plasma enhanced chemical vapor deposition (PECVD) technique. The PECVD appears to be an efficient method for production of metal coatings on nanowires. Coating of nanowires with Ni and Pt nanoparticles with high particular densities have been synthesized on silicon carbide nanowires by using this technique. That was being investigated to broaden potential uses for future applications (LaLonde et al, 2005). Also this technique was used to grow ZnO nanowires as shown in figure 2.1.

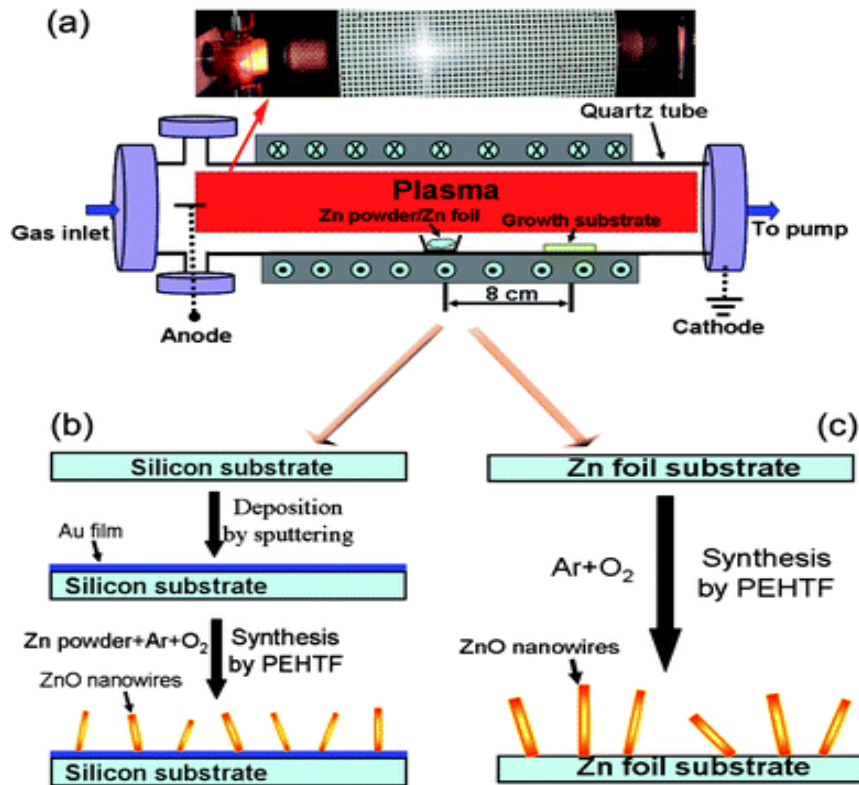


Figure 2.1: (a) shows the custom-designed plasma-enhanced horizontal tube furnace (PEHTF, the inset shows a DC plasma discharge). (b) shows a sketch of high-temperature ($\sim 700\text{ }^{\circ}\text{C}$) catalyst-assisted synthesis of semiconducting ZnO nanowires. (c) illustrates low-temperature ($\sim 420\text{ }^{\circ}\text{C}$) catalyst-free synthesis of semiconducting ZnO nanowires (Ostrikov et al, 2012).

Laser ablation, as shown in figure 2.2, is a laser-assisted method where the catalyst uses to define nanowires. This technique was used for synthesizing semiconductor nanowires such as silicon and germanium nanowires (Morales & Lieber, 1998). During the laser ablation the source material is ablated into a vapor phase which may have the same composition as the precursor. Then, the vapor phase is transferred to a substrate where nanowires nucleate and grow. This technique is useful for synthesizing of nanowires with high melting temperature because a high energy laser can ablate solid materials in a very short time (Li et al, 2011). Also amorphous SiO_x nanowires (NWs) were synthesized using laser ablation of silicon-containing targets. The influence of various parameters such as target composition, substrate type, substrate temperature and carrier gas on the growth process was studied. A metal catalyst was found essential for

the NW growth. A growth temperature which is higher than 1000 °C was important for the NW formation using an Ar-based carrier gas at 500 Torr. The use of Ar-5%H₂ instead of pure Ar resulted in a higher yield and longer NWs. An application of a diffusion barrier on the top of Si substrate guaranteed the availability of metal catalyst droplets on the surface, essential for the NW growth. Ni was found to be a better catalyst than Au in terms of the NW yield and length (Aharonovich et al, 2008).

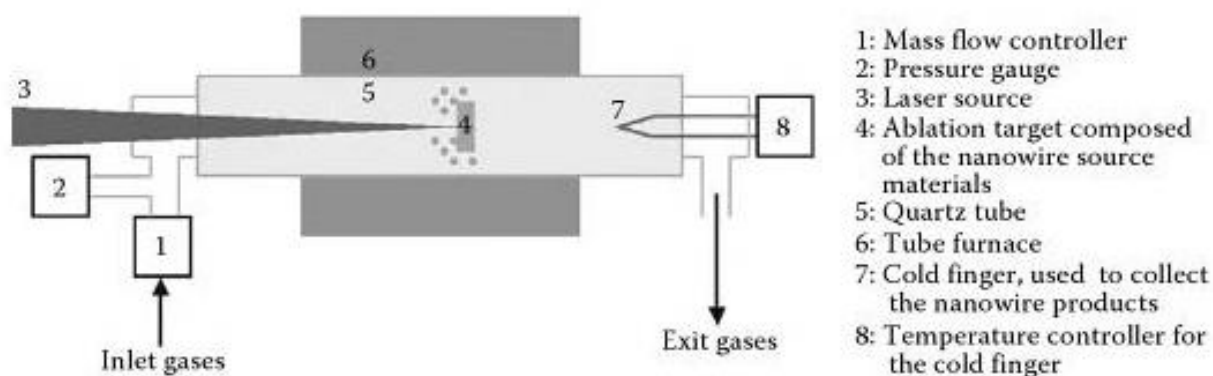


Figure 2.2: schematic of a typical reactor for Laser Ablation.

Metal-organic chemical vapor deposition (MOCVD), as illustrated in figure 2.3, is a special case of CVD method, where one or more of gas-phase precursor is a metal-organic (MO) compound. It consists of a reactor with provision for inlets for reacting gases and MO precursors. MOCVD connects to a vacuum pump and the substrate is placed directly facing the gas flow. A methyl or ethyl-based precursors were used to exhibit lower decomposition temperature that allows the growth at lower temperature than the other CVD methods (Meyyappan & Sunkara, 2009). The self-assembly of Ge₁Sb₂Te₄ nanowires (NWs) for phase change memories application was achieved by MOCVD. These nanowires can be catalyzed by Au nanoislands in a narrow range of temperatures and deposition pressures. That applied in the optimized conditions of temperature of 400 °C and deposition pressure of 50 mbar (Longo et al, 2012). Moreover,

high-quality gallium nitride nanowires have been synthesized via this technique (Kuykendall et al, 2003).

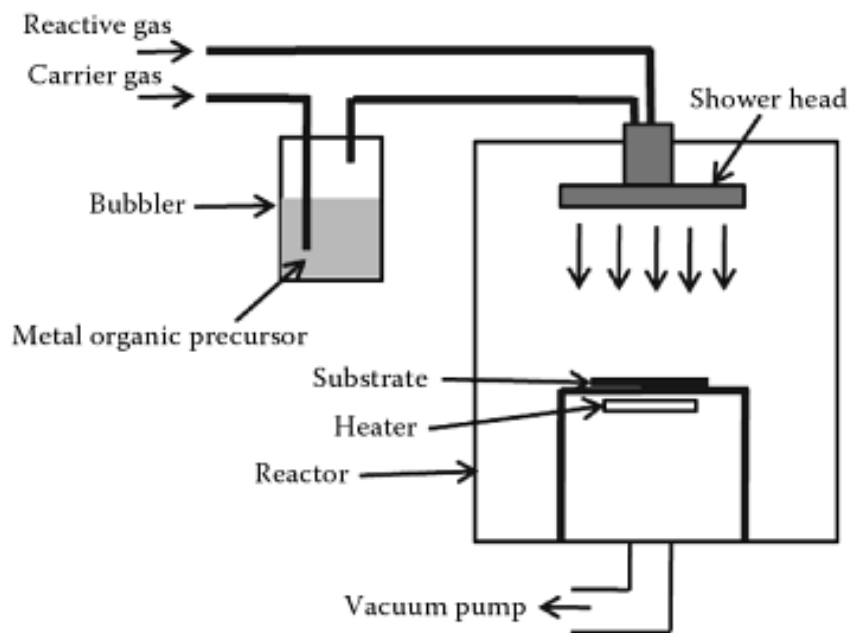


Figure 2.3: schematic of a typical reactor for MOCVD.

Thermal evaporation technique, which is shown in figure 2.4, has zones that allow a hotter source generation with a relatively cooler growth. By this technique the growth was carried out at low pressure about 1-100 Torr, which helped to reduce oxygen contamination. The materials of the crucible should have high melting point, good chemical stability and hardness, so that can be with stand high temperature and chemical corrosion (Meyyappan & Sunkara, 2009). Silicon monoxide (SiO) and Si nanowires were synthesized using using this technique (Niu et al, 2004). Without using the assistance of metal catalyst, SiC nanowires were successfully synthesized on Si substrate by the thermal evaporation method (Chen et al, 2013). Also using this technique by combining with pulsed laser deposition, CdSe/ZnTe core-shell nanowires were synthesized in high-quality on a silicon substrate (Wang et al, 2014).

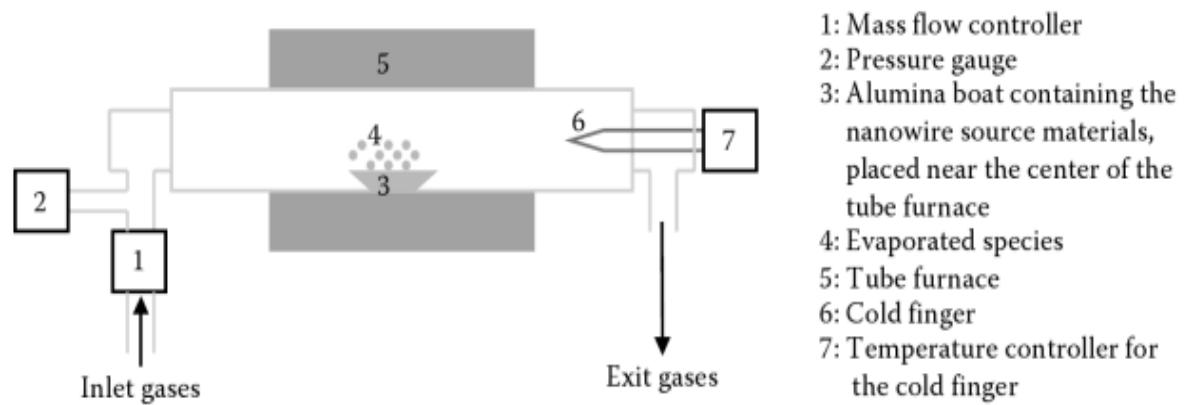


Figure 2.4: schematic of a typical reactor for thermal evaporation.

2.3.2 HWCVD

Hot wire chemical vapor deposition (HWCVD), which is also called hot filament chemical vapor deposition (HFCVD), is another type of chemical vapor deposition system. A filament such as tungsten is mounted in the system and biased to create a localized hot spot (1000-3000°C) that can be resulted in thermal decomposition of the gases or a solid target to provide the vapor phase reactant. HWCVD has been employed for the growth of nanowires such as SiNWs and SiCNWs. The deposition of the catalyst on the substrate reacts with gaseous precursor, which are provided by hot wire. There is a local heater to keep a high temperature of the substrate for maintaining the reaction energy (Jalilian, 2008).

The HWCVD technique is being explored as an effective technique to grow the nanowires using different catalyst such as gold (Chong et al, 2011), indium (Chong et al, 2013) and tin (Meshram et al, 2013). Some researcher achieved a high density of silicon nanowires by using indium nanocones as a catalyst at 3cm distance between the filament and the substrate holder of the HWCVD system (Chong et al, 2013). The filament temperature plays an important role to grow silicon nanowires that the threshold filament temperature lies between 1400 and 1500°C for successive growth of the NWs (Chong et

al, 2012). A radio frequency (rf) power, which is used in growth deposition, can control the growth of the silicon nanowires. The growth of the nanowires can grow at low rf power about 20W while the growth will be suppressed at high rf power about 100W (Chong et al, 2011). A high crystallite Si core which embedded within an amorphous matrix SiC shell was synthesized by using HWCVD system at a distance between the filament and substrate holder 1.9 cm (Goh & Abdulrahman, 2014). Figure 2.5 shows the schematic diagram for home built HW-PECVD system (Chong et al, 2011).

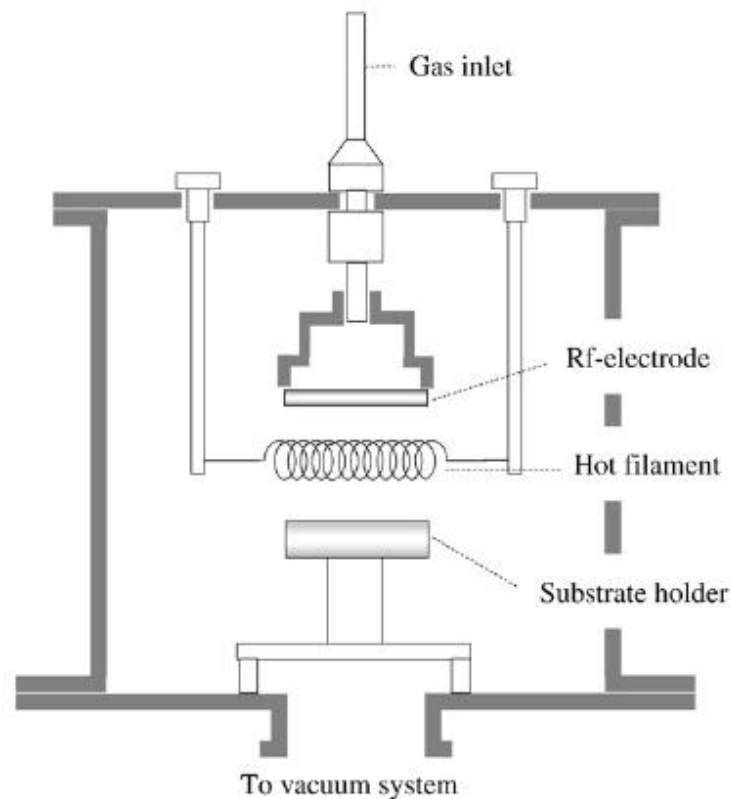


Figure 2.5: Schematic diagram for home-built HW-PECVD system.

2.4 Growth Mechanism

Depending on the configuration of growth/deposition condition and sources of raw materials, different growth mechanisms were existed that are vapor-liquid-solid (VLS), solid-liquid-solid (SLS), vapor-solid (VS) and vapor-solid-solid (VSS) growth mechanism, Most techniques involved VLS and SLS growth mechanisms, in which a

metal catalyst droplet has been used as a nucleation site for adsorption of SiC vapor phase during the growing process of nanowires.

2.4.1 VLS, VS, SLS

The VLS growth mechanism was first presented by Wagner and Treuting. Nowadays, this method was done by a lot of researchers for growing nanowire. The most semiconductor nanowires were synthesized by this mechanism such as silicon and germanium nanowires (Morales & Lieber, 1998). With widths of 15-200 nm, a high-quality gallium nitride nanowires were formed via VLS mechanism with gold, iron, or nickel as growth initiators (Kuykendall et al, 2003). The liquid catalyst acts as the energetically favored spot for absorbing gas-phase reactants. An iron that could pyrolyze from ferrocene was introduced as catalyst into the reaction system. However, no metallic droplets were observed at the tips of nanowires in electron microscopy, which was possibly due to the evaporation of iron under high temperature. That indicated to grow SiC nanowires through VLS mechanism.

The VS growth mechanism stands for vapor-solid growth and it is used to describe all the growth in which the nanowire crystallization originates from the direct condensation from the vapor phase without using of a catalyzer. At the beginning, the growth was attributed to presence of a lattice defects. The nanowires were freed from the defects, this observed explanation had to be abandoned. With noncatalytic and template-free vapor transport process, Sn nanowires with diameters of 10–20 nm were synthesized by following VS mechanism (Hsu & Lu, 2005).

SiNWs were successfully grown by following SLS mechanism in which the substrate served as a source of Si. That controls the growth directly without supplying a gaseous or liquid Si source (Yan et al, 2000). Also Yu et al reported that the SiNWs can be controlled by SLS mechanism in difference from the VLS for conventional whisker growth, as seen in figure 2.6. Also by this mechanism Xing et al successfully synthesized

a core-shell silicon carbide-silicon oxide nanocables on silicon substrate under Ar/H₂ atmosphere.

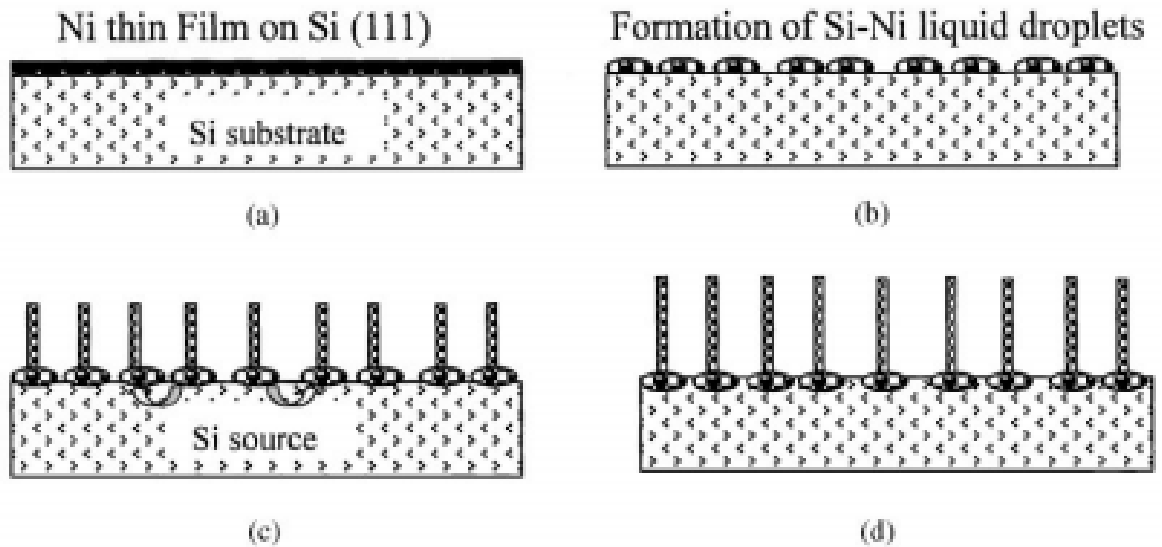


Figure 2.6: Schematic depiction of the SiNW growth via the SLS mechanism: (a) deposition of a thin layer of Ni on the Si (111) substrate;(b) formation of the Si-Ni eutectic liquid droplets; (c) the continuous diffusion of Si atoms through the substrate-liquid (S-L) interface;(d) final state of the SiNW growth. The smooth surface of the original substrate becomes rough at the end of the SiNW growth (Yu et al, 2001).

Metal-catalyzed growth was described to understand the solid phase diffusion mechanism where the most significant work on the mechanism of the unidirectional growth of semiconductor whiskers grown by VLS. The unidirectional growth of Si whiskers can be simply interpreted based on the difference of the sticking coefficients of the impinging vapor source atoms on the liquid (the catalytic droplet) and on solid surfaces. In principle, an ideal liquid surface captures all impinging Si source atoms, while a solid surface of Si rejects almost all Si source atoms if the temperature is sufficiently high. For this mechanism GaAs nanowires was grown by in-situ heating of the nanowires. The proposed growth process has been described as the vapor-liquid-solid (VLS) mechanism, where the epitaxial crystal growth is catalysed by a molten gold droplet in a vapor of the reagents onto a solid substrate surface (Larsson et al, 2005).

2.4.2 VSS

VSS growth mechanism from a solid particle was first proposed for Ag-catalyzed silicon whiskers in 1979. The VSS growth mechanism is a solid-phase diffusion mechanism, in which a solid catalyst acts as the energetically favored site for absorption of gas-phase reactants to direct the nanowires growth (Campos et al, 2008). The VSS mechanism indicates that the metal catalyst does not need to exceed the melting temperature during the nanowires growth. Campos et al reported for this mechanism for ZnO nanowire growth at low temperatures from solid Au-Zn catalyst particles which the presence of these particles is particularly important at the initial growth stages over the Si/SiO₂ substrates to provide nucleation sites for the Zn vapor (Dayeh et al, 2007). Si/SiC core-shell NWs were proposed to follow VSS mechanism as shown in figure 2.7 by using a metal Ni to catalyze the reaction under pressure of 0.5 and 1mbar and 785°C for the substrate temperature (Goh & Abdulrahman, 2014). Due to the high diffusion of Ni into Si, the diffusion of Ni into the accumulated Si layer was firstly formed NiSi layer (Jessica et al, 2009), then nucleation sites were created to induced the growth of Si core of the NWs. From the decomposition of CH₄, the dissolved C atoms were absorbed with excess of Si to form SiC shell of the NWs (Goh & Abdulrahman, 2014).

Furthermore, nanowires can also be grown without a metal seed particles in the presence of an oxide or by masking a substrate.

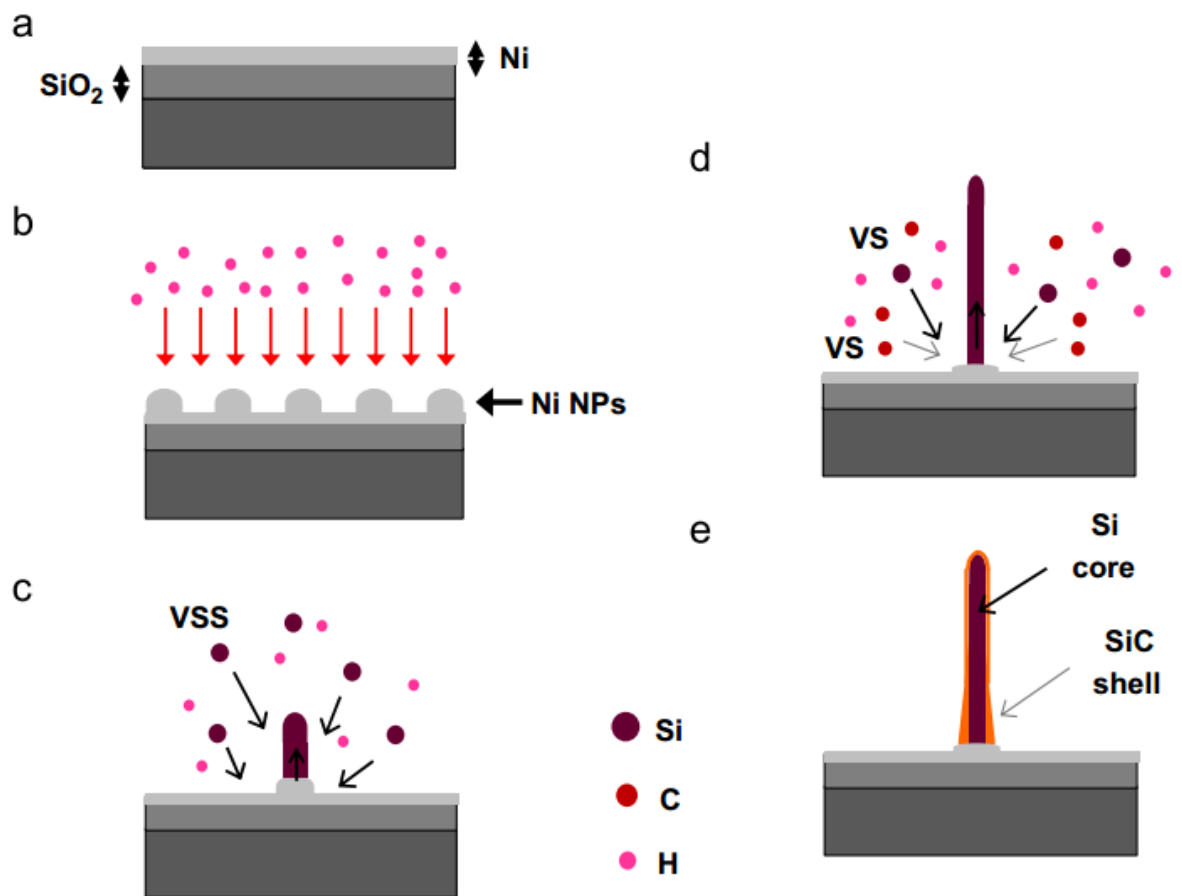


Figure 2.7: schematic diagram of the VSS growth mechanism for Si/SiC core shell NWs.

2.5 Morphological, structural and optical properties

The general morphology of SiC nanowires comes from the SEM image. Figure 2.8 (a) shows a straight and curved SiC nanowires growth randomly by the thermal evaporation method without assistance of a metal catalyst on the Si substrate. These nanowires at high density with length of the nanowires was up to several hundreds of microns, and the diameters were uniformly about 50–100 nm. The length was similar to those of the SiC nanowires synthesized previously by other researchers (Chen et al, 2013).

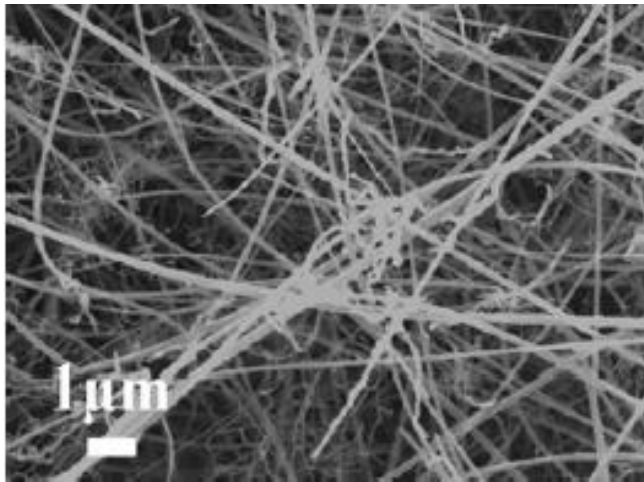


Figure 2.8: SiC nanowires without catalyst by using thermal evaporation.

Chang demonstrated the growth of 3C-SiC nanowires using the CVD system for 60 minutes of the time growth. The length of these nanowires seemed to be dependent on the time of growth up to a certain threshold point and the temperature played the main factor for determining this point. The most effective catalysts for SiC growth were the evaporated layers of 100Å of Al and 100Å of Ni. Al and Ni catalysts produced differing results in terms of structural appearance of the nanowires as seen through scanning electron microscopy (SEM) images in figure 2.9 (a) and (b), respectively.

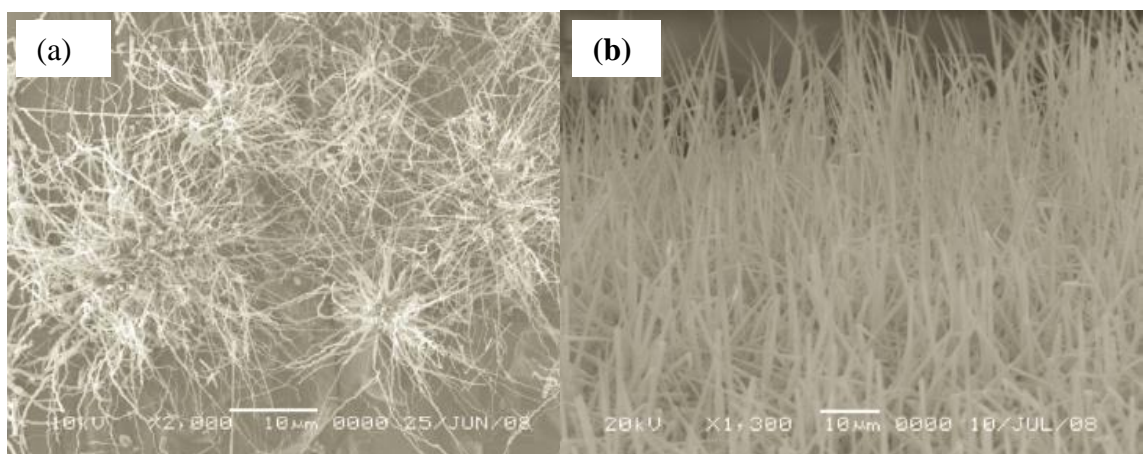


Figure 2.9: SiC nanowires a) with Al catalyst b) with Ni catalyst (Chang, 2008).

Recently NiSi core and SiC shell nanowires, which the FESEM and TEM are shown in figure 2.10, have been achieved using Ni as catalyst at 300 Pa for the pressure in low temperature by HWCVD. These NWs were randomly distributed on the surface of the sample with diameter of 88 nm and length of 2.6 micron. The TEM image of the nanowire shows clearly the core-shell structure, with core and shell diameters of 22 and 105 nm, respectively (Nazarudin et al, 2014).

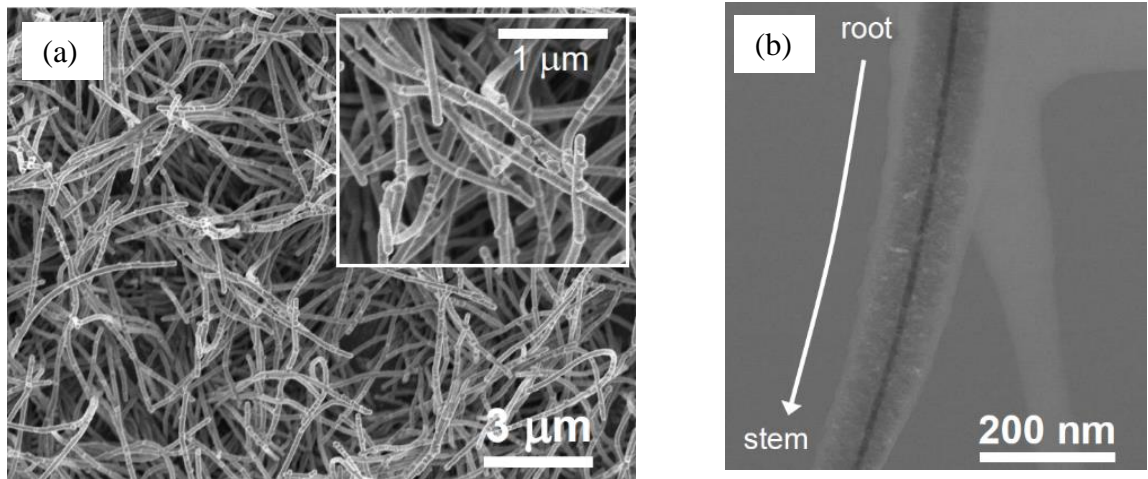


Figure 2.10: (a) FESEM (b) TEM images of NiSi/SiC core-shell nanowires prepared by HWCVD.

Si/SiC core-shell nanowires appear a narrow band near to 520 cm^{-1} of c-Si transverse optic (TO) phonon mode for Raman spectroscopy. This downshift and broadening was resulted from the formation of the Si nano-crystallites embedded within the amorphous matrix of SiC shell (Goh & Abdulrahman, 2014).

At room temperature, photoluminescence (PL) spectra of the SiC/SiO₂ core-shell nanowires with diameter 50nm and length 10 micron in different times of annealing by Oxygen and Aragon gas mix , as shown in the figure 2.11, have been measured under 325nm using a He-Cd laser as an excitation source (Xia et al, 2014). That appeared sharp ultraviolet (UV) peak at 380 nm which was achieved the energy band gap about 3.26 eV.

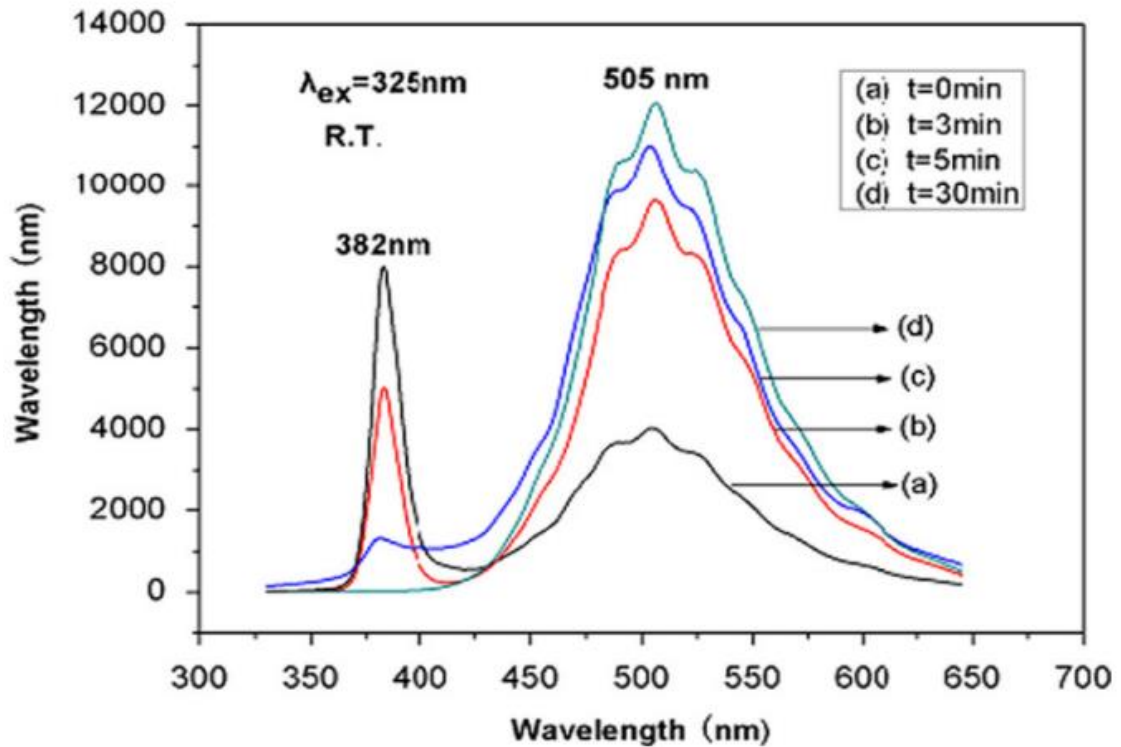


Figure 2.11: Room temperature photoluminescence spectra of SiC/SiO₂ nanowires (a) as grown, (b)-(d) annealed in oxygen and Aragon mixed gas atmosphere at 1000°C for 3 min, 5min and 30min, respectively(Xia et al, 2014).

The Si/SiC core-shell nanowires, which were prepared by HWCVD in different deposition pressures of 0.5 and 1 mbar, show a broad PL emission spectra across photon wavelengths ranging from 400 to 1000 nm, which covers the entire visible region. Whereby the two major constituents centered at approximately 590 and 750 nm, which are dominant in the entire spectrum, as shown in the figure 2.12 (Nazarudin et al, 2015)

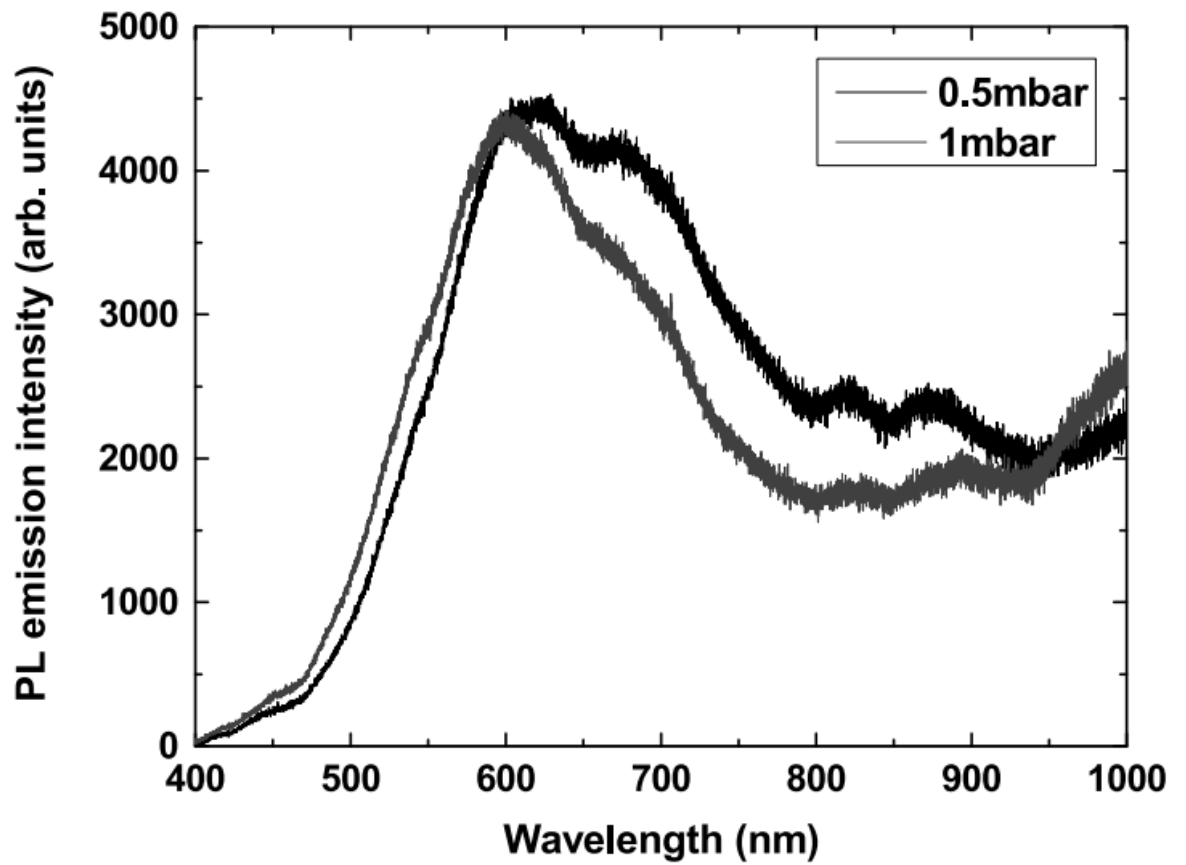


Figure 2.12: PL spectra of the Si/SiC core-shell nanowires prepared by HWCVD at different deposition pressures of 0.5 and 1 mbar.

CHAPTER 3

EXPERIMENTAL PROCEDURE

AND CHARACTERIZATION TECHNIQUES

3.1 Experimental Set Up

The used system in this research, as shown in figure 3.1, is a hot wire chemical vapor deposition system. This system shows the interesting combination of low substrate temperatures and fast deposition rates.

Figure 3.2 illustrates the schematic diagram of the hot wire chemical vapor deposition, which consists mainly of three parts; reactor, vacuum system and supply units.



Figure 3.1: photograph of hot wire chemical vapor deposition system.

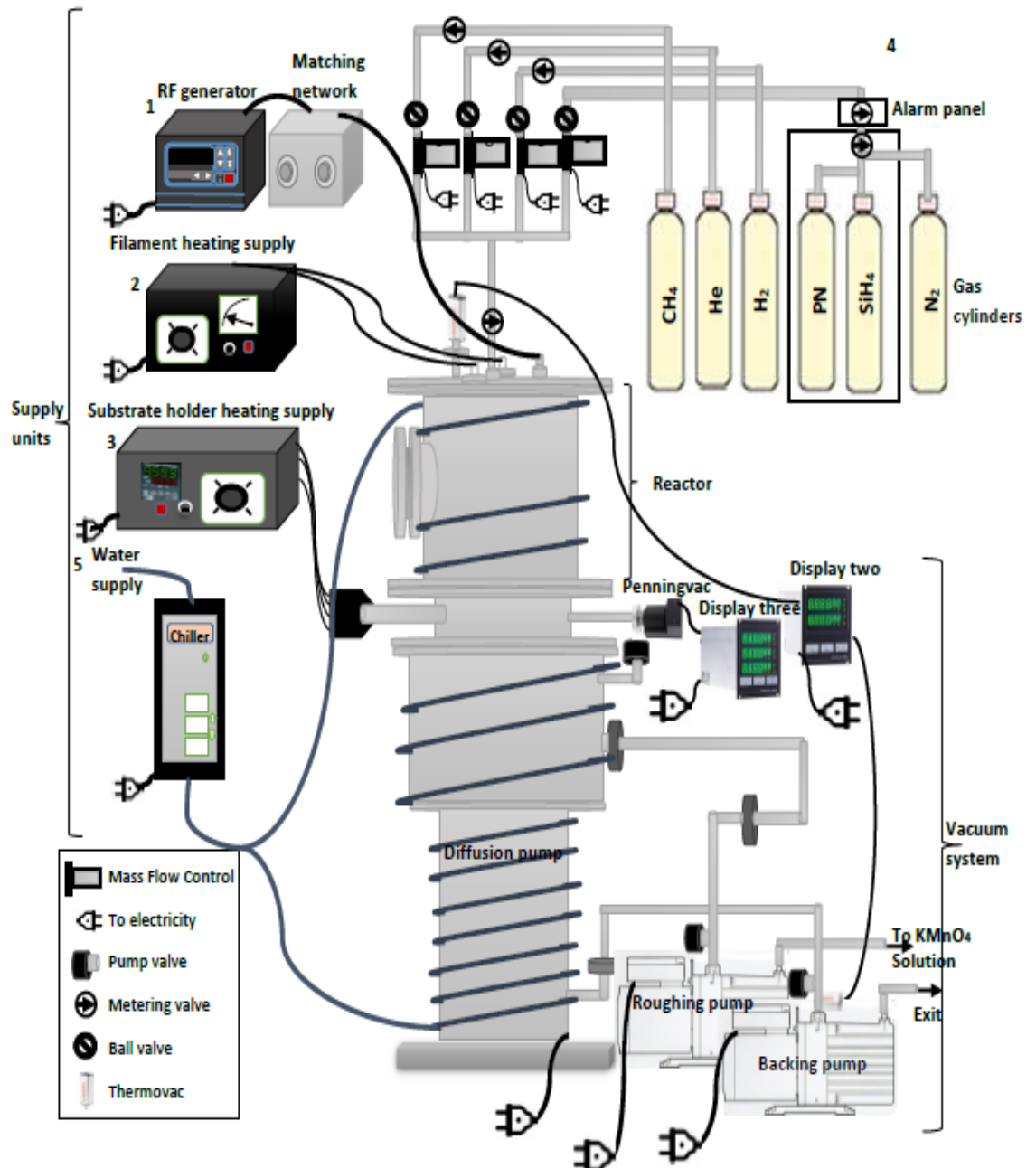


Figure 3.2: the schematic diagram of the hot wire chemical vapor deposition system.

3.1.1 Reactor Geometry

The place which the nanowires grow in is named a reactor or chamber. The utilized reactor is a hollow cylindrical stainless steel chamber with thickness of 0.5 cm, diameter of 16.4cm and height of 16.4cm. The reaction chamber, as shown in figure 3.3, has a circular glass viewport with diameter of 8 cm for display inside the chamber and optical measurement such as the surface temperature in the places of the filament by using Raytek, Raynger 3i pyrometer of infrared thermometer.

For condition of growth, some components are essential to prepare a suitable environment for growth of the nanowires. A gas inlet is 11.2 cm from the top of the chamber which is used for entering different gases through a plasma device. The plasma device is a cylindrical stainless steel electrode in diameter of 5.8 cm and height of 4mm, with 19 cone holes in outer and inner diameters of 1mm and 1.5mm, respectively, is fixed in the end of the gas inlet inside the reactor by a cylindrical insulator. The plasma device is connected with a plasma supply to ionize the gas. A used filament is a tungsten wire (W) with 0.5mm in diameter and 99.95% in purity that was coiled into spiral shape with internal diameter of 1mm for 2cm in length with 2cm of a straight shape in both sides of the spiral shape. Two connecting rods to a filament heating supply, filament holders, are used to set the filament into a specific distance from the substrates. A hole in the top of the chamber is connected with thermovac transmitter which is an active sensor for converting pressure to voltage by using thermal conductivity vacuum gauges which varies between 5×10^{-4} and 1000 mbar. A substrates holder with the diameter of 8.7cm and the height of 0.9cm has six rectangular positions 2.2×1.5 cm in the dimensions. A thermocouple is put inside the substrates holder to measure the real temperature of the samples.

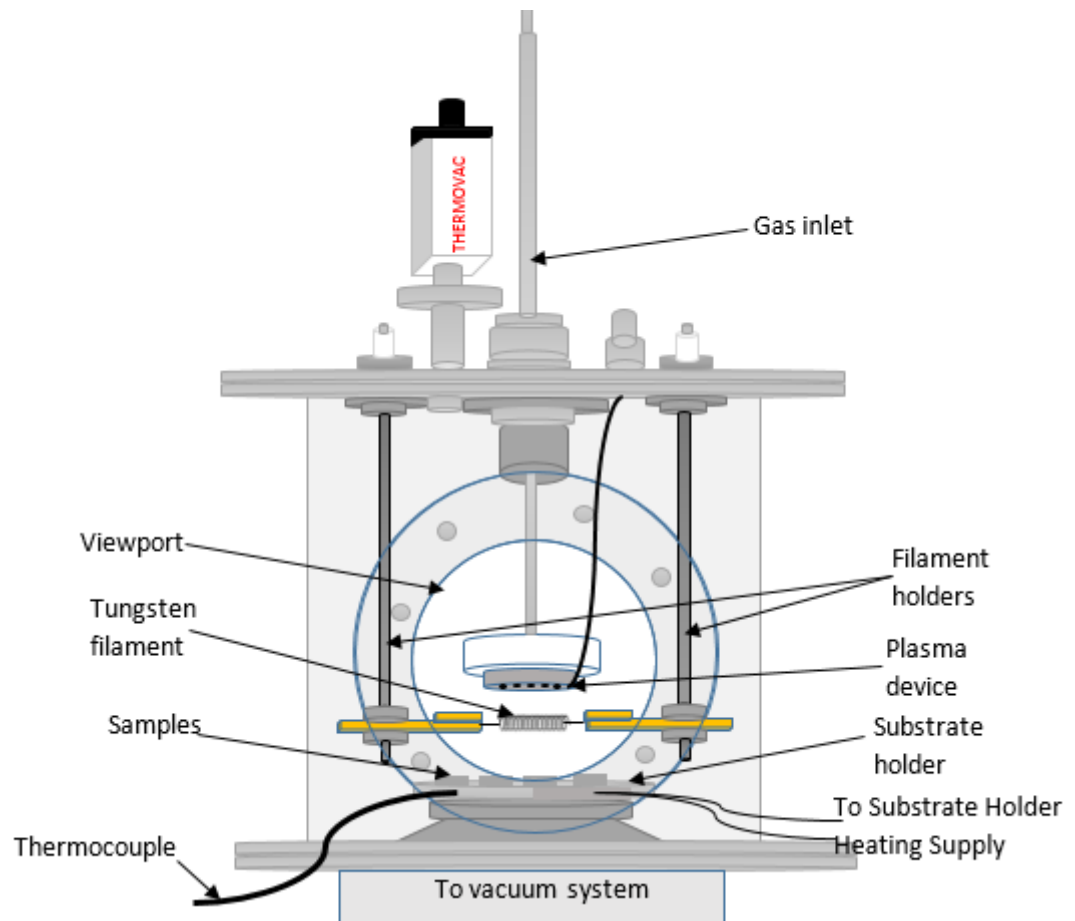


Figure 3.3: schematic diagram of the reactor of the HWCVD.

3.1.2 Supply Units

Some basic elements mainly temperature, gases and cooling system for growth nanowires need supply units. These supplies provide heating, ionizing gases and cooling water to achieve the right qualities for growth of the nanowires. From these supplies which are used in this project as following:

3.1.2.1 RF Power Supply

A device, which is used to provide ionic atoms in the experiment, is called RF5S plasma production. This supply considers the microprocessor based RF power designed to be achieved with a flexible set of options for control and display the desired maximum output power level by using adjustment arrows as seen in figure 3.4. That helps the user to get a pure, stable power source from 0 to the generator's rated power which is 600 Watts in the RF5S.

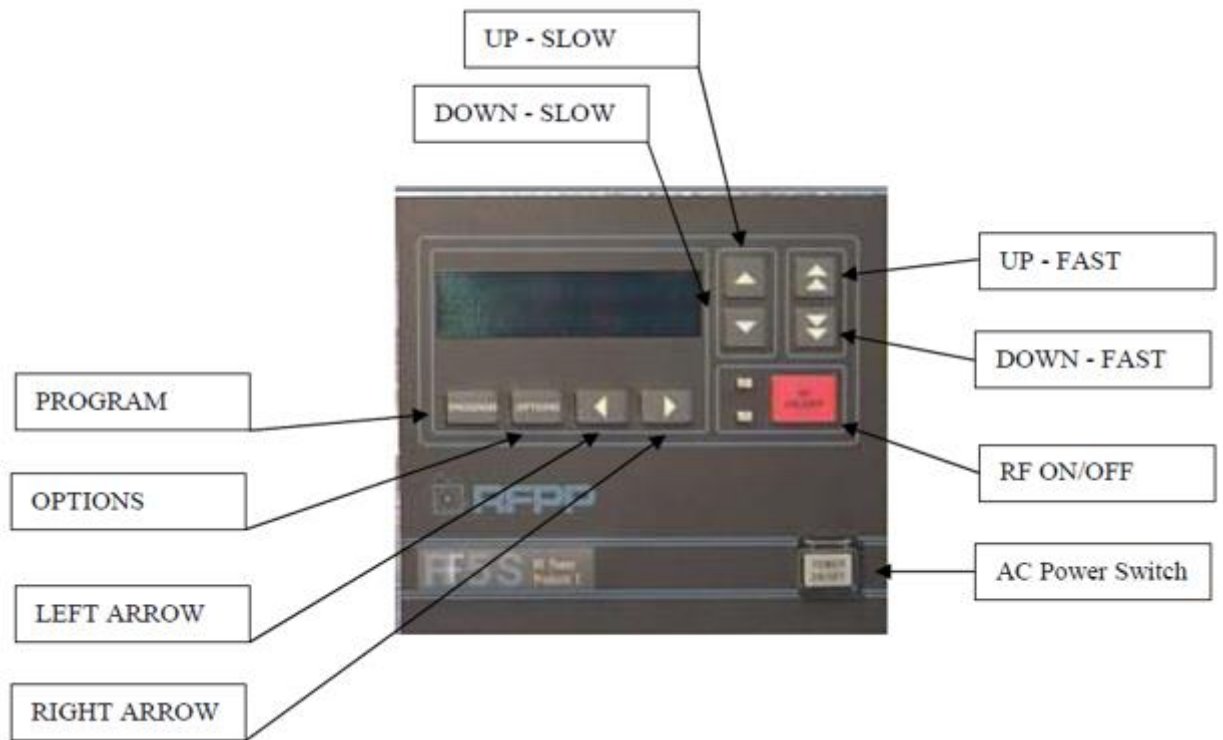


Figure 3.4: RF5S plasma production front panel.

We can use AC voltage about 240V to this device. The adjustment for the positions of the tune and load capacitors of an associated matching network are available on pins 100 (TUNE) and 100 (LOAD) for the analog interface connector.

In MHz machines, the plasma device is one electrode which is placed within the plasma chamber and is connected to the plasma production to produce 13.56 MHz of radio frequency. The RF power supply will be switched on when the pressure within the chamber achieves in low pressure thereby getting the process gases to be ionized.

3.1.2.2 Filament Heating Supply

The spiral with two arms filament is placed between the filament holders which are connected to a heating supply. The filament is heated to evaporate the metal catalyst, which is set inside the spiral part, for covering the substrates with thin film of metal and decompose the gases for a top down assembly growth.

The filament heating supply consists of a voltage regulator (IBC voltage regulator 1P-1kVA) with voltage range 0-250 V, thermal ammeter with range 60A, fuse and switch key. The voltage regulator supplies electrical current to the filament, while the ammeter measures the current flow. When the electrical current passes through the filament, it will encounter resistance leading to generating heat. A filament temperature can be adjusted by regulation the voltage.

A pyrometer (Reytek, Raynger, 3i) is used to measure the filament temperature. The detector of the pyrometer is stimulated by the incoming infrared energy and converts to a signal which passes to the circuitry leading to compute the filament temperature.

3.1.2.3 Substrate Holder Heating Supply

The heating of the substrate holder feeds the substrates to an appropriate temperature for deposition thin film of nickel, treatment by hydrogen plasma and growth the nanowires via decomposition of the gases. The cylindrical stainless steel substrate holder, which is put inside the reaction chamber, is connected to a heating supply.

The substrate holder heating supply consists clearly of a voltage regulator (IBC voltage regulator 1P-1kVA), a temperature controller (Taishio temperature controller TS-501), fuse and switch key. An insertion heater (Watlow Fire Rod cartridge heater) is used to connect the substrate holder with the heating supply. The cartridge heater provides superior heat transfer and uniform temperature to the substrate holder at high temperature.

The electrical power is supplied by the voltage regulator. Whereas, the temperature of the substrates is put in a specific value and controlled by the temperature controller. The temperature controller is connected with a thermocouple. The thermocouple acts as a temperature sensor and is placed inside the substrate holder to measure the real value of the substrate temperature.

3.1.2.4 Gas Supplies

Five gas cylinders, which are stored in a gas room, are used for preparing and growth processes. Two precursor gases SiH_4 (99.9995%) and CH_4 (99.99%) are used for synthesis of the nanowires. Hydrogen gas (99.999%) is used for dilution the precursor gases in growth deposition process. In addition, H_2 gas is also provided as a precursor gas for plasma treatment and preheating of coiled tungsten filament process. Helium gas (99.99%) serves as an addition gas to regulate the pressure which is resultant from the changing of H_2 gas. Purified nitrogen gas (99.999%) is used to clean a gas line, purge for SiH_4 gas and dilute with SiH_4 gas in vacuum pump. The SiH_4 gas cylinder is protected in a secured gas cabinet equipped with a control panel.

The gases come into the reactor through the gas lines. SiH_4 gas line is thicker the other gas lines that is used to pass SiH_4 and N_2 gases. A valve which controls the flow of gas through the gas line is installed in each gas line to prevent the gas flow from coming back to the gas cylinder. Metering valves are used to open or close the gas lines except SiH_4 gas line which is opened and close directly from the gas cylinder. Ball valves are used to control the amount gas flow from the source. Other metering valves inside the secured gas cabinet are used for purging and cleaning SiH_4 gas line. The flow rate of gas is adjusted and measured by using a mass flow controller (MFC) with unit reading of standard cubic centimeters per minute (sccm). The SiH_4 gas flow rate is controlled by an AALBORG MFC with flow range of 0-10 sccm, while the other gases flow rate can be varied from 0 to 200 sccm for H_2 and He gases and minus value for CH_4 gas. The gases are mixed by gas inlet tube before entering the reactor.

3.1.2.5 Water Supply

A cooling water is used to cool the system by flowing inside 0.25 inch stainless steel tubing which is twisted the outer body of the diffusion pump and chamber. The cooling water acts for prevention the corrosion due to vacuum pump and cooling the

system to the room temperature. The water is cooled by using a chiller into 24°C. The chiller is utilized for absorption the heat from the water to be cooled.

3.2 Vacuum System

The purpose of synthesizing the nanowires in HWCVD is achieved by a particular pressure. A very low pressure (high vacuum level) is required to perform a clean deposition environment and minimize contaminations in the sample. A vacuum system typically consists of three pumps which are connected to a chamber. Figure 3.5 shows the configuration of the vacuum system in this work. A rotary vane pump (model Edward E2M28) which acts as roughing pump is able to evacuate the reaction chamber until 1×10^{-3} mbar of the pressure. The roughing pump is also used to regulate the pressure during the growth processes. A diffusion pump (Edwards Hugh Vacuum LTD) accomplishes the vacuum level down until 1×10^{-9} mbar. Prior the synthesizing the nanowires, backing pump (BOC-Edwards E2m8) acts to support the diffusion pumps. The backing pump has an ultimate pressure of 1×10^{-3} mbar.

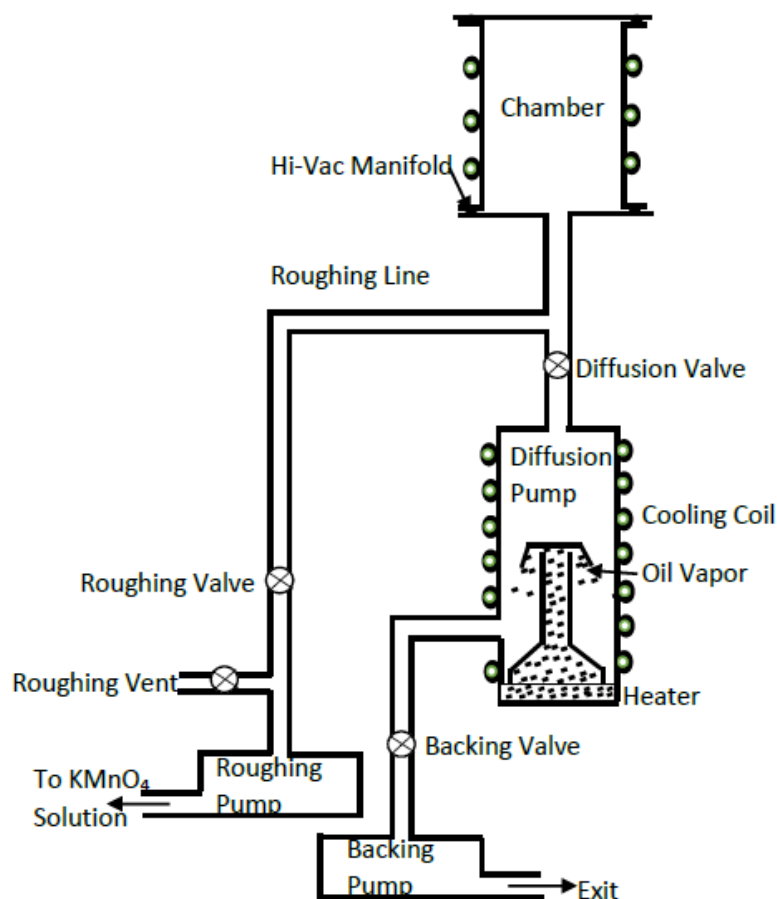


Figure 3.5: configuration of the vacuum pump system.

Additionally, one or more vacuum gauges are usually connected to the system to monitor pressure. Two thermovac (Leybold Vacuum TTR 91) are used as a gauge of the pressure. One of themovac records the pressure of the reaction chamber and the other measures the pressure which comes from backing pump. The thermovac transmitter gauge which is an active sensor for converting pressure to voltage by using thermal conductivity vacuum gauges which varies between 5×10^{-4} and 1000 mbar. While a penningvac (Oerlikon Leybold Vacuum PTR 225) gauge is used to monitor the pressure of the diffusion pump. Penningvac-transmitters PTR are active sensors and converts into a voltage. Penningvac gauge offers a wide measurement range of 10^{-9} to 10^{-2} mbar. The data of the pressure is shown in a display. Display two is used for the two thermovac

gauges, while display three is connected with the penningvac gauge. The displays are able to record the pressure range of 1×10^{-9} to 2000 mbar.

3.3 Materials Preparation

Prior growth process, materials mainly substrates and filament were prepared cleaning, drying and preheating. All substrate surfaces should be contaminated and must be cleaned. The pre-heating is useful for filament to increase the energy deposited and clean its surface.

3.3.1 Substrates Cleaning

The cut samples (1cm×1cm) were cleaned by a solvent clean, followed by a deionized water (DI) rinse. Deionized water removes nearly 100% of all elements other than the hydrogen and oxygen that form the water molecule. Acetone (C_3H_6O , $M = 58.08$ g/mol) and ethanol (C_2H_5OH , $M = 46.07$ g/mol) can dissolve organic substances such as grease, paint and glue. Hydrochloride (HCl) solution (37% HCl, $M = 36.49$ g/mol, diluted in H_2O_2 and deionized (DI) water in a ratio of 1:1:6) is used to remove residual metal contaminations. Ammonium hydroxide, also known as ammonia solution, (25% NH_4OH , $M = 17.03$ g/mol, diluted in H_2O_2 and DI water in a ratio of 1:1:5) can be used to remove organic contaminations and dissolved metal contaminations. Hydrofluoric acid (HF) is used remove native SiO_2 layer for Si substrate but it is not used in this work. Acetone and ethanol are flammable liquids that are stored far from a hotplate and any other source of heat.

The HCl, NH_4OH and HF are toxic and dangerous solution that are kept inside a laminar flow bench. For safety a pair of nitrile gloves are used and the laminar flow bench is switched on. An ultrasonic bath is used for cleaning to remove oil and gross dirt contaminations. Nitrogen gas is used for drying the substrates to prevent formation of water spots. For preserving the cleaning of the substrates, tweezers are used to hold and

a clean petri dish is used to keep the substrates. Figure 3.6 illustrates the steps of cleaning the glass and silicon substrates.

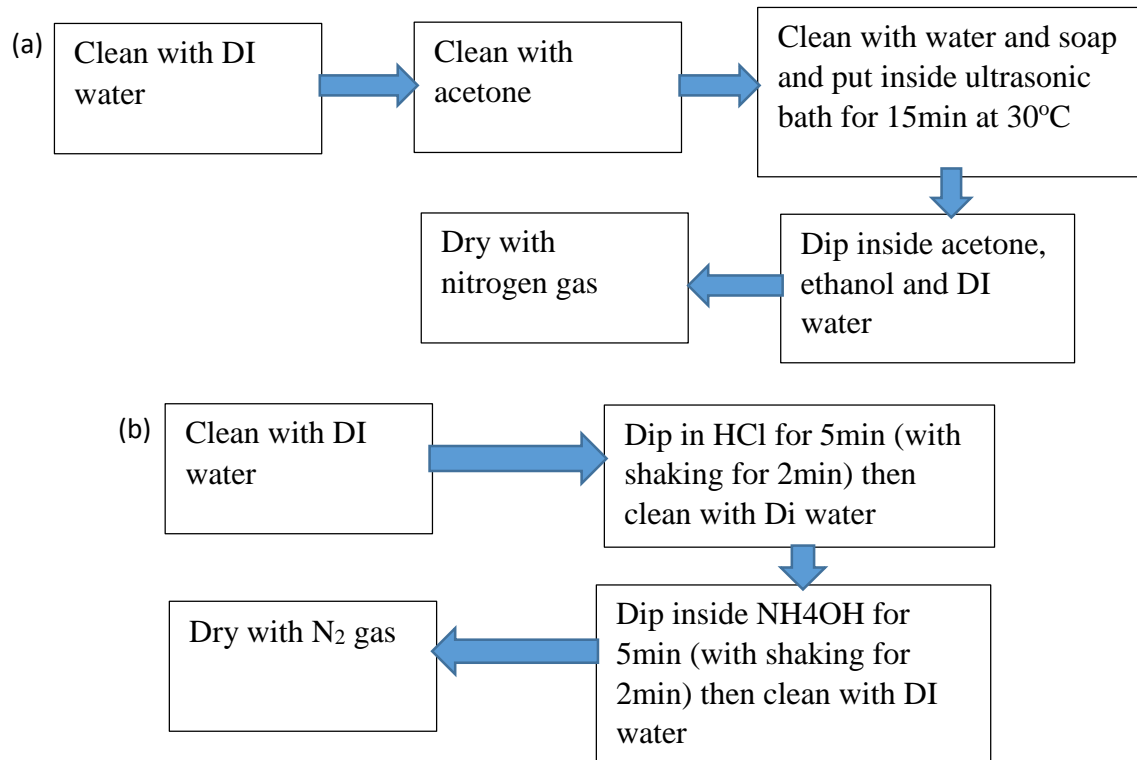


Figure 3.6: the cleaning steps of the substrates for (a) glass and (b) silicon.

3.3.2 Filament Preheating

After coiling the tungsten filament, acetone was used to clean the filament which was set between filament holders to be subjected to a pre-heating. The pre-heating is useful to increase the energy deposited in the filament during the resistive heating stage (AG Roussikh et al., 2006) and removes surface contaminations with using hydrogen gas. After evacuation of the system, the filament heating supply was set on 95 volt to heat the filament into 1600°C in existence 100sccm of hydrogen flow rate for 5 minutes. In this work, two filaments were pre-heated for metal evaporation and growth deposition.

3.4 Growth Processes

The growth of the nanowires was achieved by successive processes. Figure 3.7 shows the main stages for growth the nanowires.

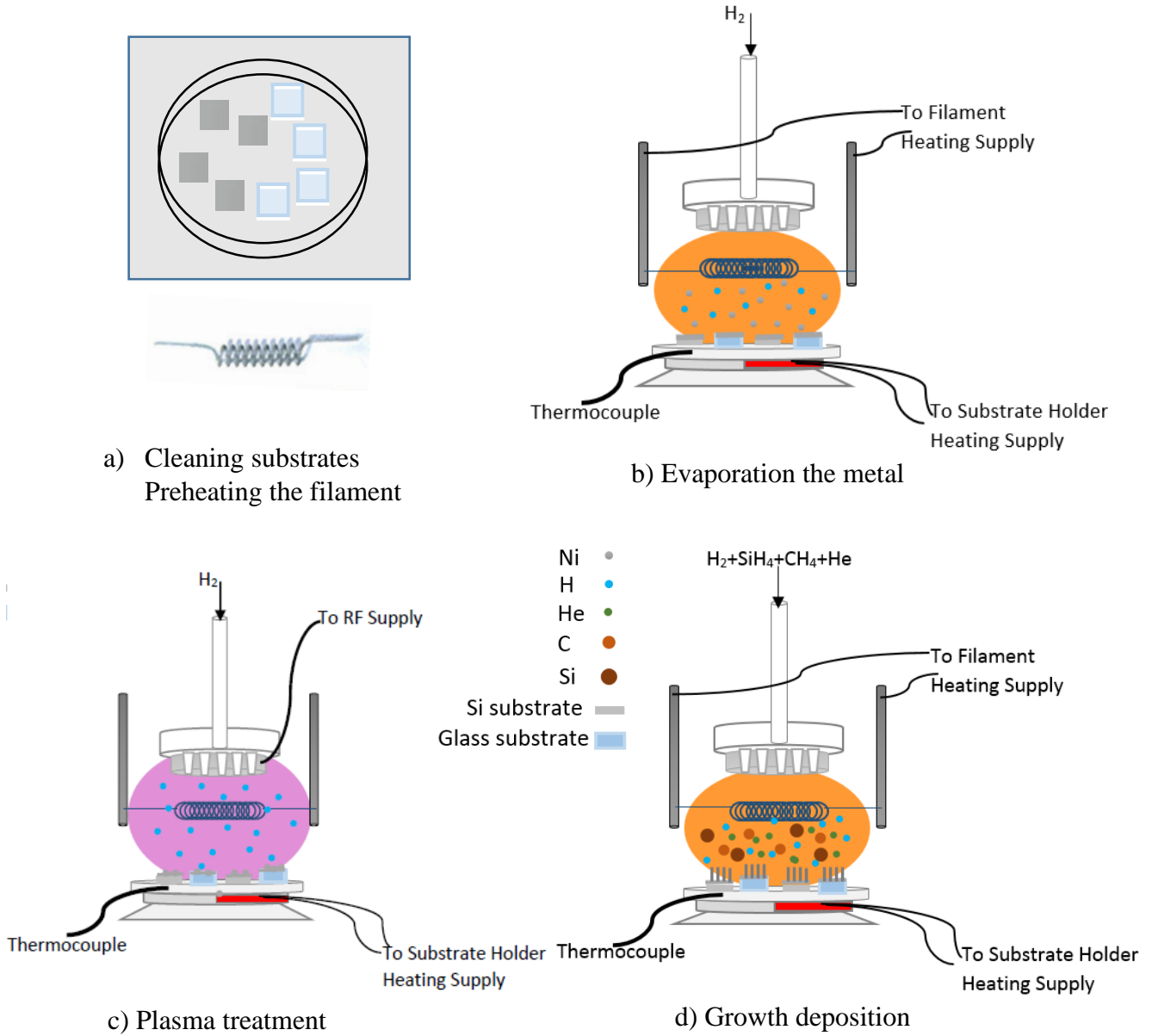


Figure 3.7: the main stages of growth the nanowires.

3.4.1 System Evacuation

Pumping the reaction chamber and clean lines of the gas are important to achieve a system evacuation. The system evacuation is first process to get a clean environment before deposition. Prior the evacuation of the system, the preparation materials were put inside the reaction chamber the cleaned substrate on the substrate holder and preheating filament between the filament holders. Then the reaction chamber was tightly sealed by bolts. The roughing, backing pumps were switched on and opened to evacuate the reaction chamber. The diffusion pump was switched on to heat an oil which was used to achieve high vacuum. The chiller and the two display were turned on. After one hour, the pressure reached to 10^{-3} mbar, the roughing pump was closed and the diffusion pump was opened for one hour to get high vacuum until 10^{-6} mbar. During the pumping of the reactor, the lines of the gas were cleaned by opening the ball valves for H_2 , CH_4 and He while the metering valves were closed which were connected to the gas sources. After cleaning lines, the ball valves was closed. That is very important to empty out the lines from a gas contamination before introducing the deposition gases into the reactor.

3.4.2 Substrates Heating

The substrate heating supply was turned on and the voltage was regulated into 75 volt then increasing to 110 volt after 20 minutes for growth deposition process with setting the temperature on $450^{\circ}C$ for growth deposition. Whereas, the voltage was turned on at 90 volt with setting the temperature on $150^{\circ}C$ for evaporation. This was followed by heating the substrates. The thermocouple acts as a sensor for the actual temperature of the substrates. When the actual temperature reached to required value, the substrates were heated for 10 minutes leading to stabilization temperature.

3.4.3 Thin Film Metal Deposition

A catalyst is used to increase in the rate of a chemical reaction with less energy. Nickel was used as a catalyst to induce the growth of the nanowires. A 1×6 mm nickel foil

was tightly hung on a coiled tungsten. When the temperature of substrates was 150°C in low pressure, the hot wire power supply was turned on at 95 volt for 5 minutes with 100 sccm of hydrogen flow rate to achieve a thin film on the substrates. The temperature of the filament reached to high temperature more than 1600°C. This temperature led to evaporate the nickel foil for deposition the thin film about 30nm of the thickness on the substrates.

3.4.4 Plasma Treatment

Prior growth deposition, the surface treatment of the coated substrates is important to synthesis the nanowires. The distance between the plasma device and the substrate holder was fixed in 4cm. The load and tune in matching network was adjusted on 23ohm and 100 turns, respectively. This treatment used H₂ plasma for formation metal nanoparticles. Table 3.1 illustrates the main conditions for plasma treatment which formed nanoparticles about 30nm in diameter.

Table 3.1: the main conditions for plasma treatment.

H ₂ Flow Rate (sccm)	Radio Frequency Power (Watt)	Pressure (mbar)	Substrate Temperature (°C)	Time (minutes)
100	5	0.75	450	10

3.4.5 Growth Deposition

Five samples were prepared one as a control sample without hydrogen flow rate and the others at different hydrogen dilutions of 50, 100, 150 and 200 sccm of hydrogen flow rates, in an increment of 50sccm. SiH₄ and CH₄ gases acted as precursor gases. The hot wire heating supply was switched on at 165 volt to achieve filament temperature more than 1900°C for 5 minutes. The substrate temperature, the distance between the filament and substrate holder were adjusted to 450°C, 2cm, respectively. The keeping of the gases pressure about 1 mbar can be done by varying of helium flow rate. The deposition

pressure was fixed at 3 mbar. The gases flow rate, hydrogen dilution and surface temperature that was noticed at growth deposition are tabulated in table 1. Whereas hydrogen dilution has been calculated from the gas flows measured by the MFCs by using the formula:

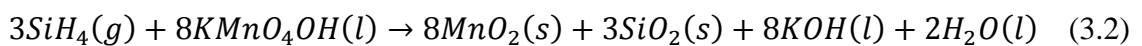
$$H\% = \frac{F_{H_2}}{F_{SiH_4} + F_{CH_4} + F_{He} + F_{H_2}} \times 100\% \quad (3.1)$$

Table 3.2: The gases flow rate, hydrogen dilution and the surface temperature at growth deposition.

Samples	Control	A	B	C	D
SiH ₄ Flow Rate (F_{SiH_4}) (sccm)	1	1	1	1	1
CH ₄ Flow Rate (F_{CH_4}) (sccm)	2	2	2	2	2
H ₂ Flow Rate (F_{H_2}) (sccm)	0	50	100	150	200
He Flow Rate (F_{He}) (sccm)	200	198	130	71	0
H ₂ Dilution (%)	0	20	43	67	99
Surface temperature (°C)	459	478	497	469	467

3.5 Post-deposition

After the deposition time, the residual gases were pumped out. This was followed by cleaning lines of the gases. The SiH₄ gas was purged by using three valves for cleaning line. The gas line was cleaned with flowing N₂ gas to dilute the SiH₄ and avoided the precipitation of residual SiH₄ gas on the walls of the tubing. The chemical reaction equation of SiH₄ clean line is as bellow:



The system was vented by roughing vent valve when the samples were cooled down to room temperature. The reaction chamber components were cleaned by using send papers and acetone to remove remnant deposition for the next deposition.

3.6 Characterization Techniques

The characterization techniques involved to study the physical behaviors and chemical components of the nanowires for a wide range of spectroscopy from macroscopic to microscopic level and from the surface to a few microns depth of the sample analysis.

3.6.1 Field Emission Scanning Electron Microscopy (FESEM)

The SEM uses a beam of electrons to produce a magnified image, unlike the optical microscope that uses light. The SEM produces highly magnified images (from 10X up to 300000X), with outstanding resolution (1-5nm) and large depth of field allowing for more of the sample to be focused at one time. The SEM mainly is used for analysis of the morphology characterization and presents an enlarged surface image on the monitor screen of the micro and nanostructures material. When the SEM uses a field emission gun for electrons source is named field emission scanning electron microscopy (FESEM), while other type of SEM uses thermionic guns. Figure 3.8 (a) shows the schematic diagram of the configuration of the SEM.

The FESEM was used in this work Hitachi SU 8000 Scanning Electron Microscope with voltage of 2 kilovolt, as shown in figure 3.8 (b). The FE gun which produced an electron beam with energy of a few hundred electron volt has higher brightness and cathode lifetime than the thermionic gun. Electromagnetic lens were used to focus the electron beam by applying magnetic field in a horizontal radial direction. Secondary electron detector was utilized for conversion into electrical signal and amplified the secondary and backscattered electrons produced from the sample. Display

was used to convert the detected and amplified secondary electron signal to brightness and provides an enlarged image.

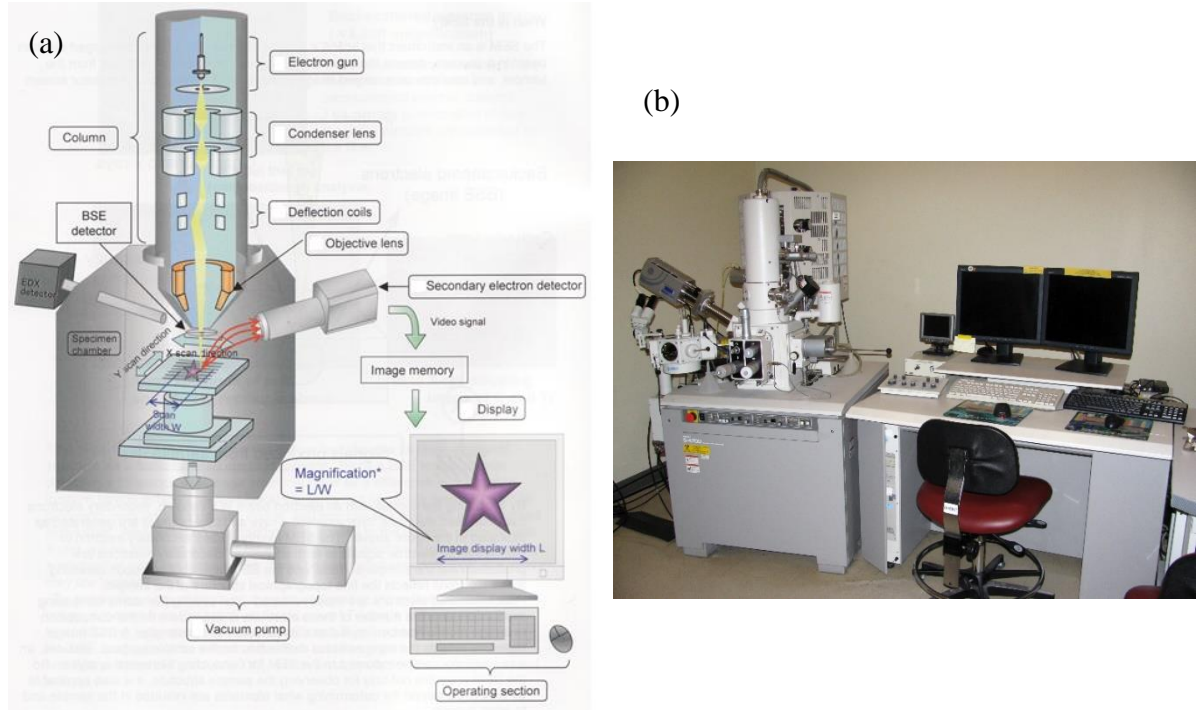


Figure 3.8: (a) schematic diagram of the configuration of SEM, (b) photograph of Hitachi S4700 SEM

3.6.2 High Resolution Transmission Electron Microscopy (HRTEM)

Transmission electron microscopy (TEM) is an important technique for microstructural analysis. Atomic structure can be investigated by high resolution transmission electron microscopy (HRTEM) for determining the crystalline and amorphous characterization of the sample. HRTEM has been developed to achieve the highest image quality and the highest analytical performance. Generally it consists, as shown in figure 3.9 (a), of electron gun, condenser lens for focusing the electron beam into the sample, objective, intermediate and projector lens for image focusing, and fluorescent screen. In this work, the type of HRTEM is JEOL JEM-2100F which is seen

in figure 3.9 (b). The naowires were put on the coper grid PK/50 for this technique scanning. The accelerating voltage was set on 200 kV.

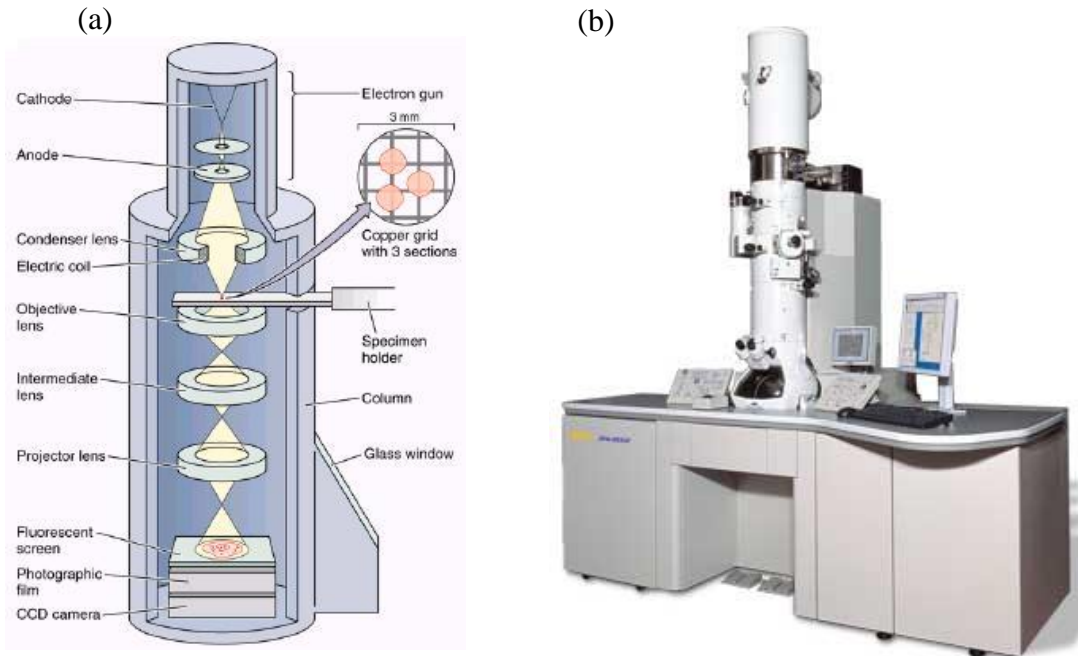


Figure 3.9: (a) schematic diagram of the configuration of HRTEM, (b) photograph of JEOL JEM-2100F HRTEM

3.6.3 Energy Dispersion X-Ray (EDX)

Energy dispersion X-ray identifies the chemical compositions of the sample and determines the quantities of these compositions. Basically, it consists of the source of incident electrons, pole piece for focusing the beam of electrons and detector, as shown in figure 3.10 (a). The EDX detector is designed to view samples at fixed work distance (WD). The highest take off angle (TOA) is describe to minimize the effects of absorption by the topography of the sample. EDX detector can be attached in a SEM or TEM to effectively collect the X-ray radiation from the sample. In this work, HAAF/STEM and Oxford EDS was used as a detector of characteristic X-ray. This detector is shown in figure 3.10 (b).

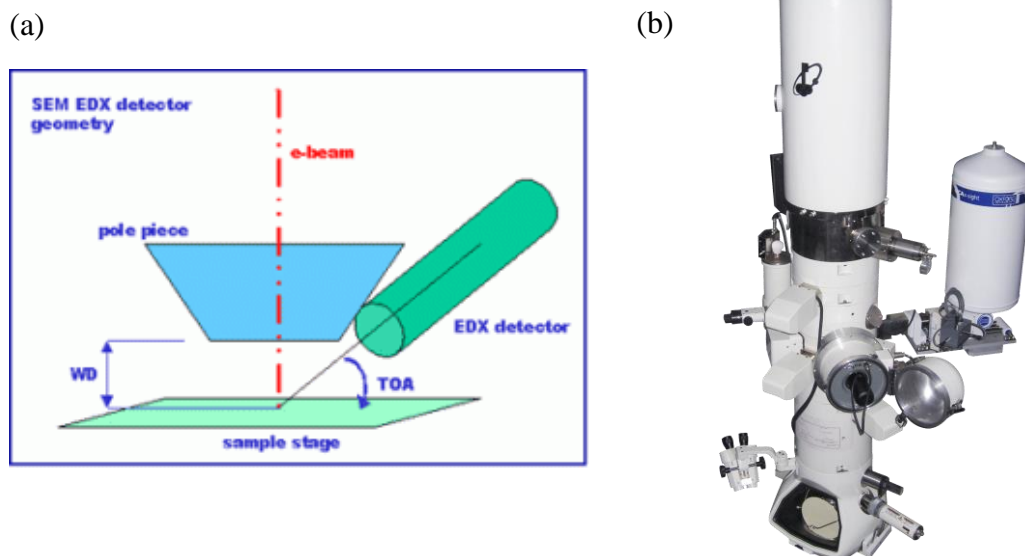


Figure 3.10: (a) schematic diagram of the configuration of EDX, (b) photograph of HAAF/STEM and Oxford EDS.

3.6.4 Micro-Raman Scattering Spectroscopy

Micro-Raman spectroscopy is used to determine the information about the structure of molecules, including crystallinity, crystalline to amorphous phase transition and vice versa. A laser source is used as incident light to irradiate onto the sample. Most of laser radiation is scattered by the sample in the same wavelength of the incident light (Rayleigh scattering) and small proportion-approximately one photon out per million- of a wavelength that is shifted from the incident light wavelength (Raman scattering). The configuration of micro-Raman spectroscopy is shown in figure 3.11 (a). The spectrum is accomplished by focusing the Raman scattered light onto a diffraction grating, which splits the beam into its constituent wavelengths. These wavelengths are directed onto a charge-coupled device (CCD) detector.

In this work Renishaw inVia Raman Microscopy which is illustrated in figure 3.11 (b) was used to study the structural properties by using Argon ion laser with wavelength of 514nm. CCD camera was chosen for the detector in Raman spectroscopy with grating of 2400 line/mm. A laser power of 10% with one accumulator of the range 100 to 2000 Raman shift/cm⁻¹ was exposed to the sample for 30 second.

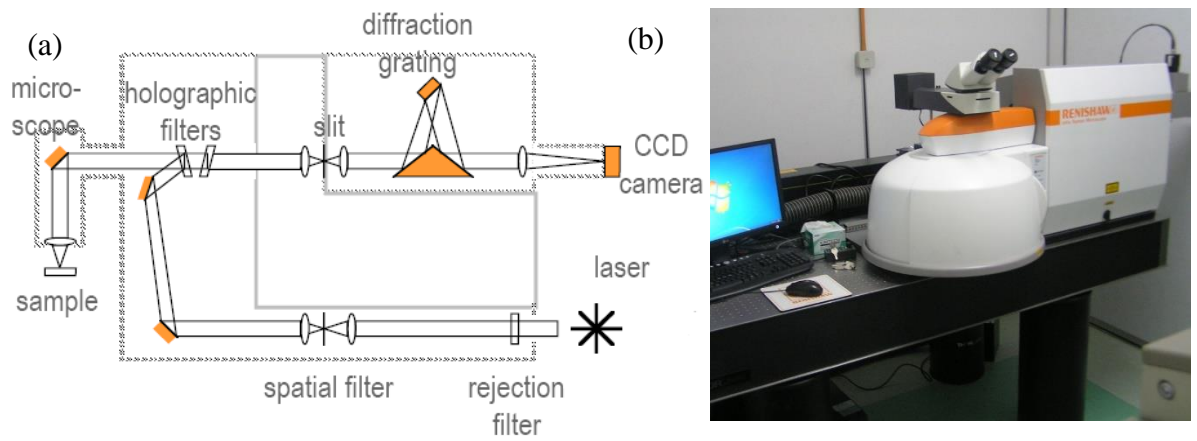


Figure 3.11: (a) schematic diagram of the configuration of micro-Raman spectroscopy, (b) photograph of Renishaw inVia Raman Microscopy.

3.6.5 Photoluminescence (PL)

Photoluminescence spectroscopy is utilized mainly to investigate the optical properties of impurities in semiconductors. The basic elements of the PL spectroscopy, as shown in figure 3.12, are an optical source, a monochromator and detector. The laser source beams which have energy more than the optical band gap is focused on the sample with using lens. The emitted light from the sample is collected by lens to be selected by monochromator and are directed onto detector. In this work, Renishaw inVia Raman Microscopy, the same device was used for Raman spectroscopy, was utilized to produce sample luminescence. A HeCd laser with wavelength of 325nm and 100% in power at range from 400 to 900nm was exposed onto the sample for 30 second. CCD was selected for detector with grating of 1200 lines/mm.

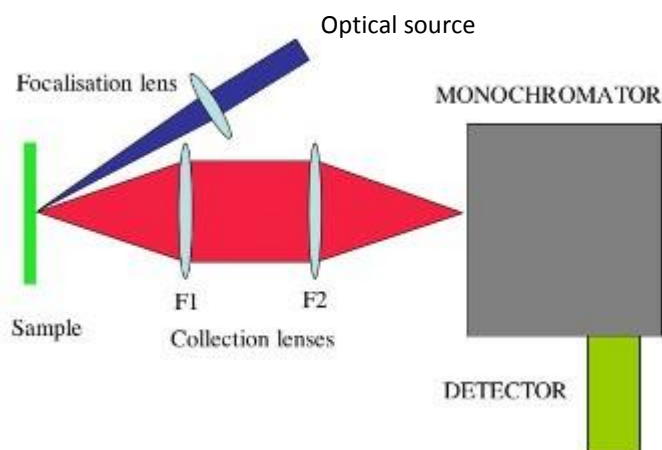


Figure 3.12: basic scheme of a PL spectroscopy.

3.6.6 X-Ray Diffraction (XRD)

X-ray is invisible and highly penetrating electromagnetic radiation. X-ray diffraction is generally non-destructive analytical technique and used for determining the crystal structure, chemical composition and physical properties of the material and thin film. The diffraction depends on the crystal structure and the wavelength. This technique as seen in figure 3.13 (a) consists of a monochromatic X-ray radiator and a detector, which are placed on the circumference of a circle centered on the sample. In this work, the type of used XRD was PANalytical EMpyrean, as shown in figure 3.13 (b), with target material of Cu $K_{\alpha 1}$ of wavelength of 1.540598\AA . The incident angle “omega” was fixed at 0.5° , where 2θ is the scan angle with scan range $20\text{-}80^\circ$. The step, counting, net time and step size were set on 3 s, 16 min, 1h and 0.026° , respectively. The voltage and the current of the scan operation were fixed at 40kV and 40mA.

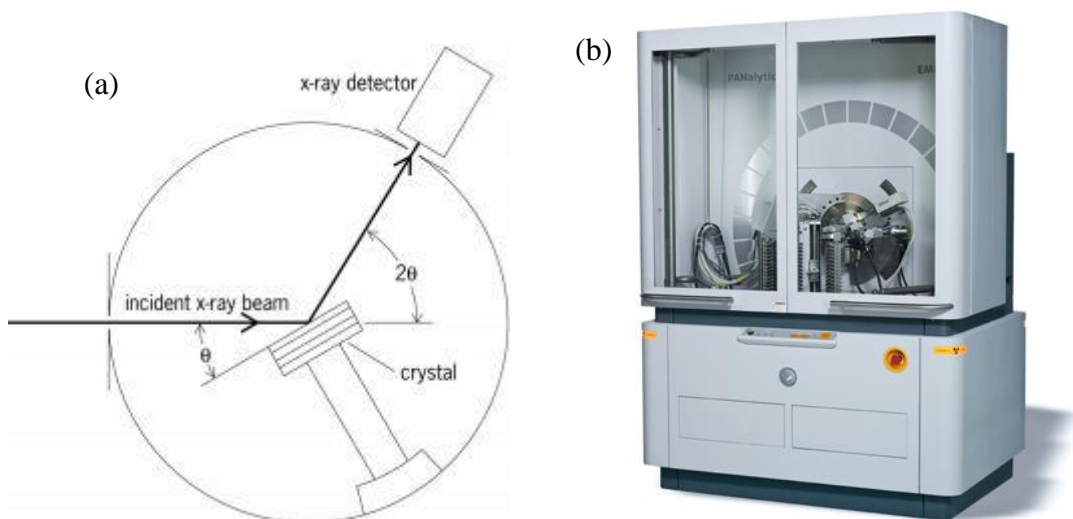
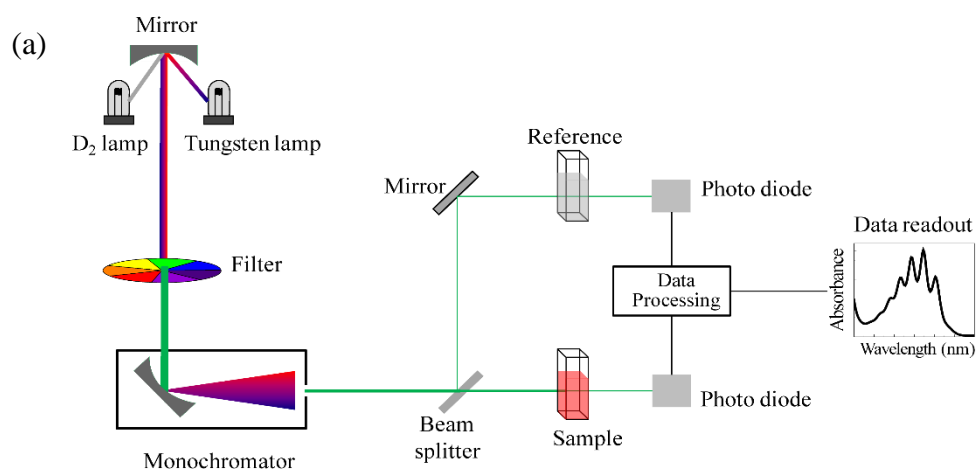


Figure 3.13: (a) X-ray diffracted beam path in $\theta/2\theta$ mode (b) photograph of PANalytical EMPyrean X-ray diffraction.

3.6.7 UV/VIS/NIR Spectrophotometer

The spectrometer is capable of performing transmittance, absorption and reflectance measurements of solid and liquid sample. These measurements are used to extract the optical properties of the materials. For reflectance, the spectrophotometer measures the intensity of light reflected from a sample (I), and compares it to the intensity of light reflected from a reference material (I_0). The ratio I/I_0 is called the reflectance, and is usually expressed as a percentage (%R). The basic parts of a spectrophotometer are a light source, a holder for the sample, a diffraction grating in a monochromator or a prism to separate the different wavelengths of light, and a detector as shown in figure 3.14 (a). The radiation source is often a Tungsten filament (300-2500 nm), a deuterium arc lamp, which is continuous over the ultraviolet region (190-400 nm), Xenon arc lamp, which is continuous from 160-2,000 nm; or more recently, light emitting diodes (LED) for the visible wavelengths. The detector is typically a photomultiplier tube, a photodiode, a photodiode array or a charge-coupled device (CCD). In this work, UV/VIS/NIR spectrophotometer-V-570- JASCO SLM-468-ALPHA ANALYTICAL (M) SDN.BHD was used to obtain the reflectance spectra of the nanowires, as seen in figure 3.14 (b). The

range of the wavelength, band wide and the scanning speed were fixed at 2200-220 nm, 2 nm and 1000nm/min, respectively, with fast response.



(b)



Figure 3.14: (a) schematic diagram of the configuration of UV/VIS/NIR Spectrophotometer, (b) photograph of UV/VIS/NIR spectrophotometer-V-570- JASCO SLM-468.

CHAPTER 4

RESULTS AND DISCUSSIONS

4.1 FESEM Analysis

The surface morphologies of Ni-catalyzed NiSi/SiC core-shell nanowires grown by HWCVD at different hydrogen dilutions are shown in figure 4.1. High density of nanowires uniformly distributed on the substrate for the sample grown without hydrogen dilution. These nanowires demonstrated relatively better uniformity and alignment as compared to other samples. The estimated average length and diameter of the nanowires from the FESEM images are approximately 792 and 253 nm respectively. Furthermore, the surface of the nanowires showed relatively smoother than other samples. No hydrogen reduces the growth sites formation on the nanowire surface which can prevent the radial growth that usually happen in the CVD growth. Introducing of hydrogen dilution up to 43 % enhances the growth of the nanowires. The length and the diameter of the nanowires increases and decreases respectively. This could be due to the hydrogen etching effect sufficiently maintaining the surface diffusion of Si-rich species and C-rich species into the Ni nanoparticles for the nucleation of the nanowires. Moreover, increasing of hydrogen dilution enhances the gas phase reactions and therefore leads to generation of more Si-rich species and C-rich species impinge on the growth surface (Kim & Anderson, 2005). Formation of the agglomerated grains as shown in the inset for the samples grown at 20 % of hydrogen dilution reveals a radial growth of the nanowires. This radial growth is due to the formation of the growth sites created by hydrogen etching effect attributed to the side nucleation on the surface of the nanowires. Increase in hydrogen dilution reduces the formation of the agglomerated grains attributed to the enhancement of the gas phase reactions which increase the surface diffusion of the growth precursors. However, the enhancement of the gas phase reactions attributed to the hydrogen dilution could

probably leads to the film growth condition instead of nanowires growth as can be found in the samples prepared at 99 % hydrogen dilution.

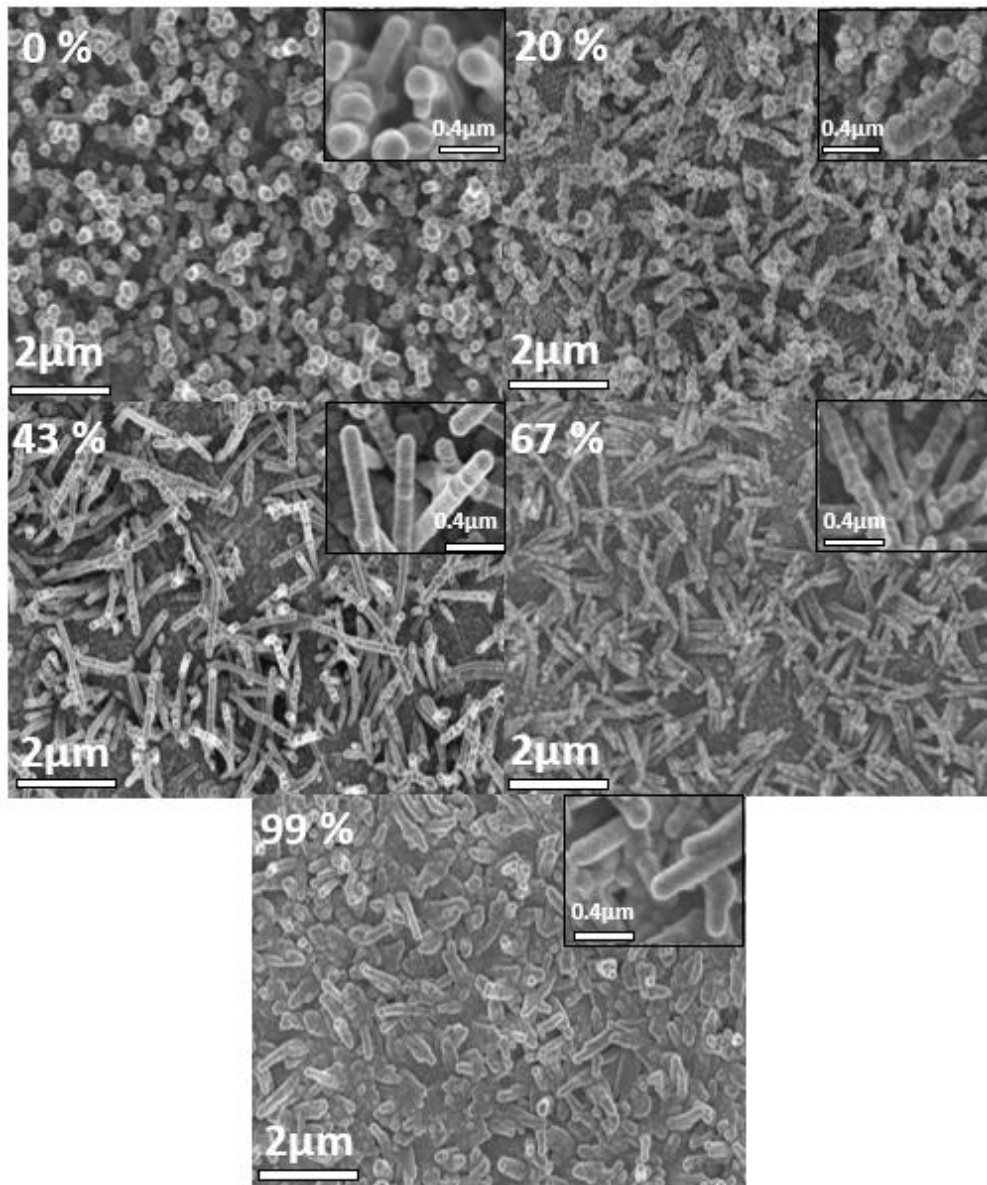


Figure 4.1: FESEM of NiSi/SiC core-shell nanowires prepared by HWCVD at different hydrogen dilutions. Inset of each image a high magnification of FESEM images.

Figure 4.2 shows the variations of the length and diameter with different hydrogen dilutions. The curve of the length shows a gradual increasing from 0 to 43 % then decreasing to 99 %, while the curve of the diameter shows decreasing with increasing the hydrogen dilutions until 67 % then increasing at 99 %. This indicates that the increasing and decreasing of the length are accompanied by the decreasing and increasing of the diameter in the nanowires at different hydrogen dilutions, respectively. The longest length

of the nanowires could be attributed to the highest surface temperature which sufficiently provide high energy for the diffusion and precipitation of the nanowires. The number density decreased with increasing in hydrogen dilution, as illustrated in an inset figure. This decreasing of the density is due to the film growth condition instead of the nanowires growth.

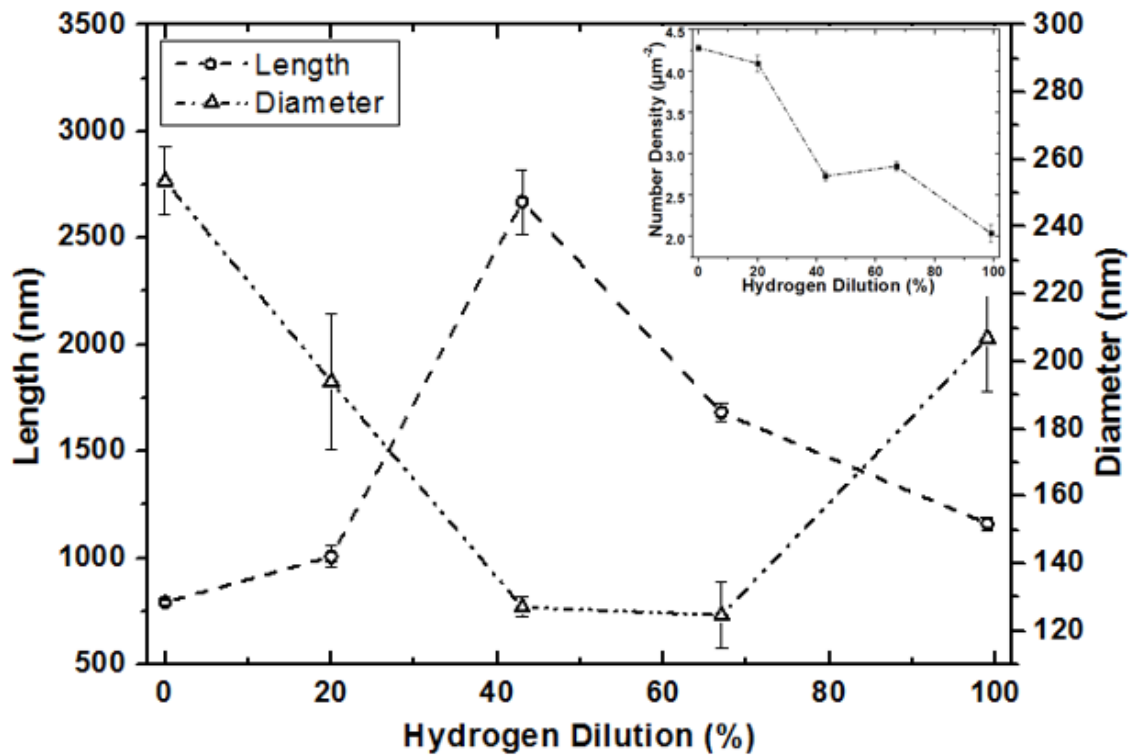


Figure 4.2: the variations of the lengths and diameters on the FESEM images against the hydrogen dilutions, an inset figure shows the variation of number densities with hydrogen dilutions.

4.2 TEM and STEM/EDS Mapping Analysis

The microstructure of these nanowires was further obtained by TEM as shown in figure 4.3. A single nanowire of the sample prepared at hydrogen dilution of 43 % was selected for this TEM measurement. As shown in figure 4.3 (a), these nanowires clearly consist of core-and shell with the diameter of 14.8 ± 3 and 105.1 ± 5 nm, respectively. Some dark particles are found near the core nanowire indicates to an out-diffusion of the NiSi core forming large NiSi grains. The out-diffusion of the core nanowires was previously reported in elsewhere (Nazarudin et al, 2015, Hannon et al, 2006). Obviously, these NiSi grains contributed to the formation of the bumps as observed in the FESEM

images as shown in figure 4.1 for the samples grown at above 20 % hydrogen dilution. Furthermore, small particles also are observed randomly distributed in the shell of nanowire. These nanoparticles are nano-crystallites embedded within an amorphous matrix of the shell that illustrated in high magnification images as shown in figures 4.3 (b) and (c). In figure 3(a), the structure of the core cannot be clearly presented due to the thickness of the shell about 45.1 ± 2 nm. According to our previous studies, the NiSi core was revealed a single crystalline structure (Nazarudin et al, 2014). Figure 4.3 (c) illustrates an increase in magnification of the image in figure 4.3(b). HRTEM scan at near the edge of the core nanowire reveals the presence of 3C-SiC nano-crystallites embedded within an amorphous matrix. The estimated lattice spacing was about 0.25 nm corresponding to SiC (111) crystallographic plane (figure 4.3 (d)). The growth direction of [111] was further revealed by a fast Fourier transform (FFT) as shown in an inset image. The estimated crystallite size average is approximately 4.05 ± 0.77 nm. The presence of NiSi near the tip of the nanowires surrounded by amorphous SiC shell indicates the Ni catalyzed the growth of the nanowires as shown in figure 4.3(e).

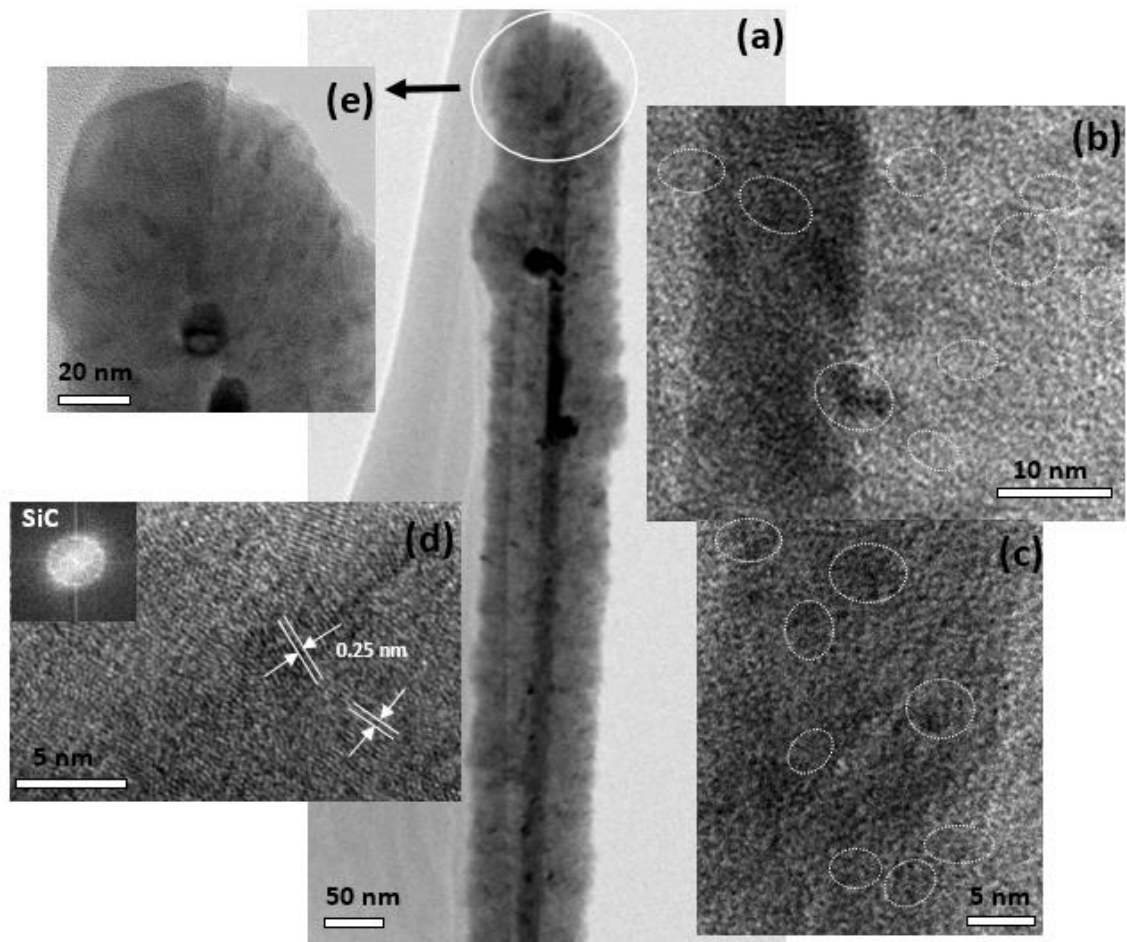


Figure 4.3: (a) TEM image of the NiSi/SiC core-shell nanowires grown by HWCVD at hydrogen dilution of 43 %; (b), (c), (d), (e) and (f) show HRTEM images of the core-shell, near the edge of the core, shell and tip of the nanowires as labelled in the figure. Inset image (d) shows the FFT of the shell of the nanowire.

The compositions of the nanowires were further investigated by STEM/EDS elemental mappings using a HAADF detector in the TEM, as shown in figure 4.4. Figure 4.4 (a) depicts a dark-field STEM image of a single nanowire. The solid pink box indicates a scan area for the EDS elemental mappings. The compositions of the nanowire were demonstrated by the EDS maps as shown in figure 4.4 (b-e) correspond to the Ni, Si, O and C $K\alpha$ maps respectively. Clearly, the presence of Ni along the centre axis of the nanowire confirms the formation of the NiSi nanowire core, as shown in figure 4.4 (b). Some Ni bumps appear near the centre axis indicates the formation of the NiSi particles due to the out-diffusion of NiSi core which was noticed in the TEM images as shown in figure 4.3 (a). The Ni nanoparticle supports the Ni catalyzed growth of these core-shell

nanowires by HWCVD. High density of Si can be observed with uniform distribution along the nanowires as shown in figure 4.4 (c) indicates its contribution of the formation the core and shell of the nanowire. Less amount and uniform distribution of O appeared along of the nanowire which indicates the radical growth of the nanowires as shown in figure (d). The C map showed the presence of C along the length the nanowires as shown in figure (e). The elemental profile of a single nanowire at the stem was obtained by the STEM line scan with HAADF detector and is illustrated in figure 4.4 (f) and (g). It is shown that from the vertical line scan, the density of Si is at maximum along the nanowire which reveal the contribution of Si to form the core and shell of the nanowire. A small density of Ni appears at the centre of the nanowires. The distributions of Si and Ni at the centre support the NiSi core nanowire. On the other hand, a low density of C is showed along the nanowires with slightly lower at the centre. The distributions of C by the EDS line scans indicate the formation of SiC shell. A very small amount of O is also found on the nanowire surface indicates the oxidation effects of the nanowire.

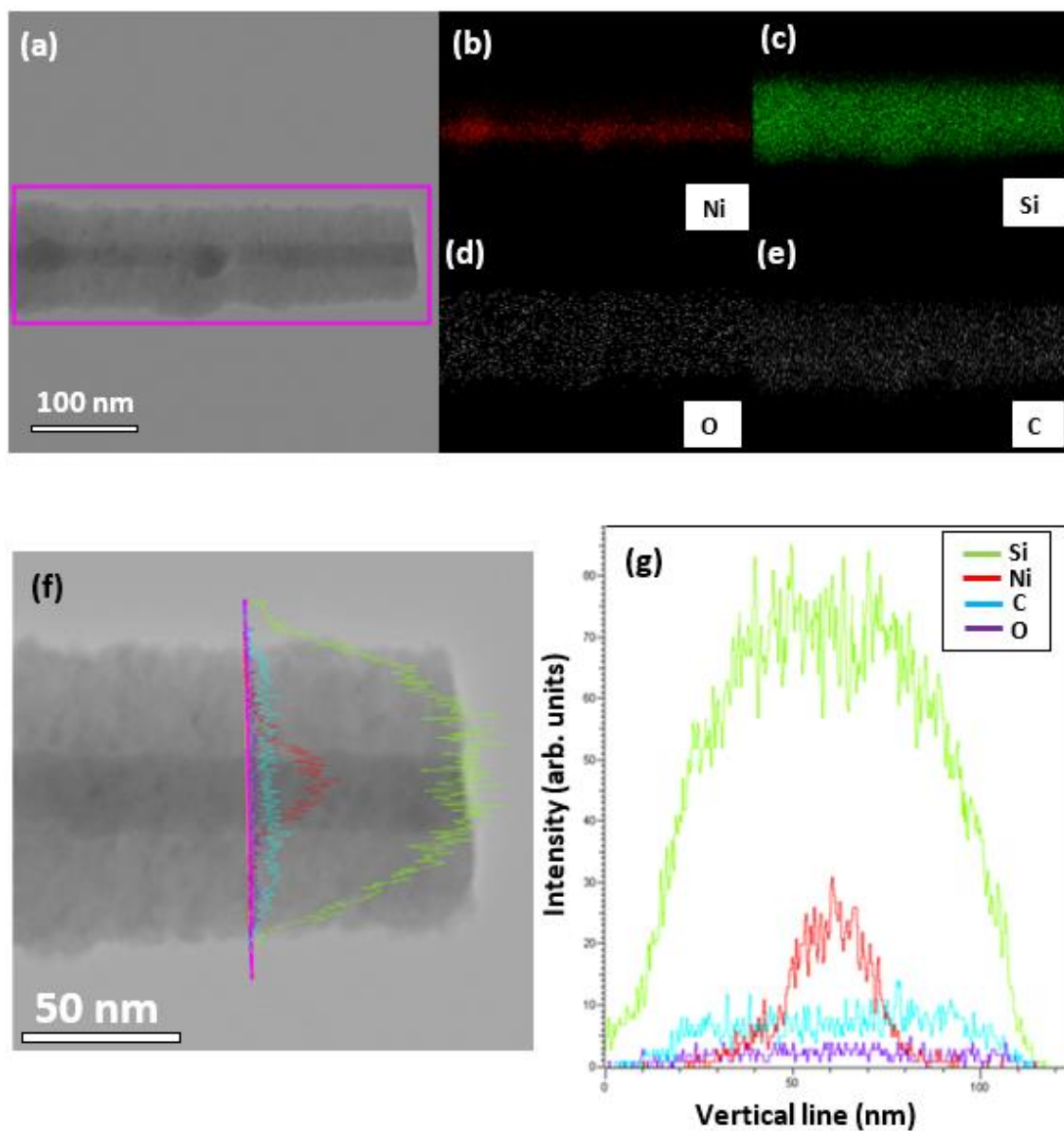


Figure 4.4: (a) Dark-field STEM image of the NiSi/SiC core-shell nanowires grown by HWCVD at hydrogen dilution of 43 %. The solid pink box in (a) shows the scanning area for the elemental maps on the single nanowire; (b)–(e) represent each EDS element map of the core-shell nanowire; (f) STEM/HAADF image of a typical single nanowire with an inset of EDS elemental profile overlay with the image; (g) EDS line scan of the elemental profile of a single nanowire at the stem.

4.3 Raman Analysis

Figure 4.5(a) shows the Raman scattering spectra of the nanowires prepared by HWCVD at different hydrogen dilutions. These Raman spectra mainly consists of Si, NiSi and SiC Raman excitation bands as illustrated in the figure. Figure 4.5(b) presents typical Raman excitation bands of Si at 150, 300, 380 and 480–520 cm^{-1} , which correspond to transverse acoustic (TA), longitudinal acoustic (LA), longitudinal optical (LO) and transverse optical (TO) modes, respectively (Sirleto et al, 2012; Jasinevicius et al, 2007). Moreover, the TO band of Si can be divided into two components which are TO_1 mode at 480 cm^{-1} and TO_2 mode at 520 cm^{-1} , associated with amorphous and crystalline Si phases, respectively. The appearance of the sharp Si TO_2 excitation bands for the nanowires, which starts from 20 % to 67 %, could indicate a formation of crystalline Si in the nanowires. The transition from amorphous to crystalline Si with increase in hydrogen dilution implies a crystallization of the nanowires. This crystallization increases with increase in hydrogen dilution up to 43 %. This effect was reported by Zhai et al (2014) attributed to the hydrogen etching effect by removing the weak Si-H₂ bonds and forming rigid Si-Si bonds. A small amount of hydrogen comes from SiH₄ and CH₄ decomposition is not sufficient to induce crystallization due to the stronger energy bond of Si-H over than Si-H₂. The crystalline Si TO_2 excitation band shows a slight red-shifted to 519 ± 0.1 and 517 ± 0.1 cm^{-1} and asymmetric broader about 20 ± 0.1 and $20.9 \pm 0.1 \text{cm}^{-1}$ at 43 % and 67 %, respectively, as compared to single crystalline Si with TO_2 excitation band at 520 ± 0.1 cm^{-1} with the width of 12.6 ± 0.1 cm^{-1} at 20 %. This red shifted and broadening are due to more enhancement to react the Si with Ni and C (Dolgiy et al, 2013). At 99 %, a weak and broad peak at 400-500 cm^{-1} , which indicates that is a low density amorphous (LDA) formation of a-Si, appeared due to high compression of hydrogen dilution. The same observation reported by Deb et al (2001) for the increasing in the compression of a porous silicon. A small and broaden

peak centred on 970 cm^{-1} which associated with a second order Si TO band (2TO) were observed at 20 % (Bi & Feng, 2006).

The appearance of broaden and asymmetric peak at 193 cm^{-1} associated to NiSi phase is observed in the sample prepared without hydrogen dilution which combined with 150 cm^{-1} peak (Bhaskaran et al, 2009; Lee et al, 2004). This peak changes to more narrow at 99 %. The presence of NiSi peak in the Raman spectra comes from the formation of NiSi nanoparticles on the surface of the nanowires due to NiSi out-diffusion. The presence of 215 cm^{-1} excitation band at 43 % reveals the formation of Ni₂Si phase (Bhaskaran et al, 2009; Lee et al, 2004). The changes of the phase from NiSi to Ni₂Si indicate an increasing of Ni diffusion into the NiSi nanoparticles during the initial growth of the nanowires (Kim & Anderson, 2005). The enhancement of the Ni diffusion rate could be attributed to the increase in surface temperature during the deposition. The shifted of the peaks at 196 and 217 cm^{-1} of NiSi and Ni₂Si phases, respectively, toward lower frequency, 193 and 215 cm^{-1} , respectively, are due to the quantum confinement effect or strain field caused by the shell. The same shifted effect was observed by Lee et al (2004). A small and broad excitation band at 371 cm^{-1} is observed at 99 % which corresponds to NiSi₂ phase (Lund et al, 2014). The change of the phase NiSi phases indicates to increasing of the decomposition rate. An increase in hydrogen dilution enhances the Raman excitation band of SiC to appear at 776 and 900 cm^{-1} in the nanowire which belong to TO and LO modes, respectively (Zhuang et al, 2012; Cui et al, 2011). The appearance of SiC phase reveals a formation of 3C-SiC nano-crystallites embedded with its matrix. The red-shifts of the SiC excitation bands and the broadening of the bands as compared to the bulk 3C-SiC crystal (Feng et al, 1988) own to the quantum confinement effects of the SiC nano-crystallites (Zhang et al, 1999). Therefore, the formation of amorphous SiC is attributed to the shell nanowires.

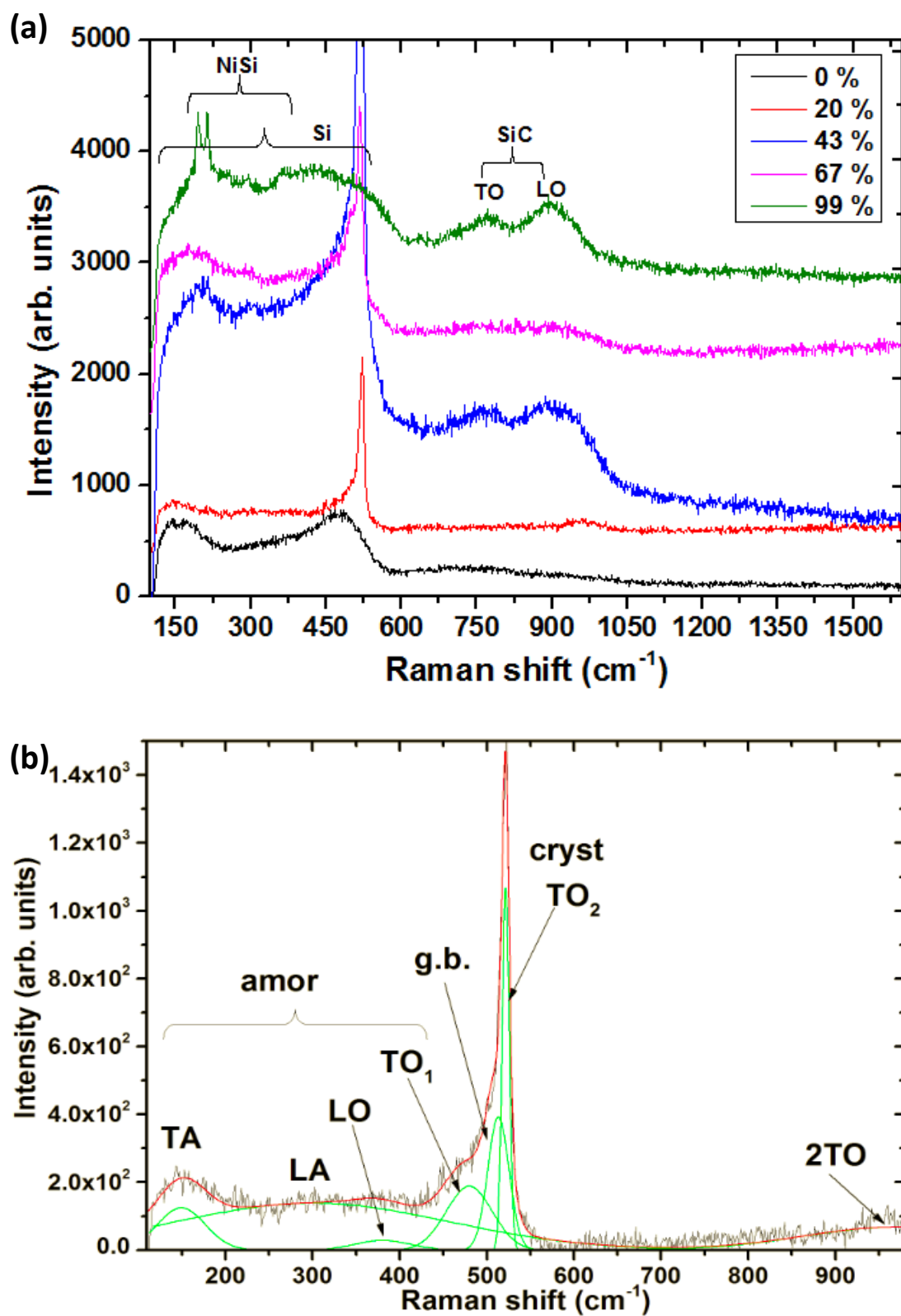


Figure 4.5: (a) Raman scattering spectra of NiSi/SiC nanowires prepared by HWCVD at different hydrogen dilutions; (b) Si phonon modes at Raman scattering of the nanowires prepared at 20 % which the decomposed components are labelled as amorphous (amor), grain boundaries (g.b.) and crystalline (cryst).

4.4 XRD Analysis

Figure 4.6 illustrates the XRD patterns of the nanowires prepared on silicon substrates by HWCVD at different hydrogen dilutions. As can be observed from the figure, the XRD patterns of the nanowires mainly exhibit Si, NiSi phases and SiC diffraction peaks. The Si diffraction peaks are located at 28.4, 47.3, 56.1 and 69.1° corresponding to c-Si with the orientations of (111), (220), (311) and (400) planes, respectively, according to JCPDS card number 01-089-2955 (Chong et al, 2011; Wu et al, 2011). The Si diffraction peaks at (220) and (311) are dominant in the spectrum of different hydrogen dilutions. Decreasing the peaks of c-Si at prepared sample without hydrogen dilution and at 99 % of hydrogen dilution indicated to amorphous Si. XRD patterns of the nanowires exhibit diffraction peaks of NiSi at 23.1, 31.6, 31.8, 34.2, 36.1, 44.3, 45.8, 47.3, 47.7, 51.4, 55.0 and 75.3°, which correspond to orthorhombic NiSi orientations of (101), (011), (002), (200), (111), (210), (112), (211), (202), (103), (301), and (114), respectively, according to JCPDS card number 00-038-0844. Most of NiSi diffraction peaks appeared at prepared sample without hydrogen dilution are due to highly diffusion of Ni with Si and three small peaks appeared at 99 %. At 20 %, the second phase of NiSi diffraction peaks were observed at 39.5, 42.4, 43.6, 45.5, 48.9, 53.4 and 53.6° that correspond to orthorhombic Ni₂Si orientations of (211), (310), (021), (301), (002), (320) and (203), respectively, according to JCPDS card number 01-073-2092. The third phase of NiSi, which is Ni₃Si₂, diffraction peaks for orthorhombic structure located at 28.0, 28.8, 30.6, 34.0, 42.8, 45, 45.1, 45.9 and 53.0° orientated at planes of (112), (131), (022), (222), (422), (242), (223), (313) and (260), respectively, according to JCPDS card number 00-065-1428, which mostly appeared at 43 %. With increasing hydrogen dilution, the decomposition rate increases in NiSi phase due to the enhancement of the hydrogen atoms that leads to Ni₁₃Si₁₂ diffraction peaks to appear at 67 % located at 30.4, 42.9, 43.9, 48.6, 51.3 and 52.4° in orientations of (112), (204), (212), (205), (214) and (116), respectively,

according to JCPDS card number 00-024-0524. Two diffraction peaks of $\text{Ni}_{13}\text{Si}_{12}$ (214) and (116) appear at 99 %. Also the diffraction peaks for NiSi_2 appear at 56.0 and 69.5° in orientations of (119) and (2011), respectively, according to JCPDS card number 00-003-1094. The appearance of different NiSi phases at 99 % may be due to more compression of hydrogen by producing Si-rich and C-rich (Zhai et al, 2014) and high diffusion of Ni in Si crystallite (Tanaka et al, 2001), which agrees with Raman spectrum. The appearance of two small diffraction peaks are observed at 43, 67 and 99 % located at 35.7 and 41.4° indicates a formation of nano-crystallites of 3C-SiC embedded within an amorphous matrix in orientations of (111) and (200), respectively, according to JCPDS card number 00-065-0360. The change of NiSi phases of the core and the interaction phase of the shell were observed by the increasing of hydrogen dilution.

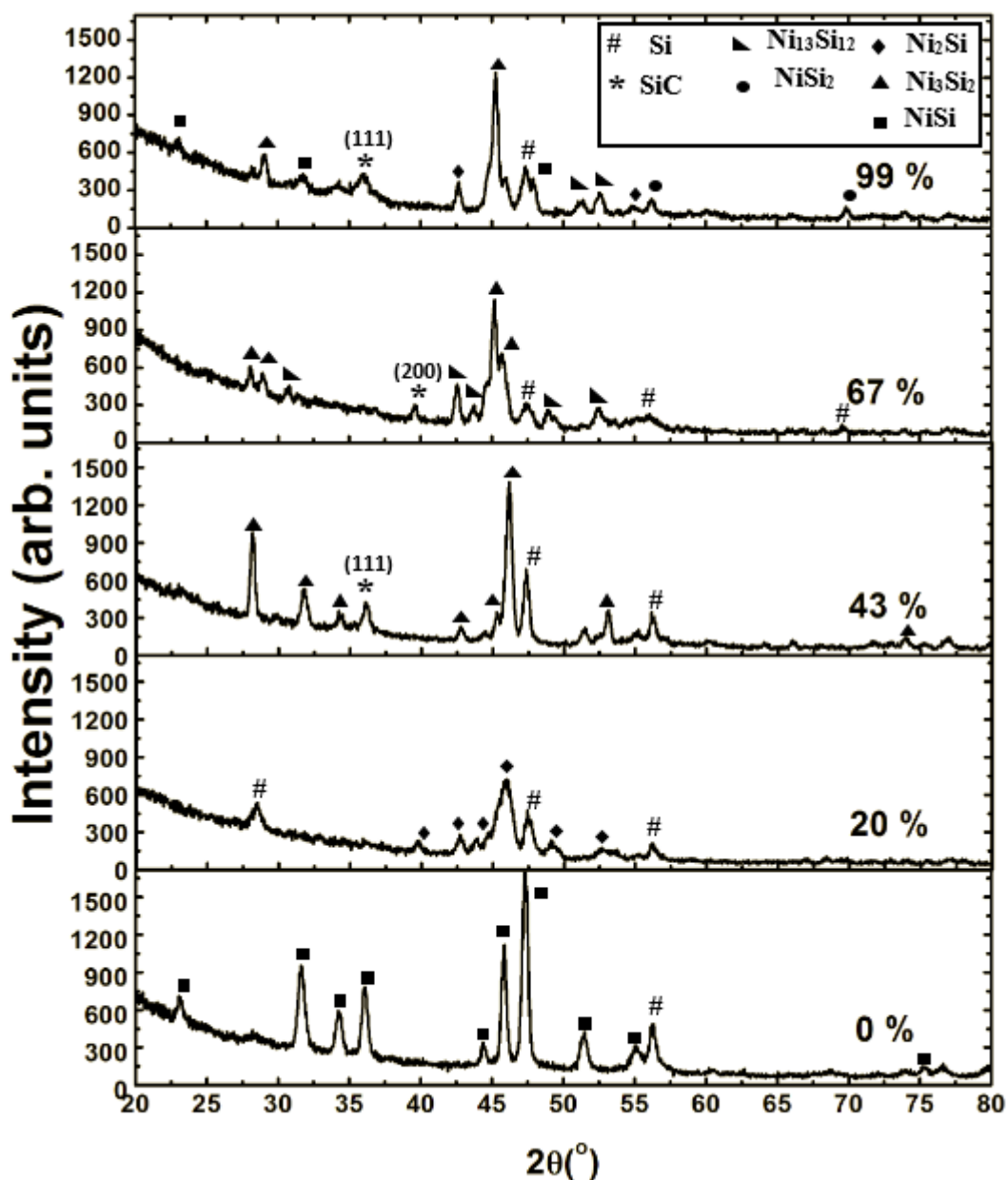


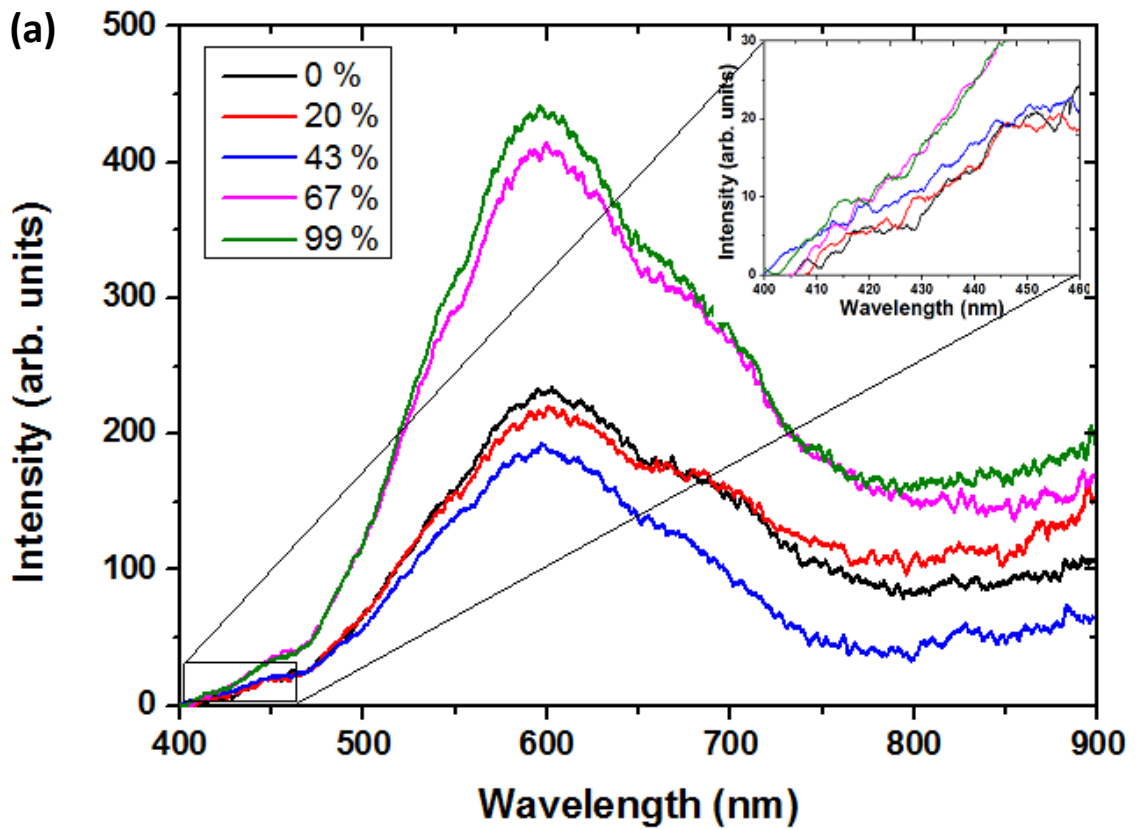
Figure 4.6: XRD patterns of NiSi/SiC core-shell nanowires prepared by HWCVD at different hydrogen dilutions.

4.5 PL Analysis

Figure 4.7 (a) illustrates the PL emission spectra as a function of wavelength for these nanowires grown by HWCVD at different hydrogen dilutions. These nanowires appeared broadened spectrum from 400 to 900 nm of the wavelength, which covered the whole visible part and near infrared region. The PL spectrum with Gaussian decomposition components is shown in figure 4.8 (b). This decomposed PL emission

spectrum consists of five components including three strong emission bands centered at around 537, 600 and 678 nm and two small emission bands located at around 450 and 818 nm. The appearance of two emission bands at 450 and 537 nm which corresponds to blue and green colour of visible light, respectively, indicated the emission of SiC nanostructures (Attolini et al, 2010; Xi et al, 2005; Wang et al, 2012). The green band of emission spectra (2.31 eV) appeared due to the presence of defect centres within the band gap of SiC shell (Gundiah et al, 2002) which is slightly higher than that the bulk 3C-SiC (2.3 eV) due to the weak quantum confinement effect in SiC nanostructure with high intensity coming from recombination process and reduction of dangling bond number formed at the interface boundary with SiO₂ (Xia et al, 2014). While the low intensity of the blue bands (2.76 eV) of 450 wavelength appeared due to decreasing SiO₂ around the SiC shell (Li et al, 2014). However, these emission peaks were appearance with red-shift of the wavelength as compared to the reported workers above due to the quantum size effects of these SiC nanostructure embedded within amorphous matrix. The appearance around small emission bands at 415 and 445 nm indicated the emission of SiC nanostructures (Xi et al, 2005; Wang et al, 2008) which were observed the red-shifted above 43 % in an inset figure. Since the transport bands of these SiC nanostructure are higher than the band of the bulk of SiC (Sohrabi et al, 2013) to exhibit any quantum confinement effect, therefore this PL emission could be referred the presence of the SiC nanostructure within the amorphous matrix. This agreement with the broadening peak appeared in Raman spectrum above 43 %. The peak at around 678 nm which is the red colour of visible light corresponds to the quantum confinement effect of the nanocrystallite Si embedded within amorphous matrix (Chen et al, 2005). The appearance of the peak at 600 nm, which is the orange colour, among the emission band in the range of 550-650 nm and blue shift with high intensity, indicated to the oxygen related defects and/or to surface and interface effect (Inokuma et al, 1998; Chen et al, 2005). The

formation of nano-crystallite Si at the nc-Si/SiO₂ interface created an intermediate state for electron-hole radiative recombination leading to a strong emission in visible region. A small peak at 818 nm, which corresponds to infrared region, observed due to the state transitions into amorphous Si nanoclusters (Goh & Abdurahman, 2014). Thus, the emission band 450-550 nm indicates that the evidence for the quantum confinement of 3C-SiC nano-crystallites (Wu et al, 2005). While the band ranged of 650-800 nm shows the quantum confinement for Si nano-crystilline (De et al, 2010).



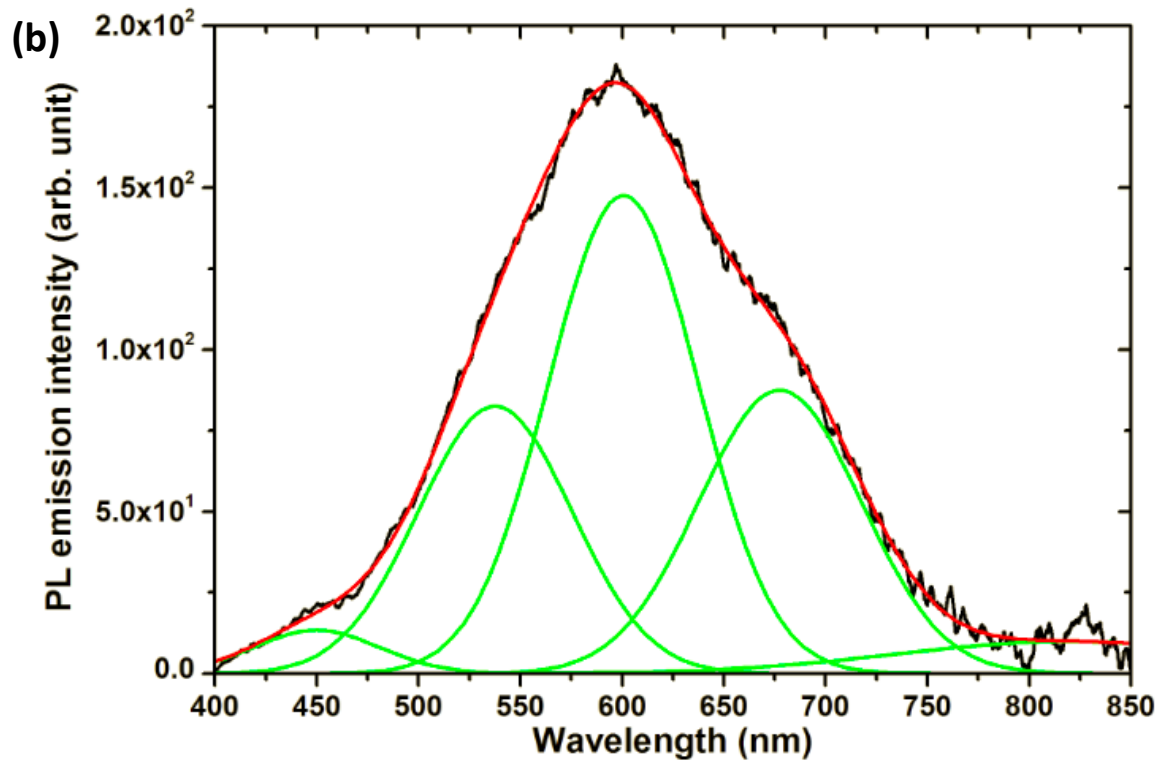


Figure 4.7: (a) PL spectra of NiSi/SiC core-shell nanowires in different hydrogen dilutions. (b) a typical Gaussian de-convolution plot of the peak into different emission bands.

4.6 UV/VIS/NIR Optical Reflectance Analysis

Figure 4.8 shows the optical reflectance spectra of the nanowires deposited on Si substrate at different hydrogen dilutions. It is worth noting that the reflectance of the nanowires shows extremely low in visible and near infrared region from 400 to 900 nm of wavelength. This reveals that the nanowires exhibited superior antireflection characteristic indicating excellent optical absorption properties. The high density of the Si-based nanowires generally exhibited strong antireflection characteristic in the visible region as reported previously (Qin et al, 2011). This antireflection behaviour can be ascribed to the light-trapping effect caused by the construction of the nanostructures, leading to the incident light being reflected and refracted in multiple nanowire arrays and eventually being effectively absorbed (Liu et al, 2012). Furthermore, a large surface area of the nanowires enhances the optical re-absorption ability as reported (Lee et al, 2013; Adachi et al, 2013). The anti-reflection and high absorption properties in the visible

region make the nanowires suitable for photovoltaic applications (Qin et al, 2011; Peng & Lee, 2011). Moreover, the absorption of these heterostructures core-shell nanowires covered the whole of the visible and partly near-infrared regions up to 2, 200 nm. There is an sudden increase in reflection with increase in wavelength above 1, 100 nm for the samples prepared at 43 and 67 % of hydrogen dilutions which could be attributed to the alignment of the nanowires as illustrated in figure 1. Slanting and less dense of the grown nanowires could lead to scattering of lights on the nanowire surfaces thus reduces the light-trapping effect. For the sample prepared at 99 % hydrogen dilution, film-like structure usually has high reflection as compared to due to the nanostructures especially one-dimensional nanowires. Obviously, nanowire morphologies play an important role in controlling the antireflection properties of the samples. The appearance of broad peaks near to 450 nm for the samples prepared at 67 % could be related to the optical inter-band of the NiSi grains which contributed to the surface roughness of the nanostructures. Thus, these nanowires suppress light reflection over wide spectral bandwidth which makes them to be used without any antireflection coatings. That is useful for optoelectronic applications.

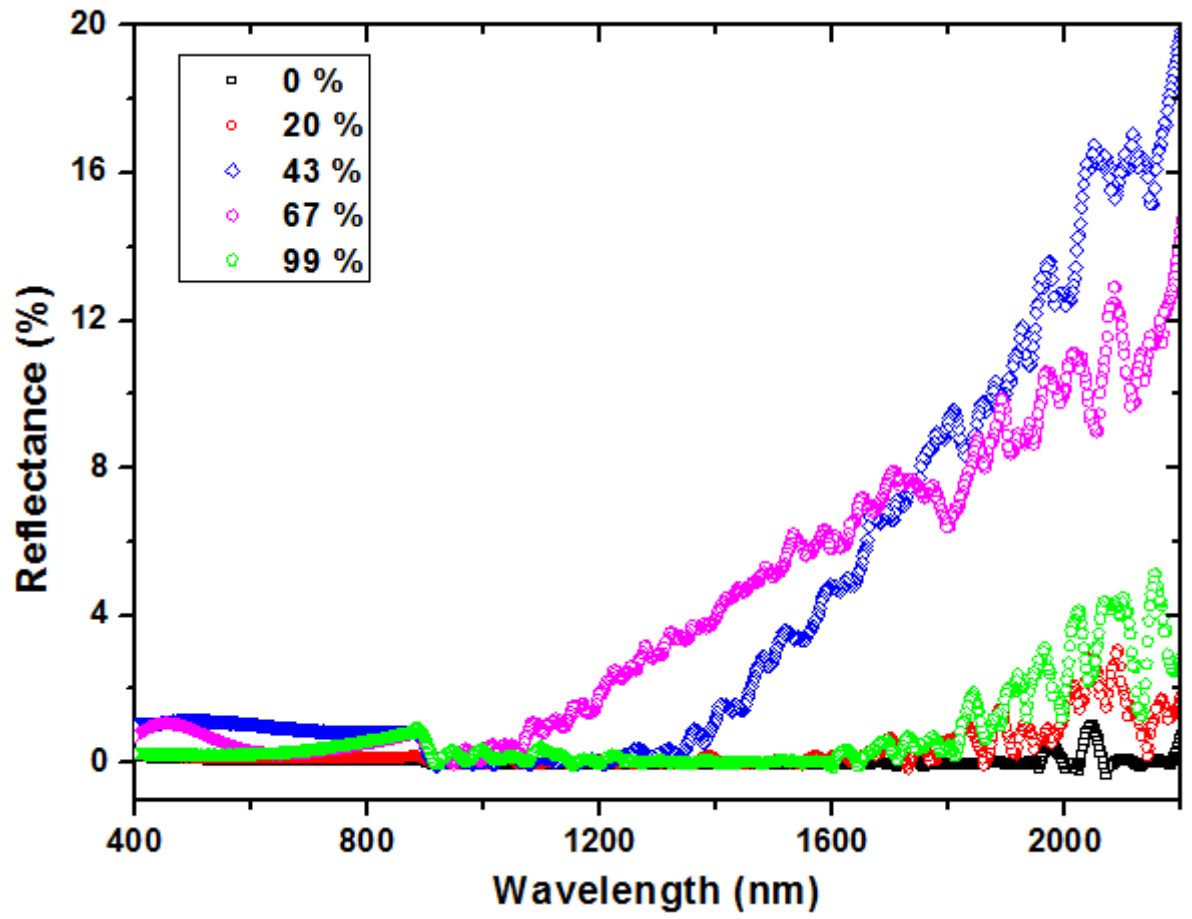


Figure 4.8: optical reflectance spectra of NiSi/SiC core-shell nanowires at different hydrogen dilutions.

CHAPTER 5

CONCLUSIONS

5.1 Conclusions

The morphological, structural and optical properties of NiSi/SiC core-shell nanowires prepared by HWCVD at different hydrogen dilutions were studied. The nanowires were grown in high density and high reflectance of the light without hydrogen dilution. The nanowires consist of single crystalline NiSi and amorphous SiC as core and shell of the nanowires, respectively. Introducing of hydrogen dilution up to 43 % enhanced the growth of the nanowires. The hydrogen effect plays an important role for transition of the phases and increasing in the decomposition rate. Moreover, an increase of the hydrogen dilution is attributed to enhancement of deposition of SiC shell. That leads to phase transition from the crystallite Si phase to amorphous SiC phase. This shell of the nanowires showed presence of 3C-SiC nano-crystallites embedded within an amorphous matrix. The increasing of hydrogen dilution to 99 % in the deposition growth, a film started to emerge due to the increasing of hydrogen compression on the nanowires. The NiSi/SiC core-shell nanowires embedded within an amorphous matrix exhibited various room-temperature PL emissions in the range of 400 – 900 nm. These nanowires appeared low reflectance which is useful for optoelectronic applications.

REFERENCES

- Adachi, M. M., Anantram, M. P., & Karim, K. S. (2013). Core-shell silicon nanowire solar cells. *Scientific reports*, 3.
- Adhikari, K., & Ray, A. K. (2011). On the existence and stability of double-walled armchair silicon carbide nanotubes. *Solid State Communications*, 151(6), 430-435.
- Aharonovich, I., Tamir, S., & Lifshitz, Y. (2008). Growth of SiO_x nanowires by laser ablation. *Nanotechnology*, 19(6), 065608.
- Alvi, N. H., Usman Ali, S. M., Hussain, S., Nur, O., & Willander, M. (2011). Fabrication and comparative optical characterization of n-ZnO nanostructures (nanowalls, nanorods, nanoflowers and nanotubes)/p-GaN white-light-emitting diodes. *Scripta Materialia*, 64(8), 697-700.
- Attolini, G., Rossi, F., Bosi, M., Watts, B. E., & Salviati, G. (2008). Synthesis and characterization of 3C-SiC nanowires. *Journal of Non-Crystalline Solids*, 354(47), 5227-5229.
- Attolini, G., Rossi, F., Fabbri, F., Bosi, M., Salviati, G., & Watts, B. E. (2010). Cubic SiC Nanowires: Growth, Characterization and Applications.
- Attolini, G., Rossi, F., Fabbri, F., Bosi, M., Watts, B. E., & Salviati, G. (2009). A new growth method for the synthesis of 3C-SiC nanowires. *Materials Letters*, 63(29), 2581-2583.
- Bhaskaran, M., Sriram, S., Perova, T. S., Ermakov, V., Thorogood, G. J., Short, K. T., & Holland, A. S. (2009). *In situ* micro-Raman analysis and X-ray diffraction of nickel silicide thin films on silicon. *Micron*, 40(1), 89-93.
- Bi, L., & Feng, J. Y. (2006). Nanocrystal and interface defects related photoluminescence in silicon-rich Al₂O₃ films. *Journal of luminescence*, 121(1), 95-101.
- Campos, L. C., Tonezzer, M., Ferlauto, A. S., Grillo, V., Magalhães-Paniago, R., Oliveira, S. & Lacerda, R. G. (2008). Vapor-Solid-Solid Growth Mechanism Driven by Epitaxial Match between Solid AuZn Alloy Catalyst Particles and ZnO Nanowires at Low Temperatures. *Advanced Materials*, 20(8), 1499-1504.
- Cao, L., Liu, X., Zhao, J., & Lu, H. (2012). Synthesis and photoluminescence of the branching silicon carbide nanowires. *Physica E: Low-dimensional Systems and Nanostructures*, 46, 57-60.
- Cao, Y., Wu, Z., Ni, J., Bhutto, W. A., Li, J., Li, S. & Kang, J. (2012). Type-II Core/Shell Nanowire Heterostructures and Their Photovoltaic Applications. *Nano-Micro Letters*, 4(3).
- Chang, W. Growth of 3C-Silicon Carbide Nanowires using Chemical Vapor Deposition. 2008.
- Chehata, N., Ltaief, A., Ilahi, B., Salam, B., Bouazizi, A., Maaref, H., & Beyou, E. (2014). Improved photovoltaic performance of silicon nanowires/conjugated polymer hybrid solar cells. *Synthetic Metals*, 191, 6-11.

- Chen, K., Huang, Z., Huang, J., Fang, M., Liu, Y. G., Ji, H., & Yin, L. (2013). Synthesis of SiC nanowires by thermal evaporation method without catalyst assistant. *Ceramics International*, 39(2), 1957-1962.
- Chen, X. Y., Lu, Y. F., Tang, L. J., Wu, Y. H., Cho, B. J., Xu, X. J., ... & Song, W. D. (2005). Annealing and oxidation of silicon oxide films prepared by plasma-enhanced chemical vapor deposition. *Journal of applied physics*, 97(1), 014913.
- Chen, Y., Zhang, X., Zhao, Q., He, L., Huang, C., & Xie, Z. (2011). P-type 3C-SiC nanowires and their optical and electrical transport properties. *Chem. Commun.*, 47(22), 6398-6400.
- Chong, S. K., Goh, B. T., Aspanut, Z., Muhamad, M. R., Dee, C. F., & Rahman, S. A. (2011). Effect of rf power on the growth of silicon nanowires by hot-wire assisted plasma enhanced chemical vapor deposition (HW-PECVD) technique. *Thin Solid Films*, 519(15), 4933-4939.
- Chong, S. K., Goh, B. T., Aspanut, Z., Muhamad, M. R., Dee, C. F., & Rahman, S. A. (2011). Effect of substrate temperature on gold-catalyzed silicon nanostructures growth by hot-wire chemical vapor deposition (HWCVD). *Applied Surface Science*, 257(8), 3320-3324.
- Chong, S. K., Goh, B. T., Dee, C. F., & Rahman, S. A. (2012). Study on the role of filament temperature on growth of indium-catalyzed silicon nanowires by the hot-wire chemical vapor deposition technique. *Materials Chemistry and Physics*, 135(2), 635-643.
- Chong, S. K., Goh, B. T., Dee, C. F., & Rahman, S. A. (2013). Effect of substrate to filament distance on formation and photoluminescence properties of indium catalyzed silicon nanowires using hot-wire chemical vapor deposition. *Thin Solid Films*, 529, 153-158.
- Chong, S. K., Goh, B. T., Wong, Y. Y., Nguyen, H. Q., Do, H., Ahmad, I., ... & Rahman, S. A. (2012). Structural and photoluminescence investigation on the hot-wire assisted plasma enhanced chemical vapor deposition growth silicon nanowires. *Journal of Luminescence*, 132(6), 1345-1352.
- Cui, H., Gong, L., Sun, Y., Yang, G. Z., Liang, C. L., Chen, J., & Wang, C. X. (2011). Direct synthesis of novel SiC@ Al₂O₃ core-shell epitaxial nanowires and field emission characteristics. *CrystEngComm*, 13(5), 1416-1421.
- Dayeh, S, A; Yu, E ,T; Wang, D,I.III-V nanowires growth mechanism : V/III ratio and temperature effects. *Nano Lett.*2007,7,2486.
- De Boer, W. D. A. M., Timmerman, D., Dohnalova, K., Yassievich, I. N., Zhang, H., Buma, W. J., & Gregorkiewicz, T. (2010). Red spectral shift and enhanced quantum efficiency in phonon-free photoluminescence from silicon nanocrystals. *Nature nanotechnology*, 5(12), 878-884.
- Deb, S. K., Wilding, M., Somayazulu, M., & McMillan, P. F. (2001). Pressure-induced amorphization and an amorphous–amorphous transition in densified porous silicon. *Nature*, 414(6863), 528-530.
- Decker, C. A., Solanki, R., Freeouf, J. L., Carruthers, J. R., & Evans, D. R. (2004). Directed growth of nickel silicide nanowires. *Applied physics letters*,84(8), 1389-1391.

- Dolgiy, A. L., Redko, S. V., Komissarov, I., Bondarenko, V. P., Yanushkevich, K. I., & Prischepa, S. L. (2013). Structural and magnetic properties of Ni nanowires grown in mesoporous silicon templates. *Thin Solid Films*, 543, 133-137.
- Fan, X., Zhang, H., Du, N., & Yang, D. (2012). Phase-controlled synthesis of nickel silicide nanostructures. *Materials Research Bulletin*, 47(11), 3797-3803.
- Feng, Z. C., Mascarenhas, A. J., Choyke, W. J., & Powell, J. A. (1988). Raman scattering studies of chemical-vapor-deposited cubic SiC films of (100) Si. *Journal of applied physics*, 64(6), 3176-3186.
- Gao, L., Zhong, H., & Chen, Q. (2013). Synthesis of 3C-SiC nanowires by reaction of poly (ethylene terephthalate) waste with SiO₂ microspheres. *Journal of Alloys and Compounds*, 566, 212-216.
- Gao, Y., Bao, W., Meng, Q., Jing, Y., & Song, X. (2014). The thermal transport properties of single-crystalline nanowires covered with amorphous shell: A molecular dynamics study. *Journal of Non-Crystalline Solids*, 387, 132-138.
- Goh, B. T., & Rahman, S. A. (2014). Study of the growth, and effects of filament to substrate distance on the structural and optical properties of Si/SiC core-shell nanowires synthesized by hot-wire chemical vapor deposition. *Materials Chemistry and Physics*, 147(3), 974-981.
- Goh, B. T., & Rahman, S. A. (2014). Synthesis of nickel catalyzed Si/SiC core-shell nanowires by HWCVD. *Journal of Crystal Growth*, 407, 25-30.
- Grinberg, O. Y., & Berliner, L. J. (Eds.). (2004). *Very High Frequency (VHF) ESR/EPR (Vol. 22)*. Springer.
- Gundiah, G., Madhav, G. V., Govindaraj, A., Seikh, M. M., & Rao, C. N. R. (2002). Synthesis and characterization of silicon carbide, silicon oxynitride and silicon nitride nanowires. *Journal of Materials Chemistry*, 12(5), 1606-1611.
- Hannon, J. B., Kodambaka, S., Ross, F. M., & Tromp, R. M. (2006). The influence of the surface migration of gold on the growth of silicon nanowires. *Nature*, 440(7080), 69-71.
- Hsu, Y. J., & Lu, S. Y. (2005). Vapor-solid growth of Sn nanowires: Growth mechanism and superconductivity. *The Journal of Physical Chemistry B*, 109(10), 4398-4403.
- Huong, N. T., Van, N. D., Tien, D. M., Tung, D. K., Binh, N. T., Anh, T. K., & Minh, L. Q. (2011). Structural and luminescent properties of (Eu, Tb) PO₄·H₂O nanorods/nanowires prepared by microwave technique. *Journal of rare earths*, 29(12), 1170-1173
- Hwang, Y. J., Boukai, A., & Yang, P. (2008). High density n-Si/n-TiO₂ core/shell nanowire arrays with enhanced photoactivity. *Nano letters*, 9(1), 410-415.
- Ibupoto, Z. H., Khun, K., Liu, X., & Willander, M. (2013). Low temperature synthesis of seed mediated CuO bundle of nanowires, their structural characterisation and cholesterol detection. *Materials Science and Engineering: C*, 33(7), 3889-3898.
- Inokuma, T., Wakayama, Y., Muramoto, T., Aoki, R., Kurata, Y., & Hasegawa, S. (1998). Optical properties of Si clusters and Si nanocrystallites in high-temperature annealed SiO_x films. *Journal of applied physics*, 83(4), 2228-2234.

- Iwai, H., Ohguro, T., & Ohmi, S. I. (2002). NiSi silicide technology for scaled CMOS. *Microelectronic Engineering*, 60(1), 157-169.
- Jalilian, R. (2008). *Pulse Laser Assisted Growth of Nanowires and Nano-heterojunctions and Their Properties*. ProQuest.
- Jasinevicius, R. G., Duduch, J. G., & Pizani, P. S. (2007). In-situ raman spectroscopy analysis of re-crystallization annealing of diamond turned silicon crystal. *Journal of the Brazilian Society of Mechanical Sciences and Engineering*, 29(1), 49-54.
- Jessica L. Lensch-Falk, Eric R. Hemesath, Daniel E. Pere, Lincoln J. Lauhon J. Mater. Chem., 19 (2009), p. 849
- Kelzenberg, M. D., Turner-Evans, D. B., Kayes, B. M., Filler, M. A., Putnam, M. C., Lewis, N. S., & Atwater, H. A. (2008). Photovoltaic measurements in single-nanowire silicon solar cells. *Nano letters*, 8(2), 710-714.
- Khan, A. (2014). Position Dependent Growth of Polycrystalline Cubic-SiC Film in a Cold-Wall Atmospheric Pressure Chemical Vapour Deposition Reactor. *Science of Advanced Materials*, 6(6), 1286-1292.
- Kim, C. J., Kang, K., Woo, Y. S., Ryu, K. G., Moon, H., Kim, J. M., ... & Jo, M. H. (2007). Spontaneous chemical vapor growth of NiSi nanowires and their metallic properties. *Advanced Materials*, 19(21), 3637-3642.
- Kim, G. B., Yoo, D. J., Baik, H. K., Myoung, J. M., Lee, S. M., Oh, S. H., & Park, C. G. (2003). Improved thermal stability of Ni silicide on Si (100) through reactive deposition of Ni. *Journal of Vacuum Science & Technology B*, 21(1), 319-322.
- Kim, J., & Anderson, W. A. (2005). Spontaneous nickel monosilicide nanowire formation by metal induced growth. *Thin Solid Films*, 483(1), 60-65.
- Kim, J., Shin, Y. H., Yun, J. H., Han, C. S., Hyun, M. S., & Anderson, W. A. (2008). A nickel silicide nanowire microscopy tip obtains nanoscale information. *Nanotechnology*, 19(48), 485713.
- Kuo, C. Y., & Gau, C. (2011). Vapor–solid–solid growth of crystalline silicon nanowires using anodic aluminum oxide template. *Thin solid films*, 519(11), 3603-3607.
- Kuykendall, T., Pauzauskie, P., Lee, S., Zhang, Y., Goldberger, J., & Yang, P. (2003). Metalorganic chemical vapor deposition route to GaN nanowires with triangular cross sections. *Nano Letters*, 3(8), 1063-1066.
- LaLonde, A. D., Norton, M. G., McIlroy, D. N., Zhang, D., Padmanabhan, R., Alkhateeb, A. & Holman, Z. (2005). Metal coatings on SiC nanowires by plasma-enhanced chemical vapor deposition. *Journal of materials research*, 20(3), 549-553.
- Lavoie, C.; d'Heurle, F. M, Detavernier, C, & Cabral Jr. C, (2003). Towards implementation of a nickel silicide process for CMOS Technologies. *Microelectronic Engineering*, 70, 144-157.
- Lee, J. B., Jeong, S. Y., Park, B. J., Choi, C. J., Hong, K., Whang, S. J., & Seong, T. Y. (2010). Improved electrical and thermal properties of nickel silicides by using a NiCo interlayer. *Superlattices and Microstructures*, 47(2), 259-265
- Lee, K. S., Mo, Y. H., Nahm, K. S., Shim, H. W., Suh, E. K., Kim, J. R., & Kim, J. J. (2004). Anomalous growth and characterization of carbon-coated nickel silicide nanowires. *Chemical physics letters*, 384(4), 215-218.

- Lee, Y. H., Fu, L., Li, Z., Breuer, S., Tan, H., Jagadish, C., & Parkinson, P. (2013). Nanowire solar cells for next-generation photovoltaics. In Proc. SPIE(Vol. 10, No. 2.1201308, p. 005048).
- Li, J., Wang, D., & LaPierre, R. R. (Eds.). (2011). *Advances in III-V Semiconductor Nanowires and Nanodevices*. Bentham Science Publishers.
- Li, X., Chen, X., & Song, H. (2011). Preparation of silicon carbide nanowires via a rapid heating process. *Materials Science and Engineering: B*, 176(1), 87-91.
- Li, Z., Zhao, J., Zhang, M., Xia, J., & Meng, A. (2014). SiC nanowires with thickness-controlled SiO₂ shells: Fabrication, mechanism, reaction kinetics and photoluminescence properties. *Nano Research*, 7(4), 1-11.
- Lisowski, M., & Zipper, E. (1998). Orbital magnetic ordering in disordered mesoscopic systems. *Journal of magnetism and magnetic materials*, 189(2), 225-233.
- Liu, C. Y., Xu, H. Y., Ma, J. G., Li, X. H., Zhang, X. T., Liu, Y. C., & Mu, R. (2011). Electrically pumped near-ultraviolet lasing from ZnO/MgO core/shell nanowires. *Applied Physics Letters*, 99(6), 063115.
- Liu, Y., Ji, G., Wang, J., Liang, X., Zuo, Z., & Shi, Y. (2012). Fabrication and photocatalytic properties of silicon nanowires by metal-assisted chemical etching: effect of H₂O₂ concentration. *Nanoscale research letters*, 7(1), 1-9.
- Longo, M., Fallica, R., Wiemer, C., Salicio, O., Fanciulli, M., Rotunno, E., & Lazzarini, L. (2012). Metal Organic Chemical Vapor Deposition of Phase Change Ge₁Sb₂Te₄ Nanowires. *Nano letters*, 12(3), 1509-1515.
- Lund, I. N., Lee, J. H., Efstathiadis, H., Haldar, P., & Geer, R. E. (2014). Influence of catalyst layer thickness on the growth of nickel silicide nanowires and its application for Li-ion batteries. *Journal of Power Sources*, 246, 117-123.
- Meshram, N., Kumbhar, A., & Dusane, R. O. (2013). Synthesis of silicon nanowires using tin catalyst by hot wire chemical vapor processing. *Materials Research Bulletin*, 48(6), 2254-2258.
- Meyyappan, M., & Sunkara, M. K. (2009). *Inorganic nanowires: applications, properties, and characterization*. CRC Press.
- Mézy, A., Anceau, S., Bretagnon, T., Lefebvre, P., Taliercio, T., Yi, G. C., & Yoo, J. (2006). Optical properties of ZnO nanorods and nanowires. *Superlattices and Microstructures*, 39(1), 358-365.
- Minaee, H., Mousavi, S. H., Haratizadeh, H., & de Oliveira, P. W. (2013). Oxygen sensing properties of zinc oxide nanowires, nanorods, and nanoflowers: The effect of morphology and temperature. *Thin Solid Films*, 545, 8-12.
- Mohiddon, M. A., & Krishna, M. G. (2011). Nanocrystalline wurtzite Si–nickel silicide composite thin films with large band gap and high resistivity. *Journal of Materials Science*, 46(8), 2672-2677.
- Morales, A. M., & Lieber, C. M. (1998). A laser ablation method for the synthesis of crystalline semiconductor nanowires. *Science*, 279(5348), 208-211.
- Nazarudin, N. F. F. B., Azizan, S. N. A. B., Rahman, S. A., & Goh, B. T. (2014). Growth and structural property studies on NiSi/SiC core-shell nanowires by hot-wire chemical vapor deposition. *Thin Solid Films*.

- Nazarudin, N. F. F. B., Noor, N. J. B. M., Rahman, S. A., & Goh, B. T. (2015). Photoluminescence and structural properties of Si/SiC core-shell nanowires growth by HWCVD. *Journal of Luminescence*, 157, 149-157.
- Niu, J., Sha, J., & Yang, D. (2004). Silicon nanowires fabricated by thermal evaporation of silicon monoxide. *Physica E: Low-dimensional Systems and Nanostructures*, 23(1), 131-134.
- Noor, M. O., & Krull, U. J. (2014). Silicon nanowires as field-effect transducers for biosensor development: A review. *Analytica Chimica Acta*, 825, 1-25.
- Ostrikov, K. K., Seo, D. H., Mehdipour, H., Cheng, Q., & Kumar, S. (2012). Plasma effects in semiconducting nanowire growth. *Nanoscale*, 4(5), 1497-1508.
- Pant, A., Russell, T. W. F., Huff, M. C., Aparicio, R., & Birkmire, R. W. (2001). Hot-wire chemical vapor deposition of silicon from silane: Effect of process conditions. *Industrial & engineering chemistry research*, 40(5), 1377-1385.
- Pauzauskie, P. J., & Yang, P. (2006). Nanowire photonics. *Materials Today*, 9(10), 36-45.
- Peng, K. Q., & Lee, S. T. (2011). Silicon nanowires for photovoltaic solar energy conversion. *Advanced Materials*, 23(2), 198-215.
- Qin, Y., Li, F., Liu, D., Yan, H., Wang, J., & He, D. (2011). The structure and optical properties of silicon nanowires prepared by inductively coupled plasma chemical vapor deposition. *Materials Letters*, 65(7), 1117-1119.
- Rath, J. K. (2003). Low temperature polycrystalline silicon: a review on deposition, physical properties and solar cell applications. *Solar Energy Materials and Solar Cells*, 76(4), 431-487.
- Rousskikh, A. G., Baksht, R. B., Chaikovskiy, S. A., Fedunin, A. V., Khishchenko, K. V., Labetsky, A. Y., ... & Tkachenko, S. I. (2006). The effects of preheating of a fine tungsten wire and the polarity of a high-voltage electrode on the energy characteristics of an electrically exploded wire in vacuum. *Plasma Science, IEEE Transactions on*, 34(5), 2232-2238.
- Sankir, N. D., & Dogan, B. (2011). Growth of CdS thin films and nanowires for flexible photoelectrochemical cells. *Journal of Materials Processing Technology*, 211(3), 382-387.
- Schmidt, V., Wittemann, J. V., & Gosele, U. (2010). Growth, thermodynamics, and electrical properties of silicon nanowires†. *Chemical reviews*, 110(1), 361-388.
- Şenozan, S., Turgut, S., & Tomak, M. (2011). A continuum model for dephasing in mesoscopic systems. *Physica E: Low-dimensional Systems and Nanostructures*, 43(10), 1845-1852.
- Shahid, M., Liu, J., Ali, Z., Shakir, I., & Warsi, M. F. (2013). Structural and electrochemical properties of single crystalline MoV₂O₈ nanowires for energy storage devices. *Journal of Power Sources*, 230, 277-281.
- Sirleto, L., Ferrara, M. A., Nikitin, T., Novikov, S., & Khriachtchev, L. (2012). Giant Raman gain in silicon nanocrystals. *Nature communications*, 3, 1220.
- Sohrabi, F., Nikniazi, A., & Movla, H. (2013). Optimization of Third Generation Nanostructured Silicon-Based Solar Cells.

- Sze, S. M., & Ng, K. K. (2006). Metal-semiconductor contacts. *Physics of semiconductor devices*, 134-196.
- Tanaka, S., Kitagawa, H., & Ikari, T. (2001). Precipitation-enhanced diffusion of nickel in dislocation-free silicon studied by in-diffusion and annealing processes. *Physica B: Condensed Matter*, 308, 427-430
- Tang, J., Huo, Z., Brittan, S., Gao, H., & Yang, P. (2011). Solution-processed core-shell nanowires for efficient photovoltaic cells. *Nature nanotechnology*, 6(9), 568-572.
- Thambidurai, M., Muthukumarasamy, N., Velauthapillai, D., & Lee, C. (2014). Rosa centifolia sensitized ZnO nanorods for photoelectrochemical solar cell applications. *Solar Energy*.
- Tsakalakos, L., Balch, J., Fronheiser, J., Korevaar, B. A., Sulima, O., & Rand, J. (2007). Silicon nanowire solar cells. *Applied Physics Letters*, 91(23), 233117.
- Vj, L., Oh, J., Nayak, A. P., Katzenmeyer, A. M., Gilchrist, K. H., Grego, S., ... & Islam, M. S. (2011). A perspective on nanowire photodetectors: Current status, future challenges, and opportunities. *Selected Topics in Quantum Electronics, IEEE Journal of*, 17(4), 1002-1032.
- Wang, D. H., Xu, D., Wang, Q., Hao, Y. J., Jin, G. Q., Guo, X. Y., & Tu, K. N. (2008). Periodically twinned SiC nanowires. *Nanotechnology*, 19(21), 215602.
- Wang, J., Liu, S., Ding, T., Huang, S., & Qian, C. (2012). Synthesis, characterization, and photoluminescence properties of bulk-quantity β -SiC/SiO_x coaxial nanowires. *Materials Chemistry and Physics*, 135(2), 1005-1011.
- Wang, K., Rai, S. C., Marmon, J., Chen, J., Yao, K., Wozny, S., ... & Zhou, W. (2014). Nearly Lattice Matched All Wurtzite CdSe/ZnTe Type II Core-Shell Nanowires with Epitaxial Interfaces for Photovoltaics. *Nanoscale*.
- Wu, T., Shen, H., Cheng, B., Pan, Y., Liu, B., & Shen, J. (2011). Formation of α -Si_{1-x}C_x: H and nc-SiC films grown by HWCVD under different process pressure. *Applied Surface Science*, 258(3), 999-1003.
- Wu, X. L., Fan, J. Y., Qiu, T., Yang, X., Siu, G. G., & Chu, P. K. (2005). Experimental evidence for the quantum confinement effect in 3 C-SiC nanocrystallites. *Physical review letters*, 94(2), 026102.
- Wu, Y., Xiang, J., Yang, C., Lu, W., & Lieber, C. M. (2004). Single-crystal metallic nanowires and metal/semiconductor nanowire heterostructures. *Nature*, 430(6995), 61-65.
- Xi, G., Yu, S., Zhang, R., Zhang, M., Ma, D., & Qian, Y. (2005). Crystalline silicon carbide nanoparticles encapsulated in branched wavelike carbon nanotubes: synthesis and optical properties. *The Journal of Physical Chemistry B*, 109(27), 13200-13204.
- Xi, G., Yu, S., Zhang, R., Zhang, M., Ma, D., & Qian, Y. (2005). Crystalline silicon carbide nanoparticles encapsulated in branched wavelike carbon nanotubes: synthesis and optical properties. *The Journal of Physical Chemistry B*, 109(27), 13200-13204.

- Xia Liua, Lianzhen Caoa, Hang Song, Hong Jiang (2014). Strong ultraviolet and green photoluminescence from SiC/SiO₂ core-shell nanowires. *Physica E*, (61)167–170.
- Xing, Y. J., Hang, Q. L., Yan, H. F., Pan, H. Y., Xu, J., Yu, D. P., ... & Feng, S. Q. (2001). Solid-liquid-solid (SLS) growth of coaxial nanocables: silicon carbide sheathed with silicon oxide. *Chemical physics letters*, 345(1), 29-32.
- Yan, H. F., Xing, Y. J., Hang, Q. L., Yu, D. P., Wang, Y. P., Xu, J., ... & Feng, S. Q. (2000). Growth of amorphous silicon nanowires via a solid-liquid-solid mechanism. *Chemical Physics Letters*, 323(3), 224-228.
- Yang, P. (2005). The chemistry and physics of semiconductor nanowires. *MRS bulletin*, 30(02), 85-91.
- Yang, P. (2012). Semiconductor nanowire building blocks: From flux line pinning to artificial photosynthesis. *MRS bulletin*, 37(09), 806-813.
- Yin, X., Que, W., Fei, D., Xie, H., & He, Z. (2013). Effect of TiO₂ shell layer prepared by wet-chemical method on the photovoltaic performance of ZnO nanowires arrays-based quantum dot sensitized solar cells. *Electrochimica Acta*, 99, 204-210.
- Yu, D. P., Xing, Y. J., Hang, Q. L., Yan, H. F., Xu, J., Xi, Z. H., & Feng, S. Q. (2001). Controlled growth of oriented amorphous silicon nanowires via a solid-liquid-solid (SLS) mechanism. *Physica E: Low-dimensional Systems and Nanostructures*, 9(2), 305-309.
- Zekentes, K., & Rogdakis, K. (2011). SiC nanowires: material and devices. *Journal of Physics D: Applied Physics*, 44(13), 133001.
- Zhai, X., Tan, R., Wang, W., Huang, J., Zhuang, F., Dai, S., & Song, W. (2014). Silicon-Hydrogen bond Effects on aluminum-induced crystallization of hydrogenated amorphous silicon films. *Journal of Crystal Growth*.
- Zhang, S. L., Zhu, B. F., Huang, F., Yan, Y., Shang, E. Y., Fan, S., & Han, W. (1999). Effect of defects on optical phonon Raman spectra in SiC nanorods. *Solid state communications*, 111(11), 647-651.
- Zhao, F. F., Zheng, J. Z., Shen, Z. X., Osipowicz, T., Gao, W. Z., & Chan, L. H. (2004). Thermal stability study of NiSi and NiSi₂ thin films. *Microelectronic engineering*, 71(1), 104-111.
- Zhu, J., Jia, J., Kwong, F. L., & Ng, D. H. (2013). Synthesis of 6 H-SiC nanowires on bamboo leaves by carbothermal method. *Diamond and Related Materials*, 33, 5-11.
- Zhu, J., Yu, Z., Burkhard, G. F., Hsu, C. M., Connor, S. T., Xu, Y., ... & Cui, Y. (2008). Optical absorption enhancement in amorphous silicon nanowire and nanocone arrays. *Nano letters*, 9(1), 279-282.
- Zhuang, H., Zhang, L., Staedler, T., & Jiang, X. (2012). Nanoscale integration of SiC/SiO₂ core-shell nanocables in diamond through a simultaneous hybrid structure fabrication. *Applied Physics Letters*, 100(19), 193102.

APPENDICES

Appendices A: XRD patterns of materials.

Name and formula

Reference code:	01-089-2955
ICSD name:	Silicon
Empirical formula:	Si
Chemical formula:	Si

Crystallographic parameters

Crystal system:	Cubic
Space group:	Fd-3m
Space group number:	227
a (Å):	5.4303
b (Å):	5.4303
c (Å):	5.4303
Alpha (°):	90.0000
Beta (°):	90.0000
Gamma (°):	90.0000
Calculated density:	2.33
Measured density:	2.33
Volume of cell:	160.13
Z:	8.00
RIR:	4.55

Subfiles and Quality

Subfiles:	Inorganic Alloy, metal or intermetallic Modelled additional pattern
Quality:	Calculated (C)

Comments

ICSD collection code:	043610
Test from ICSD:	No R value given. At least one TF missing.

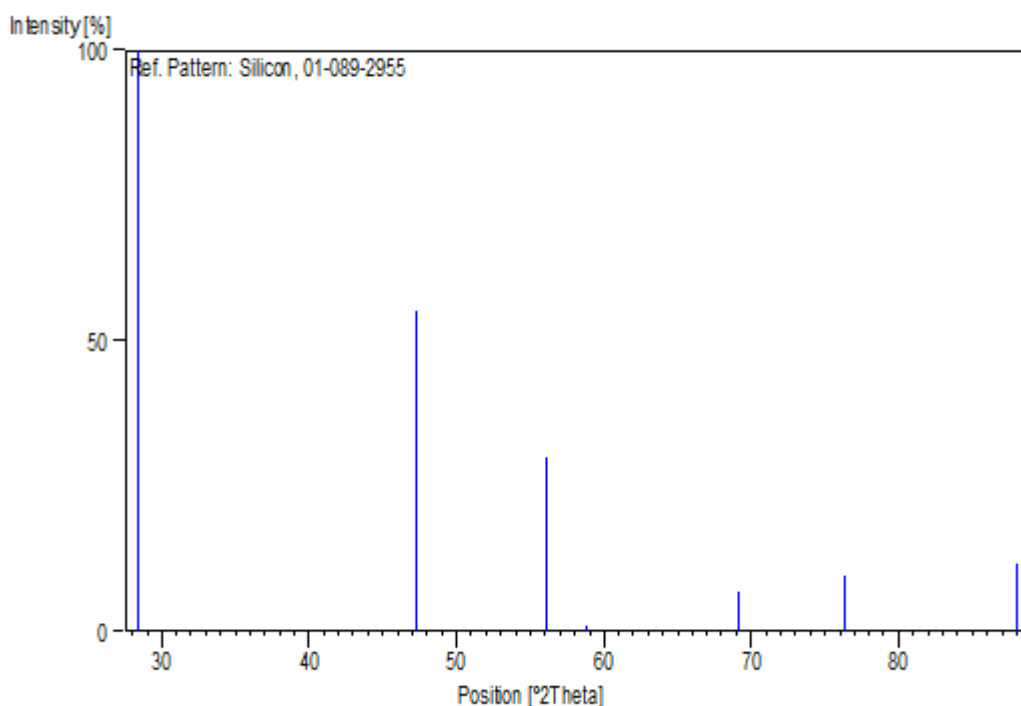
References

Primary reference:	<i>Calculated from ICSD using POWD-12++</i>
Structure:	Straumanis, M.E., Borgeaud, P., James, W.J., <i>J. Appl. Phys.</i> , 32 , 1382, (1961)

Peak list

No.	h	k	l	d [Å]	2Theta [deg]	I [%]
1	1	1	1	3.13518	28.446	100.0
2	2	2	0	1.91990	47.309	55.4
3	3	1	1	1.63729	56.130	30.0
4	2	2	2	1.56759	58.864	0.1
5	4	0	0	1.35757	69.140	6.9
6	3	3	1	1.24579	76.387	9.5
7	4	2	2	1.10845	88.044	11.5

Stick Pattern



Name and formula

Reference code:	00-065-1428
ICSD name:	Nickel Silicon
Empirical formula:	Ni ₃ Si ₂
Chemical formula:	Ni ₃ Si ₂

Crystallographic parameters

Crystal system:	Orthorhombic
Space group:	Cmc21
Space group number:	36
a (Å):	12.2290
b (Å):	10.8050
c (Å):	6.9240
Alpha (°):	90.0000
Beta (°):	90.0000
Gamma (°):	90.0000

Volume of cell: 914.90
Z: 16.00
RIR: 1.79

Subfiles and Quality

Subfiles: Inorganic
Alloy, metal or intermetallic
Modelled additional pattern
Quality: Calculated (C)

Comments

References

Primary reference: *Calculated from NIST using POWD-12++*
Structure: G.Pilström, *Acta Chem. Scand.*, **15**, 893, (1961)

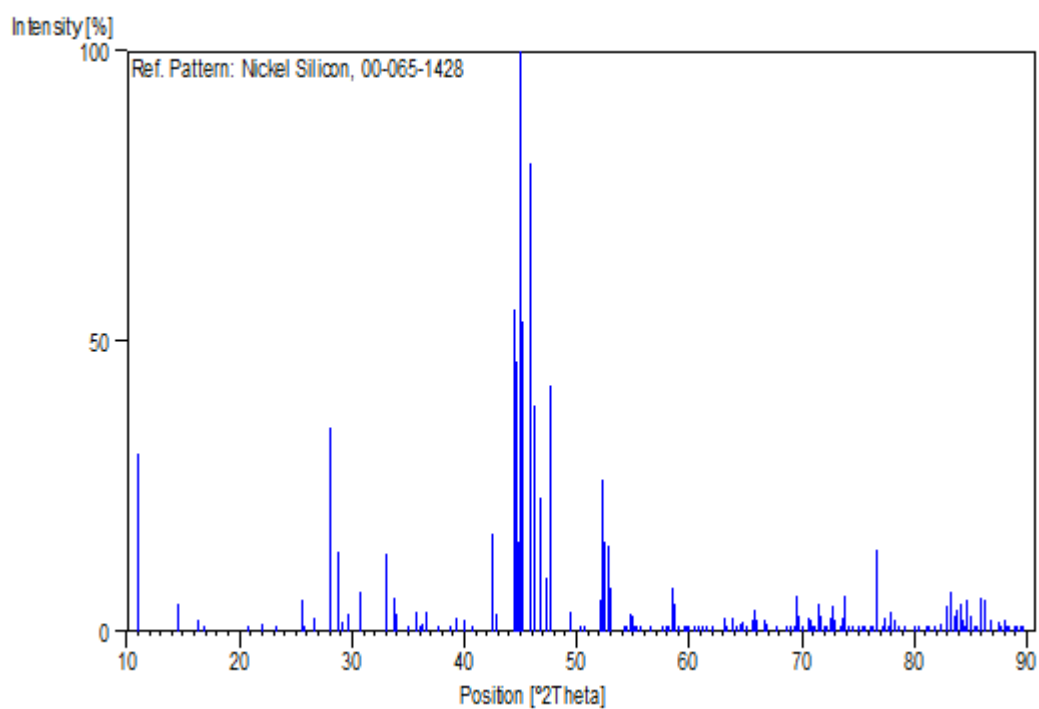
Peak list

No.	h	k	l	d [Å]	2Theta[deg]	I [%]
1	1	1	0	8.09717	10.918	30.7
2	2	0	0	6.11450	14.475	4.6
3	0	2	0	5.40250	16.395	2.1
4	1	1	1	5.26236	16.834	0.4
5	0	2	1	4.25935	20.838	0.1
6	2	2	0	4.04858	21.936	1.4
7	3	1	0	3.81394	23.304	0.3
8	2	2	1	3.49497	25.465	5.4
9	0	0	2	3.46200	25.712	0.1
10	3	1	1	3.34067	26.663	2.4
11	1	1	2	3.18325	28.007	35.2
12	1	3	1	3.09145	28.857	13.8
13	4	0	0	3.05725	29.187	1.6
14	2	0	2	3.01263	29.629	3.0
15	0	2	2	2.91487	30.647	6.9
16	0	4	0	2.69906	33.165	13.3
17	4	2	0	2.66076	33.656	5.7
18	2	2	2	2.63118	34.046	3.1
19	3	1	2	2.56342	34.975	1.1
20	0	4	1	2.51475	35.674	3.5
21	4	2	1	2.48368	36.136	0.3
22	2	4	0	2.47087	36.330	1.2
23	1	3	2	2.44550	36.720	3.4
24	5	1	0	2.38545	37.679	0.1
25	2	4	1	2.32714	38.660	0.3
26	4	0	2	2.29161	39.284	2.2
27	5	1	1	2.25535	39.942	1.9
28	1	1	3	2.21959	40.613	0.1
29	0	4	2	2.12968	42.409	16.7
30	0	2	3	2.12243	42.561	11.8
31	4	2	2	2.10966	42.831	3.1
32	6	0	0	2.03817	44.412	55.7
33	1	5	1	2.03413	44.505	46.6
34	4	4	0	2.02429	44.733	15.4
35	2	4	2	2.01118	45.040	100.0
36	2	2	3	2.00507	45.185	53.4
37	3	1	3	1.97460	45.922	80.7

38	5	1	2	1.96430	46.177	38.9
39	4	4	1	1.94214	46.735	23.1
40	1	3	3	1.91916	47.328	9.1
41	3	5	0	1.90930	47.588	42.4
42	3	5	1	1.84060	49.480	3.5
43	1	5	2	1.81292	50.288	0.3
44	0	6	0	1.80083	50.649	0.1
45	0	4	3	1.75472	52.079	5.3
46	4	4	2	1.74749	52.310	26.2
47	4	2	3	1.74285	52.460	15.3
48	0	0	4	1.73100	52.847	14.7
49	2	6	0	1.72460	53.058	7.4
50	1	1	4	1.69275	54.137	0.3
51	2	4	3	1.68664	54.350	0.2
52	7	1	1	1.67347	54.813	2.9
53	6	2	2	1.67033	54.925	2.7
54	2	0	4	1.66554	55.096	1.0
55	5	1	3	1.65871	55.342	0.3
56	0	2	4	1.64845	55.717	0.8
57	6	4	0	1.62699	56.517	0.7
58	0	6	2	1.59762	57.652	0.7
59	2	2	4	1.59162	57.890	0.8
60	6	4	1	1.58385	58.201	0.6
61	5	5	1	1.57688	58.484	7.6
62	7	3	0	1.57185	58.689	4.8
63	1	5	3	1.56450	58.992	0.2
64	4	6	0	1.55166	59.529	1.1
65	1	3	4	1.54762	59.700	1.0
66	7	1	2	1.54367	59.868	0.5
67	7	3	1	1.53142	60.397	0.7
68	8	0	0	1.52863	60.519	0.3
69	4	4	3	1.52187	60.816	0.9
70	4	6	1	1.51410	61.161	0.7
71	4	0	4	1.50631	61.512	0.3
72	1	7	1	1.49528	62.016	0.1
73	6	4	2	1.47249	63.085	2.2
74	6	2	3	1.47009	63.199	1.5
75	5	5	2	1.46688	63.354	0.7
76	0	4	4	1.45709	63.829	2.4
77	4	2	4	1.45097	64.131	0.3
78	3	7	0	1.44354	64.501	1.2
79	8	2	1	1.43877	64.740	1.5
80	7	3	2	1.43124	65.123	0.3
81	0	6	3	1.41978	65.715	2.0
82	2	4	4	1.41772	65.822	3.8
83	3	7	1	1.41316	66.062	1.9
84	5	1	4	1.40100	66.710	2.1
85	8	0	2	1.39838	66.851	1.2
86	2	6	3	1.38152	67.776	1.1
87	1	1	5	1.36498	68.712	0.1
88	7	5	0	1.35858	69.081	0.6
89	8	2	2	1.35376	69.362	0.8
90	0	8	0	1.35063	69.546	6.0
91	9	1	0	1.34816	69.692	2.8
92	1	5	4	1.34284	70.008	0.3
93	7	5	1	1.33236	70.641	2.3
94	8	4	0	1.32979	70.798	1.9
95	5	5	3	1.32566	71.052	0.5
96	9	1	1	1.32331	71.197	0.7
97	6	0	4	1.31938	71.441	4.8
98	4	4	4	1.31534	71.695	2.6
99	2	2	5	1.31027	72.015	0.7
100	8	4	1	1.30648	72.257	0.6
101	3	1	5	1.30165	72.568	2.3

102	7	3	3	1.29917	72.729	4.5
103	2	8	1	1.29554	72.965	2.1
104	4	6	3	1.28770	73.482	0.6
105	1	3	5	1.28539	73.636	2.5
106	3	5	4	1.28241	73.835	6.0
107	1	7	3	1.27606	74.264	0.1
108	9	3	0	1.27131	74.589	0.8
109	7	5	2	1.26468	75.047	0.2
110	0	8	2	1.25826	75.497	0.1
111	9	1	2	1.25627	75.637	0.5
112	9	3	1	1.25041	76.055	0.1
113	0	6	4	1.24796	76.231	0.1
114	8	4	2	1.24184	76.675	14.0
115	4	8	0	1.23544	77.145	0.8
116	2	8	2	1.23244	77.367	2.4
117	4	2	5	1.22839	77.670	1.0
118	3	7	3	1.22387	78.011	3.5
119	7	1	4	1.22141	78.198	2.0
120	4	8	1	1.21623	78.596	0.5
121	2	4	5	1.20801	79.235	0.1
122	5	1	5	1.19763	80.060	0.1
123	1	9	0	1.19481	80.287	0.4
124	9	3	2	1.19339	80.402	0.1
125	6	4	4	1.18552	81.047	0.2
126	5	5	4	1.18259	81.289	0.2
127	1	9	1	1.17741	81.723	0.1
128	10	2	1	1.17541	81.892	0.1
129	7	5	3	1.17080	82.284	1.3
130	9	1	3	1.16411	82.860	4.3
131	1	5	5	1.16068	83.160	6.7
132	7	7	0	1.15674	83.506	2.7
133	0	0	6	1.15400	83.749	3.7
134	9	5	0	1.15029	84.081	4.9
135	1	7	4	1.14698	84.380	1.9
136	8	0	4	1.14507	84.553	0.8
137	5	3	5	1.14278	84.762	5.5
138	7	7	1	1.14093	84.932	2.7
139	5	7	3	1.13621	85.368	1.1
140	9	5	1	1.13473	85.506	0.5
141	1	9	2	1.12944	86.003	5.9
142	6	8	0	1.12586	86.344	5.3
143	3	5	5	1.12099	86.812	1.9
144	10	4	0	1.11405	87.489	1.8
145	6	8	1	1.11127	87.763	0.9
146	3	7	4	1.10863	88.026	2.1
147	11	1	0	1.10589	88.301	1.1
148	3	1	6	1.10449	88.442	0.6
149	10	4	1	1.09991	88.907	0.1
150	0	6	5	1.09776	89.127	0.9
151	1	3	6	1.09456	89.458	0.7
152	3	9	2	1.09277	89.644	0.8

Stick Pattern



Name and formula

Reference code: 00-038-0844
PDF index name: Nickel Silicon
Empirical formula: NiSi
Chemical formula: NiSi

Crystallographic parameters

Crystal system: Orthorhombic
Space group: Pnma
Space group number: 62

a (Å): 5.2330
b (Å): 3.2580
c (Å): 5.6590
Alpha (°): 90.0000
Beta (°): 90.0000
Gamma (°): 90.0000

Volume of cell: 96.48
Z: 4.00

RIR: -

Subfiles and Quality

Subfiles: Inorganic
Alloy, metal or intermetallic
Common Phase
Quality: Calculated (C)

Comments

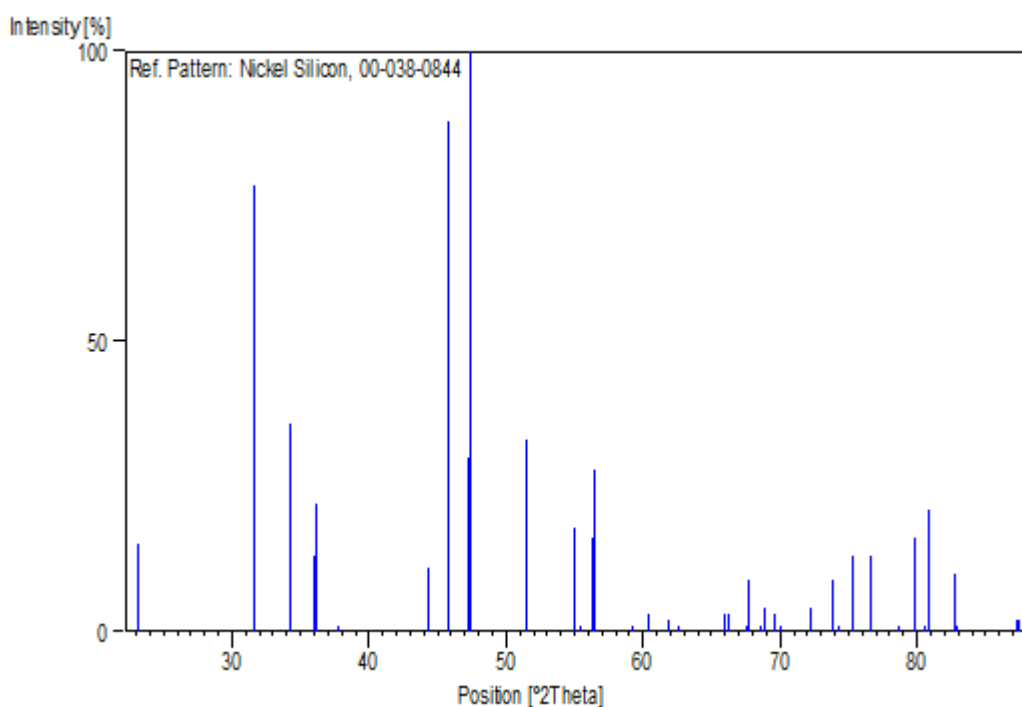
References

Primary reference: d'Heurle, F. et al., *J. Appl. Phys.*, **55**, 4218, (1984)
Unit cell: Toman, K., *Acta Crystallogr.*, **5**, 329, (1952)

Peak list

No.	h	k	l	d [Å]	2Theta[deg]	I [%]
1	1	0	1	3.84200	23.132	15.0
2	0	0	2	2.83000	31.589	15.0
3	0	1	1	2.82300	31.670	77.0
4	2	0	0	2.61600	34.250	36.0
5	1	0	2	2.48900	36.056	13.0
6	1	1	1	2.48500	36.116	22.0
7	2	0	1	2.37500	37.851	1.0
8	2	1	0	2.04000	44.370	11.0
9	1	1	2	1.97800	45.839	88.0
10	2	0	2	1.92100	47.280	30.0
11	2	1	1	1.91900	47.332	100.0
12	1	0	3	1.77500	51.440	33.0
13	3	0	1	1.66700	55.044	18.0
14	2	1	2	1.65500	55.477	1.0
15	0	1	3	1.63200	56.328	16.0
16	0	2	0	1.62900	56.441	28.0
17	1	1	3	1.55800	59.262	1.0
18	2	0	3	1.53000	60.459	3.0
19	1	2	1	1.50000	61.799	2.0
20	3	0	2	1.48400	62.540	1.0
21	0	0	4	1.41500	65.965	3.0
22	0	2	2	1.41100	66.176	3.0
23	2	1	3	1.38500	67.583	1.0
24	2	2	0	1.38300	67.694	9.0
25	1	0	4	1.36600	68.653	1.0
26	1	2	2	1.36300	68.825	4.0
27	3	1	2	1.35100	69.524	3.0
28	2	2	1	1.34300	69.999	1.0
29	4	0	0	1.30800	72.160	4.0
30	3	0	3	1.28100	73.930	9.0
31	4	0	1	1.27500	74.336	1.0
32	1	1	4	1.26000	75.374	13.0
33	2	2	2	1.24200	76.663	13.0
34	4	1	0	1.21400	78.768	1.0
35	1	2	3	1.20000	79.870	16.0
36	3	1	3	1.19200	80.515	1.0
37	4	0	2	1.18700	80.925	21.0
38	3	2	1	1.16500	82.783	10.0
39	2	1	4	1.16300	82.957	1.0
40	4	1	2	1.11600	87.297	2.0
41	2	2	3	1.11500	87.395	2.0

Stick Pattern



Name and formula

Reference code: 01-073-2092
ICSD name: Nickel Silicon
Empirical formula: Ni₂Si
Chemical formula: Ni₂Si

Crystallographic parameters

Crystal system: Orthorhombic
Space group: Pbnm
Space group number: 62

a (Å): 7.0600
b (Å): 4.9900
c (Å): 3.7200
Alpha (°): 90.0000
Beta (°): 90.0000
Gamma (°): 90.0000

Calculated density: 7.37
Measured density: 7.23
Volume of cell: 131.05
Z: 4.00

RIR: 1.52

Subfiles and Quality

Subfiles: Inorganic
Alloy, metal or intermetallic
Corrosion
Modelled additional pattern
Quality: Calculated (C)

Comments

Additional pattern: See PDF 50-779.
ICSD collection code: 024641
Test from ICSD: Calc. density unusual but tolerable.

References

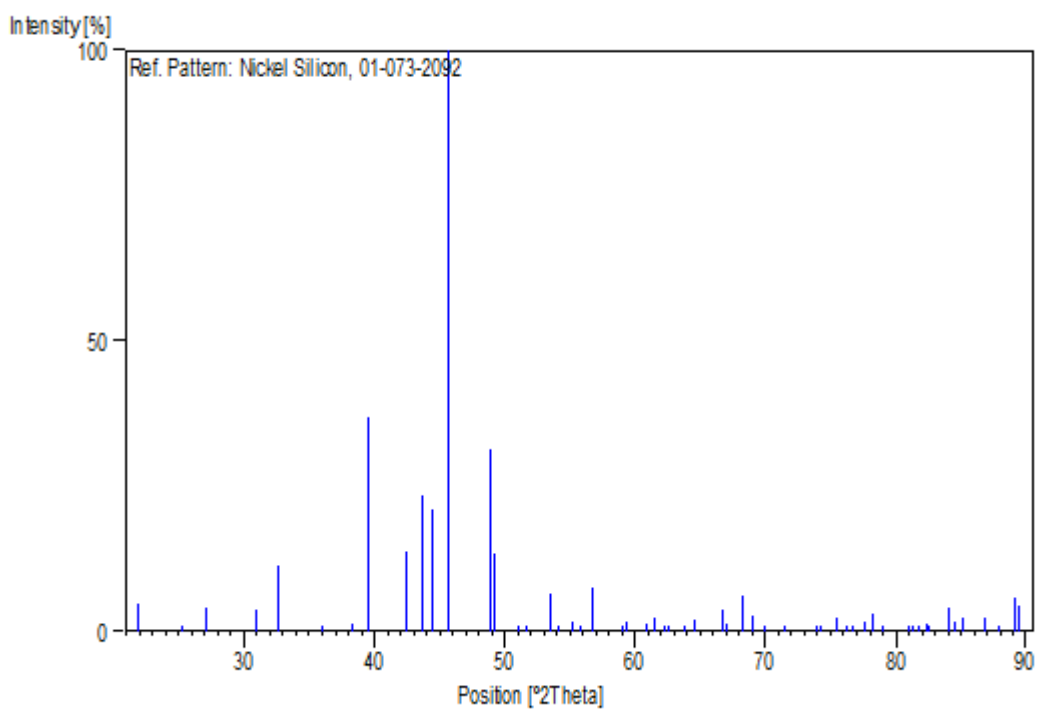
Primary reference: *Calculated from ICSD using POWD-12++*, (1997)
Structure: Toman, K., *Acta Crystallogr.*, **5**, 329, (1952)

Peak list

No.	h	k	l	d [Å]	2Theta [deg]	I [%]
1	1	1	0	4.07491	21.793	4.7
2	2	0	0	3.53000	25.208	0.2
3	1	0	1	3.29109	27.072	4.1
4	2	1	0	2.88181	31.007	3.8
5	1	1	1	2.74736	32.566	11.4
6	0	2	0	2.49500	35.966	0.9
7	1	2	0	2.35242	38.228	1.4
8	2	1	1	2.27818	39.525	36.9
9	3	1	0	2.12850	42.434	13.8
10	0	2	1	2.07210	43.647	23.3
11	2	2	0	2.03745	44.428	21.1
12	3	0	1	1.98879	45.576	100.0
13	0	0	2	1.86000	48.930	31.2
14	3	1	1	1.84746	49.284	13.3
15	2	2	1	1.78698	51.070	0.3
16	4	0	0	1.76500	51.753	0.1
17	3	2	0	1.71195	53.482	6.5
18	1	1	2	1.69206	54.161	0.4
19	4	1	0	1.66398	55.152	1.5
20	2	0	2	1.64554	55.824	0.1
21	1	3	0	1.61901	56.821	7.5
22	2	1	2	1.56276	59.064	0.5
23	3	2	1	1.55517	59.381	1.7
24	4	1	1	1.51894	60.946	1.3
25	2	3	0	1.50466	61.587	2.3
26	0	2	2	1.49122	62.203	0.3
27	1	3	1	1.48451	62.516	0.1
28	1	2	2	1.45903	63.735	0.3
29	4	2	0	1.44091	64.633	2.0
30	3	1	2	1.40059	66.732	3.6
31	2	3	1	1.39488	67.041	1.2
32	2	2	2	1.37368	68.216	6.0
33	5	1	0	1.35865	69.077	2.8
34	4	2	1	1.34363	69.961	0.3
35	5	0	1	1.32010	71.397	0.5
36	4	0	2	1.28031	73.976	0.1
37	5	1	1	1.27591	74.274	0.1
38	3	2	2	1.25962	75.401	2.4
39	0	4	0	1.24750	76.264	0.3
40	4	1	2	1.24014	76.799	0.5
41	5	2	0	1.22847	77.664	1.7

42	1	0	3	1.22119	78.215	3.1
43	4	3	0	1.21050	79.040	0.4
44	1	1	3	1.18629	80.983	0.2
45	0	4	1	1.18277	81.275	0.1
46	6	0	0	1.17621	81.824	0.4
47	2	3	2	1.16981	82.369	1.2
48	5	2	1	1.16684	82.624	0.9
49	4	3	1	1.15109	84.009	4.0
50	6	1	0	1.14526	84.536	1.5
51	4	2	2	1.13909	85.101	2.2
52	2	4	1	1.12149	86.763	2.2
53	0	2	3	1.11042	87.848	0.8
54	3	0	3	1.09703	89.202	5.9
55	6	1	1	1.09456	89.458	4.3

Stick Pattern



Name and formula

Reference code: 00-024-0524
 PDF index name: Nickel Silicon
 Empirical formula: $\text{Ni}_{31}\text{Si}_{12}$
 Chemical formula: $\text{Ni}_{31}\text{Si}_{12}$

Crystallographic parameters

Crystal system: Hexagonal
 Space group: P321
 Space group number: 150

a (Å): 6.6700
b (Å): 6.6700
c (Å): 12.2800
Alpha (°): 90.0000
Beta (°): 90.0000
Gamma (°): 120.0000

Calculated density: 7.57
Volume of cell: 473.13
Z: 1.00

RIR: -

Status, subfiles and quality

Status: Marked as deleted by ICDD
Subfiles: Inorganic
Alloy, metal or intermetallic
Quality: Calculated (C)

Comments

Deleted by: cell incomplete; WFM 1/01.
Additional pattern: See 17-222.
See ICSD 9106 (PDF 71-638).

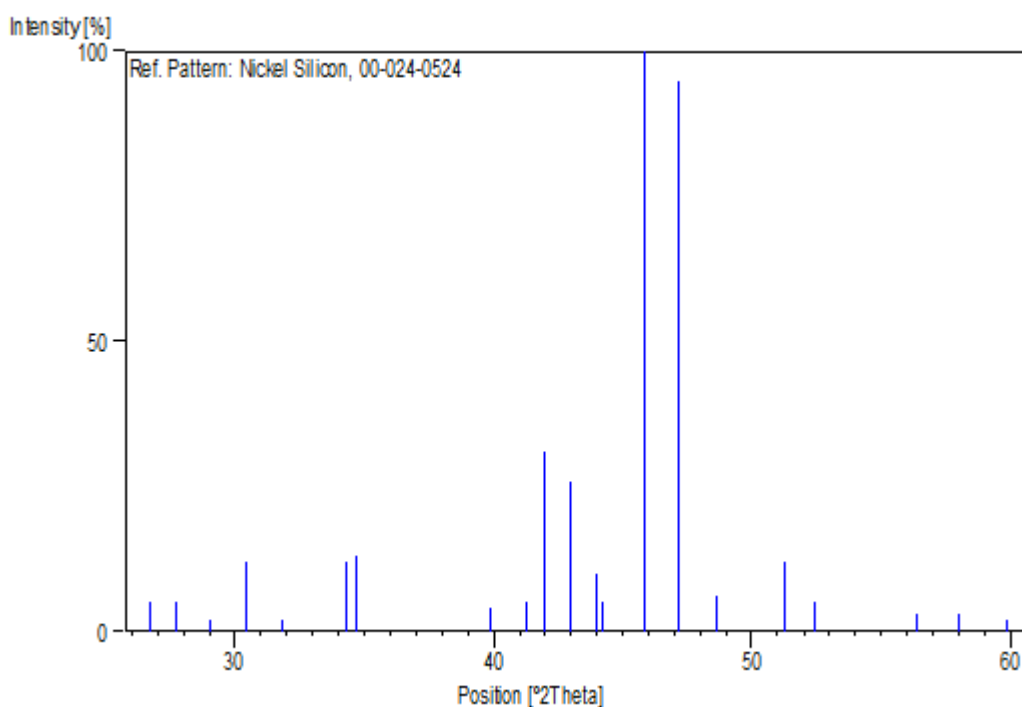
References

Primary reference: Smith et al., Penn State University, University Park,
Pennsylvania, USA., *ICDD Grant-in-Aid*, (1973)
Unit cell: Frank, Schubert., *Acta Crystallogr., Sec. B*, **27**, 916, (1971)

Peak list

No.	h	k	l	d [Å]	2Theta [deg]	I [%]
1	1	1	0	3.33500	26.709	5.0
2	1	1	1	3.21800	27.699	5.0
3	0	0	4	3.07000	29.063	2.0
4	1	1	2	2.93100	30.474	12.0
5	2	0	1	2.81100	31.809	2.0
6	2	0	2	2.61300	34.291	12.0
7	1	1	3	2.58600	34.660	13.0
8	1	1	4	2.25900	39.875	4.0
9	2	1	0	2.18300	41.325	5.0
10	2	1	1	2.15000	41.989	31.0
11	2	0	4	2.10400	42.952	26.0
12	2	1	2	2.05700	43.984	10.0
13	0	0	6	2.04700	44.210	5.0
14	1	1	5	1.97760	45.848	100.0
15	3	0	0	1.92550	47.163	95.0
16	2	0	5	1.87100	48.624	6.0
17	2	1	4	1.77920	51.310	12.0
18	1	1	6	1.74440	52.410	5.0
19	2	1	5	1.63170	56.339	3.0
20	3	1	1	1.58860	58.011	3.0
21	2	2	3	1.54430	59.842	2.0

Stick Pattern



Name and formula

Reference code: 00-003-1094
PDF index name: Nickel Silicon
Empirical formula: NiSi₂
Chemical formula: NiSi₂

Crystallographic parameters

Crystal system: Rhombohedral
Space group: R
a (Å): 12.6020
b (Å): 12.6020
c (Å): 15.2770
Alpha (°): 90.0000
Beta (°): 90.0000
Gamma (°): 120.0000
Volume of cell: 2101.10
Z: 18.00
RIR: -

Status, subfiles and quality

Status: Marked as deleted by ICDD
Subfiles: Inorganic
Quality: Blank (B)

Comments

Deleted by: Deleted by M&A review.
Analysis: Analysis (wt.%): Si 49.0.
Unit cell: Rhombohedral cell: a=8.881, a=90.39.

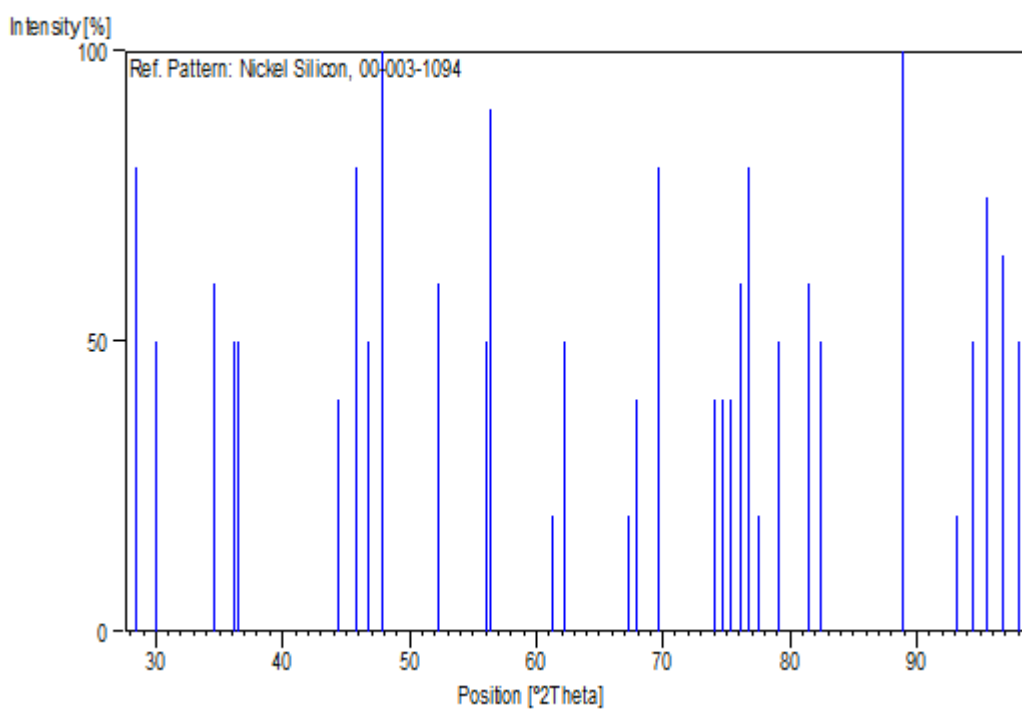
References

Primary reference: Osawa, Okamoto., *Sci. Rep. Tohoku Imp. Univ., Ser. 1*, **27**, 341, (1939)

Peak list

No.	h	k	l	d [Å]	2Theta[deg]	I [%]
1	0	2	4	3.13000	28.494	80.0
2	1	3	1	2.97000	30.064	50.0
3	0	4	2	2.59000	34.605	60.0
4	3	2	1	2.48000	36.191	50.0
5	1	2	5	2.46000	36.496	50.0
6	2	4	1	2.04000	44.370	40.0
7	2	2	6	1.98000	45.790	80.0
8	3	3	3	1.94000	46.789	50.0
9	1	5	2	1.90000	47.835	100.0
10	5	2	0	1.75000	52.230	60.0
11	1	1	9	1.64000	56.029	50.0
12	6	1	2	1.63000	56.403	90.0
13	1	0	10	1.51000	61.345	20.0
14	2	2	9	1.49000	62.260	50.0
15	7	1	3	1.39000	67.307	20.0
16	4	1	9	1.38000	67.861	40.0
17	2	0	11	1.35000	69.583	80.0
18	0	8	4	1.28000	73.997	40.0
19	4	5	5	1.27000	74.679	40.0
20	1	8	2	1.26000	75.374	40.0
21	0	5	10	1.25000	76.084	60.0
22	6	0	9	1.24000	76.809	80.0
23	2	4	10	1.23000	77.549	20.0
24	6	3	6	1.21000	79.079	50.0
25	9	0	3	1.18000	81.506	60.0
26	7	3	4	1.17000	82.352	50.0
27	7	1	9	1.10000	88.898	100.0
28	1	8	8	1.06000	93.221	20.0
29	6	6	0	1.05000	94.381	50.0
30	8	3	5	1.04000	95.578	75.0
31	5	2	12	1.03000	96.811	65.0
32	2	4	13	1.02000	98.085	50.0

Stick Pattern



Name and formula

Reference code: 00-065-0360
ICSD name: Silicon Carbide
Empirical formula: CSi
Chemical formula: SiC

Crystallographic parameters

Crystal system: Cubic
Space group: F-43m
Space group number: 216

a (Å): 4.3581
b (Å): 4.3581
c (Å): 4.3581
Alpha (°): 90.0000
Beta (°): 90.0000
Gamma (°): 90.0000

Volume of cell: 82.77
Z: 4.00

RIR: 3.53

Subfiles and Quality

Subfiles: Inorganic
Alloy, metal or intermetallic
Modelled additional pattern

Quality: Calculated (C)

Comments

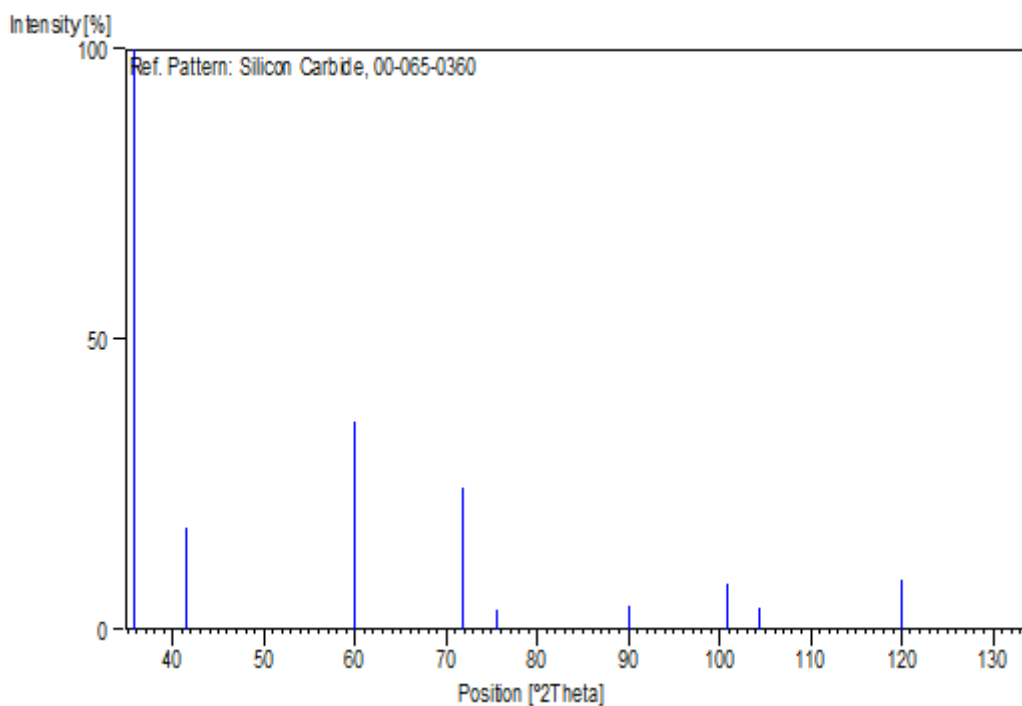
References

Primary reference: *Calculated from NIST using POWD-12++*
Structure: Z.Li & R.C.Bradt, *J. Mater. Sci.*, **21**, 4366-, (1986)

Peak list

No.	h	k	l	d [Å]	2Theta [deg]	I [%]
1	1	1	1	2.51615	35.654	100.0
2	2	0	0	2.17905	41.403	17.7
3	2	2	0	1.54082	59.991	35.7
4	3	1	1	1.31402	71.778	24.6
5	2	2	2	1.25808	75.509	3.3
6	4	0	0	1.08953	89.983	4.1
7	3	3	1	0.99982	100.787	8.0
8	4	2	0	0.97450	104.456	3.7
9	4	2	2	0.88959	119.971	8.5
10	5	1	1	0.83872	133.394	6.6

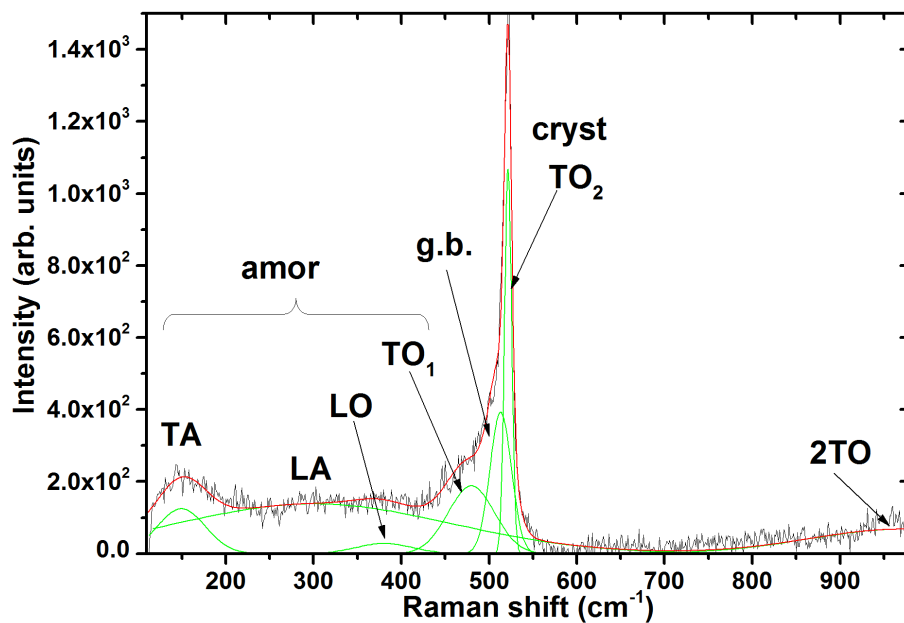
Stick Pattern



Appendices B: Gaussian plot of Raman scattering.

Peak Analysis

Data Set:[Book3]Sheet1!B Date:12/12/2014
 Baseline:Spline
 Chi²=6.91017E+002 Adj. R-Square=9.71459E-001 # of Data Points=852.
 SS=5.79072E+005 Degree of Freedom=838.



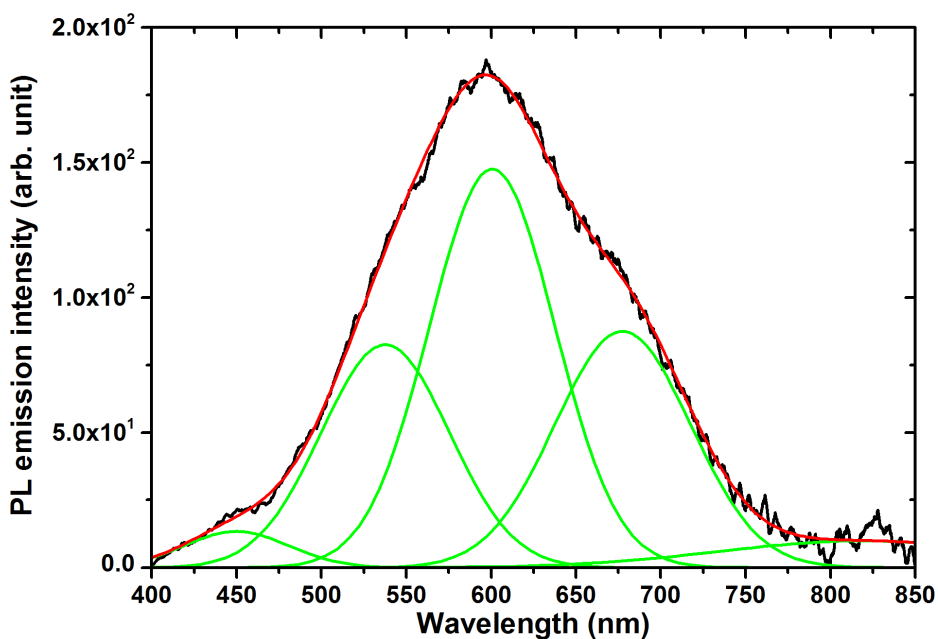
Fitting Results

Peak Index	Peak Type	Area Intg	FWHM	Max Height	Center Grvty	Area IntgP
1.	Gaussian	7919.41756	65.00529	124.74415	149.45652	7.20655
2.	Gaussian	48177.7813	369.28651	138.32495	300.20704	43.84106
3.	Gaussian	2281.98955	75.78547	28.28756	380.43478	2.07658
4.	Gaussian	12511.48824	62.59822	187.76505	479.64113	11.38527
5.	Gaussian	11982.09971	28.70298	392.16946	513.07797	10.90353
6.	Gaussian	10885.61827	9.5813	1067.32449	521.48033	9.90575
7.	Gaussian	16133.53287	250	68.00198	970.06556	14.68127

Appendices C: Gaussian plot of PL spectrum.

Peak Analysis

Data Set:[Book3]Sheet1!Smoothed Y1 Date:1/1/2015
 Baseline:Spline
 Chi²=8.34702E+000 Adj. R-Square=9.97737E-001 # of Data Points=6987.
 SS=5.82455E+004 Degree of Freedom=6978.



Fitting Results

Peak Index	Peak Type	Area Intg	FWHM	Max Height	Center Grvty	Area IntgP
1.	Gaussian	1751.78677	200	9.89952	818.59903	5.31325
2.	Gaussian	8754.96371	94.09159	87.41206	677.53623	26.5542
3.	Gaussian	13673.25871	87.07246	147.52276	600.60386	41.47161
4.	Gaussian	7805.91094	88.93444	82.46693	537.56039	23.67568
5.	Gaussian	984.24404	73.09116	13.37017	449.87923	2.98526